



**TEMPERATURE DEPENDENT CURRENT-VOLTAGE MEASUREMENTS OF
NEUTRON IRRADIATED $\text{Al}_{0.27}\text{Ga}_{0.73}\text{N}/\text{GaN}$ MODULATION DOPED FIELD
EFFECT TRANSISTORS**

THESIS

Troy A. Uhlman, Captain, USAF

AFIT/GNE/ENP/05-16

**DEPARTMENT OF THE AIR FORCE
AIR UNIVERSITY
AIR FORCE INSTITUTE OF TECHNOLOGY**

Wright-Patterson Air Force Base, Ohio

APPROVED FOR PUBLIC RELEASE; DISTRIBUTION UNLIMITED

The views expressed in this thesis are those of the author and do not reflect the official policy or position of the United States Air Force, Department of Defense, or the United States Government.

TEMPERATURE DEPENDENT CURRENT-VOLTAGE MEASUREMENTS OF
NEUTRON IRRADIATED $\text{Al}_{0.27}\text{Ga}_{0.73}\text{N}/\text{GaN}$ MODULATION DOPED FIELD
EFFECT TRANSISTORS

THESIS

Presented to the Faculty

Department of Engineering Physics

Graduate School of Engineering and Management

Air Force Institute of Technology

Air University

Air Education and Training Command

In Partial Fulfillment of the Requirements for the
Degree of Master of Science in Nuclear Engineering

Troy A. Uhlman, BSEP

Captain, USAF

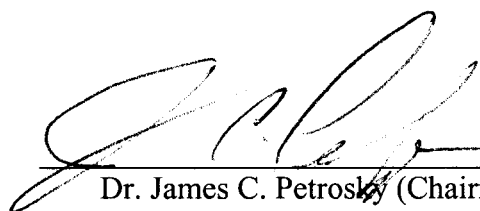
March 2005

APPROVED FOR PUBLIC RELEASE; DISTRIBUTION UNLIMITED

TEMPERATURE DEPENDENT CURRENT-VOLTAGE MEASUREMENTS OF
NEUTRON IRRADIATED $\text{Al}_{0.27}\text{Ga}_{0.73}\text{N}/\text{GaN}$ MODULATION DOPED FIELD
EFFECT TRANSISTORS

Troy A. Uhlman, BSEP
Captain, USAF

Approved:



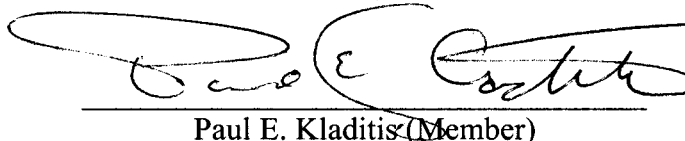
Dr. James C. Petrosky (Chairman)

11 Mar 05
date



Dr. Robert L. Hengehold (Member)

11 Mar 05
date



Paul E. Kladitis (Member)

11 Mar 05
date

Abstract

In the first ever neutron irradiation study of AlGaN/GaN MODFETs, devices were irradiated to a total fluence of 1.2×10^{16} n-cm⁻² 1 MeV equivalent (Si) neutrons. Devices irradiated at 80 K exhibit significant persistent electrical degradation at 5.4 rad (Si), whereas those irradiated at elevated temperatures exhibit transient increases in gate and drain current up to 392 krad (Si).

I-V measurements indicate that substantial radiation-induced increased gate and drain currents occur only at low-temperature irradiations. The introduction of a high density of donor defects is hypothesized as the primary cause of both increased values. The defects are persistent at temperatures < 300 K. However, subsequent irradiations at temperatures > 300 K accelerate annealing. The primary mechanism of accelerated annealing is thought to be a combination of device self-heating and high temperature ambient during irradiation. Irradiating at temperatures > 300 K effectively nullifies accumulated dose at 1.2×10^{16} n-cm⁻².

Analysis of the Schottky contacts has determined that the devices are tunneling dominated at all temperatures. A high density of surface states introduced at the metal-semiconductor junction following irradiation facilitates defect-assisted tunneling across the barrier. Current-voltage characteristics in a wide temperature range are used to determine the Schottky barrier height and associated diode parameters utilizing a unique six-parameter fitting routine.

To my wife and family

Acknowledgments

I would like to express my sincere appreciation to my faculty advisor, Dr. James C. Petrosky, for his guidance and support throughout the course of this thesis effort. His breadth of experience as an experimentalist and as a senior military officer is both unique and inspiring. I truly value his opinion and appreciate his kind conversation and candor. Furthermore, I sincerely thank my committee members, Dr. Robert L. Hengehold and Captain Paul E. Kladitis for their straight-shooting approach in guiding me through this learning process.

Additionally, Major Laura Suzuki of the AFIT Department of Mathematics and Statistics was critical to the success of my research. Her unrelenting enthusiasm and eagerness to assist in creating a usable mathematical fitting model was invaluable. Without her assistance, this research endeavor would not have succeeded.

I would also like to thank Jan LeValley, Condie Inman, and Robert Jarusiewic of the AFIT model workshop, Joseph Talnagi, Andrew Kauffman, and Sean Zalesny of The Ohio State University Research Reactor, and especially Renate Hannaford of the AFIT Academic Library for their efforts in assisting with various phases of the research process.

To my wife, there simply is not enough gratitude to fully thank you. Thank you so much for supporting me through these crazy times. You kept me well fed, well encouraged, and most of all well loved. This was a team effort.

Troy A. Uhlman

Table of Contents

	Page
Abstract.....	iv
Acknowledgments.....	vi
List of Figures.....	ix
List of Tables	xvi
I. Introduction	1
III-V Nitride Revolution	1
Problem Statement	4
Hypothesis.....	4
Objectives	4
Scope.....	5
Approach.....	5
Assumptions/Limitations	8
Sequence of Presentation	9
II. Current State of Technology	10
Purpose.....	10
The Need for Group-III Heterostructures	10
Radiation Effects on $\text{Al}_{0.27}\text{Ga}_{0.73}\text{N}/\text{GaN}$ Heterostructures.....	17
Research Justification	38
III. Theory	39
MODFET Charge-Control Model.....	39
Rectifying Contacts and Charged Carrier Transport	52
IV. Experimental Procedures	65
Device Fabrication and Packaging.....	65
Neutron-Specific Experimental Considerations	68
Pre-irradiation Characterization.....	69
Long Term Anneal Study.....	75
Irradiation Experiments	75
Dosimetry.....	85

V. Experimental Results	89
In situ Irradiation Experiment: A25	89
Rabbit Tube Irradiation Experiment: A25	97
Rabbit Tube Irradiation Experiment: A27	103
Rabbit Tube Irradiation Experiment: A29	108
Rabbit Tube Irradiation Experiment: A30	114
Analysis and Discussion	123
VI. Conclusions and Recommendations	130
Conclusions	130
Recommended Further Work	132
Appendix A – Nitride Parameters	135
Appendix B – Schottky Diode Parameter Extraction Methods	136
Thermionic Emission Theory	136
Six-parameter Fitting Model	144
Appendix C – Nine Month Anneal Study	153
Bibliography	164

List of Figures

Figure	Page
1. Intrinsic Carrier Concentration of commonly used semiconductor materials [10].	11
2. Empirical relationship between E_d and reciprocal lattice constant [11].	12
3. Potential Applications of GaN-based devices [18].	16
4. Transfer characteristics for a $1.2 \times 200 \mu\text{m}^2$ MODFET pre and post 600 Mrad total dose gamma irradiation [20].	20
5. I_{ds} - V_{ds} characteristics for a $1.2 \times 200 \mu\text{m}^2$ MODFET pre and post 600 Mrad total dose gamma irradiation [20].	21
6. I_D - V_{DS} characteristics of a $0.25 \times 150 \mu\text{m}^2$ AlGaN/GaN MODFET at various gamma irradiation doses [19].	23
7. Transfer characteristics of a $0.25 \times 150 \mu\text{m}^2$ AlGaN/GaN MODFET at various radiation doses. The anomalous spike is an artifact of taking the derivative of the saturation drain current as a function of the gate voltage [19].	23
8. Transfer characteristics for AlGaN/GaN MODFETs before and after 10-keV X-ray irradiation at fluences up to 30 Mrad (SiO_2) [23].	25
9. Common-Source I-V Curves - Pre-Irradiation (Solid Curves), Post $10^{11} \text{ p}^+ \cdot \text{cm}^{-2}$ (Dashed Curves), and Post- $10^{12} \text{ p}^+ \cdot \text{cm}^{-2}$ (Dotted Curves) [35].	32
10. Transfer characteristics and g_m . Pre-Irradiation (Solid Curves), Post $10^{12} \text{ p}^+ \cdot \text{cm}^{-2}$ (Dashed Curves), and post $5 \times 10^{12} \text{ p}^+ \cdot \text{cm}^{-2}$ (Dotted Curves) [35].	33
11. Drain saturation current as a function of proton fluence [36].	34
12. Extracted threshold voltage and peak transconductance as a function of proton fluence [36].	34
13. Normalized mobility and 2DEG sheet density, extracted from RT Hall effect measurements. The initial 2DEG mobility and sheet density were $987 \text{ cm}^2 \cdot \text{V}^{-1} \cdot \text{s}^{-1}$ and $1.03 \times 10^{13} \text{ cm}^{-2}$ [36].	35

14. Transfer characteristics for AlGaN/GaN MODFETs before and after 1.8-MeV proton irradiation at different fluences [23].	36
15. $I_{ds} - V_{ds}$ characteristics for AlGaN/GaN MODFETS before and after 1.8-MeV proton irradiation at different fluences at RT [23].	37
16. Basic MODFET structure with the x-axis in/out of the page and z-axis top to bottom (not to scale).	40
17. Qualitative description of an AlGaN/GaN interface [37].	41
18. Crystalline structure of wurtzite Ga-face and N-face GaN [39].	42
19. Polarization induced sheet charge density[39].	43
20. Schematic representation of AlGaN/GaN MODFET design used in derivation of the presented charge-control model [44].	47
21. The energy band profile of the modeled AlGaN/GaN MODFET [44].	47
22. Schematic diagram illustrating the parasitic resistance [12].	49
23. Metal-semiconductor contacts [47].	53
24. Conduction mechanisms for m-s contacts.	57
25. Band diagram of a Schottky barrier contact under forward bias [48].	57
26. Effects of resistance on Schottky diode parameter extraction.	62
27. Proposed dc equivalent circuit of a Schottky structure [52].	63
28. AlGaN/GaN/4H-SiC Wafer segment.	66
29. Reticle containing MODFET and test structures [29].	66
30. Packaged reticle [29].	66
31. Wired FATFET with appropriate contacts shown.	67
32. Absorption cross section of Cadmium.	69
33. Experimental setup showing electronic measurement equipment.	70
34. Measurement-type control switch.	70
35. Schematic representation of experimental equipment setup.	71

36.	Dewar shown in wooden cradle designed to fit within the 7" section of the beam port. Inset shows Cadmium shielded thermal block.	74
37.	Wooden cradle used for both <i>in situ</i> beam port measurements and benchtop characterizations at 80 K in darkness.....	74
38.	6" Dewar system for <i>in situ</i> measurements at 80 K within the BP.....	75
39.	OSURR core and relative placement of irradiation facilities.	76
40.	Insertion of Dewar apparatus into beam port for <i>in situ</i> measurements (LEFT) and polyurethane plug to moderate streaming neutrons (RIGHT).	78
41.	Shielding of the beam port with lead bricks (LEFT) and concrete blocks (RIGHT) to attenuate neutron-induced gamma radiation.....	78
42.	Pneumatically actuated rabbit tube with automatic timer shown.	80
43.	Rabbit Tube sample carrier.....	81
44.	OSURR Neutron Spectrum at 500 kW.....	86
45.	Displacement damage KERMA functions for Si and GaAs.....	88
46.	A25: Drain current versus gate voltage and extrinsic transconductance as a function of neutron fluence measured at $V_d = +6.0$ V. The RSD <1.4 %.	90
47.	A25: Extracted threshold voltage as a function of neutron fluence.....	90
48.	A25: I-V characteristics as a continuum of accumulated dose. The RSD <1.3%.	91
49.	A25: I-V characteristics shown as a function of neutron fluence. The maximum increase in drain current at $V_d = +6.0$ V is 14%, 20%, and 33% for $V_g = 0.0$, -1.0, and -2.0 respectively. The maximum RSD <0.46%.....	91
50.	A25: Gate leakage as a continuum of accumulated dose. The arrow denotes a continuous increase of gate current with dose to a maximum increase in magnitude of 16% for $V_g = -2.0$	92
51.	A25: Gate leakage shown as a function of neutron fluence. Measurement run zero represents the pre-irradiation measurement.....	93
52.	A25: SBH alteration during <i>in situ</i> measurements at 80 K. Data points removed that had excessive error in the fitting parameter phi.....	94
53.	A25: GR saturation current as a function of increasing neutron fluence.....	95

54. A25: Tunneling saturation current as a function of increasing neutron fluence.....	96
55. A25: The reciprocal of the tunneling parameter, E_0 as a function of increasing neutron fluence.....	96
56. A25: Actual unaided nitrogen burn off shown along with optimal temperature profile.....	97
57. A25: TE saturation current in a wide temperature range.....	98
58. A25: Arrhenius plot of GR saturation current.....	99
59. A25: Arrhenius plot of tunneling saturation current with three distinct linear regions shown.....	99
60. A25: Temperature dependence of series resistance.....	100
61. A25: Transfer characteristics at 80 K upon RT irradiation.....	101
62. A25: Threshold voltage shift as a function of neutron fluence.....	101
63. A25: Drain current as a function of neutron fluence at a fixed drain voltage of +6.0 V. The maximum RSD <0.7%.....	102
64. A25: Gate current as a function of neutron fluence at a fixed drain voltage of +6.0 V. The maximum RSD <10%.....	103
65. A27: Transfer and extrinsic g_m . The maximum RSD <0.5 %.....	104
66. A27: Threshold voltage shift as a function of neutron fluence.....	105
67. A27: Pre- and post-irradiation characteristics. Closed symbols designate pre-irradiation measurements, and open symbols designate post-irradiation to the specific fluence. Maximum RSD <2%.....	106
68. A27: Drain current as a function of neutron fluence at a fixed drain voltage of +6.0 V. The maximum RSD <1%.....	106
69. A27: Pre- and post-irradiation gate leakage. Symbols have the same meaning as above.....	107
70. A27: Gate leakage as a function of neutron fluence.....	107
71. A29: Threshold voltage shift as a function of neutron fluence. The maximum positive shift in V_{th} is 2.5 %.....	109

72. A29: Pre-irradiation I-V characteristics. The maximum RSD <2%.....	109
73. A29: Drain current as a function of neutron fluence at a fixed drain voltage of +6.0 V. The maximum RSD <1.1%.....	110
74. A29: Pre-irradiation gate leakage characteristics.....	111
75. A29: Gate leakage as a function of fluence measured at $V_d = +6.0$ V. The maximum decrease in gate leakage is approximately 45% at 5×10^{15} n-cm $^{-2}$ for all gate voltages. The decrease in leakage at maximum fluence is 20, 25, and 30% for $V_g = 0.0, -1.0$, and -2.0 V, respectively.....	111
76. A29: Plot of TE saturation current and SBH as a function of neutron fluence and time of RT anneal. Arbitrary areal Richardson constant of 5×10^{-8} A-K $^{-2}$ used to determine the SBH.....	113
77. A30: Pre-irradiation Schottky diode parameter extraction of the areal Richardson constant and temperature-independent SBH.....	114
78. A30: Determination of the tunneling parameter E_{00} from E_0	115
79. A30: Comparison of TE saturation current following a total fluence of 1.2×10^{16} n-cm $^{-2}$	116
80. A30: Comparison of GE saturation current following a total fluence of 1.2×10^{16} n-cm $^{-2}$	116
81. A30: Comparison of tunneling saturation current following a total fluence of 1.2×10^{16} n-cm $^{-2}$	117
82. A30: Comparison of tunneling saturation current following a total fluence of 1.2×10^{16} n-cm $^{-2}$	117
83. A30: The reciprocal tunneling parameter E_0 , before and following a total fluence of 1.2×10^{16} n-cm $^{-2}$	118
84. A30: GLADC I-V characteristics at 80 K (symbols) and 295 K (solid line). The maximum RSD <1% at 80 K and <2% at RT.....	119
85. A30: Pre-irradiation characterization at 295 K.....	119
86. A30: Pre-irradiation characterization at 80 K.....	120
87. A30: Gate leakage adjusted drain current pre-irradiation (solid symbols) and post-irradiation (open symbols). The maximum RSD for all measurements <1.4%.....	121

88. A30: GLADC as a function of fluence measured at $V_d = +6.0$ V. The increase in drain current at the maximum dose is approximately 14, 9, and 6.5% for gate voltages of -2, -1, and 0 V, respectively. The maximum RSD for all measurements is <0.8%.....	121
89. A30: Gate leakage current pre-irradiation (solid symbols) and post-irradiation (open symbols). The maximum increase is nominally 14% for $V_g = -2.0$ V and decreases for increasing gate voltage.	122
90. A30: Gate leakage as a function of fluence measured at $V_d = +6.0$ V. The increase in gate leakage at the maximum dose is approximately 18.5, 13.75, and 0% for gate voltages of -2.0, -1.0, and 0.0 V, respectively.....	122
91. A30: Transfer characteristics and transconductance measured at RT. The maximum RSD <1.5%.....	123
92. Sample Schottky diode curve at 80K.....	138
93. Semi-log current plot for Schottky diode parameter extraction.....	138
94. Temperature dependent ideality factor.	139
95. Temperature dependent TE saturation current.....	140
96. Temperature dependency of ideality factor.	141
97. Richardson and modified Richardson Plot.	142
98. Temperature dependence of the ideality factor and SBH.	143
99. Zero-bias apparent SBH vs. ideality factor.....	143
100. Six-parameter fitting model extracted via numerical fitting routine.	144
101. TE saturation current in a wide temperature range.....	147
102. Temperature dependence of barrier height determined by the six-parameter method and TE only approach.	147
103. Arrhenius plot of TE saturation current.	148
104. Arrhenius plot of GR saturation current.	148
105. Temperature dependence of tunneling saturation current in a wide temperature range.....	149

106. Arrhenius plot of tunneling saturation current with three distinct linear regions shown	149
107. Reciprocal tunneling parameter, E_0	150
108. Temperature dependence of series resistance.....	150
109. Temperature dependence of parasitic resistance, R_1	151
110. A0408: Solid symbols are pre-irradiation, open symbols are $3 \times 10^{14} \text{ e}^- \cdot \text{cm}^{-2}$, open-lined symbols are 9-mos measurements. Data is gate leakage adjusted drain current. The maximum RSD <1%.....	154
111. A0408: Non-Gate leakage adjusted drain current characteristics. The maximum RSD <1% and symbols have the same meaning as above.....	155
112. A0408: Pre- and post-irradiation gate leakage. Symbols have same meaning as above.....	156
113. A0408: Gate leakage recovery after 9-mos anneal. Symbols have same meaning as in previous figures.....	157
114. A0408: Recovery of gate leakage following a 9-mos RT anneal. Symbols have same meaning as in previous figures.....	157
115. A0409: GLADC I-V characteristics. The maximum RSD <2.5%. Symbols have same meaning as above.....	159
116. A0409: Non-GLADC I-V characteristics. Maximum RSD <2.5%. Symbols have same meaning as above.....	160
117. A0409: Increased gate leakage following a maximum dose of $3.67 \times 10^{15} \text{ e}^- \cdot \text{cm}^{-2}$. Symbols have same meaning as above.....	161
118. A0409: Annealing “super” recovery of gate leakage. Symbols have same meaning as above.....	162

List of Tables

Table	Page
1. Advantages of GaN-Based Transistors [17].	15
2. Al mole fraction dependent parameters for $\text{Al}_x\text{Ga}_{1-x}\text{N}/\text{GaN}$ MODFETs.	44
3. Parameter descriptions for Figure 25.	58
4. A25 PART Irradiation Experiment Summary (06JAN05).	81
5. A27 PART Irradiation Experiment Summary (10JAN05).	82
6. A29 PART Irradiation Experiment Summary (10JAN05).	83
7. A29 PART Irradiation Experiment Summary (10JAN05).	84
8. Comparison of total flux to 1 MeV Eq neutrons for Si and GaAs.	87
9. A25: Summary Table of Observed Schottky behavior.	94
10. A25: Summary Table of Observed Schottky behavior.	103
11. A27: Summary Table of Observed Schottky behavior.	108
12. A29: Change of gate leakage magnitude for 24 and 48 hr anneal.	112
13. A29: Summary Table of Observed Schottky behavior.	114
14. TE vs six-parameter fitting model.	145
15. Areal Richardson constant and Temperature-Independent SBH.	151
16. Second Irradiation Experiment Summary (28 January 2004) [29].	153
17. Percent increase drain current from pre-irradiation baseline measurement following irradiation and annealing, A0408.	154
18. Percent increase gate current from pre-irradiation baseline measurement following irradiation and annealing, A0408.	156
19. Percent increase drain current from pre-irradiation baseline measurement following irradiation and annealing, A0409 GLADC.	159

20. A0409: Percent increase drain current from pre-irradiation baseline measurement following irradiation and annealing, Non-GLADC.....	160
21. A0409: Percent increase gate current from pre-irradiation baseline measurement following irradiation and annealing.....	161

TEMPERATURE DEPENDENT CURRENT-VOLTAGE MEASUREMENTS OF
NEUTRON IRRADIATED $\text{Al}_{0.27}\text{Ga}_{0.73}\text{N}/\text{GaN}$ MODULATION DOPED FIELD
EFFECT TRANSISTORS

I. Introduction

Semiconductor electronics have penetrated nearly all aspects of human existence. Ubiquitous acceptance of such devices is attributable to unremitting evolutionary change. Consumer demand for faster, smaller, and more economical electronics has fueled near exponential growth in processing power. Radiation susceptibility, however, remains a fundamental attribute of semiconductor electronics that is principally extraneous to terrestrial users. Although terrestrial sources of radiation are typically negligible, device operation in the harsh space or nuclear radiation environment “can cause severe degradation of the device performance and of its operating life. These radiation effects are of both practical and scientific interest [1].”

III-V Nitride Revolution

Consisting of greater than one-fourth of the earth's crust by weight, Silicon (Si) has been the predominant choice of material for the microelectronics industry during the past half century. In addition to profuse availability, Si readily forms an insulating oxide and large crystal growth of pure Si is more economical and straightforward to that of other materials. Therefore, it logically follows that the preponderance of efforts and

advancements in material processes and radiation effects testing on semiconductors focuses on Si.

Although Si remains the accepted choice of material for most terrestrial uses, there are opportunities for specialty compound materials to evolve for niche aerospace, telecommunications, and high-power computing applications for use in radiation environments. Interest in these materials has greatly increased recently as commercial foundries struggle with diminishing returns on investments in attempts to further reduce Si device feature sizes. Unable to exploit economies-of-scale, hardened-by-design devices remain costly and inefficient [2].

Wide bandgap (WBG) III-V (group-III nitrides) material systems such as Aluminum Nitride (AlN), Gallium Nitride (GaN), and Aluminum Gallium Nitride (AlGaN), are fast gaining traction as practical cure-alls for applications that demand high-power, temperature-insensitive, fast, and radiation tolerant devices. Previously thought useful only as insulating materials, III-V materials specifically exhibit material properties that make it well suited to applications in harsh environments. Demonstrating high thermal conductivity, chemical inertness and exceptional mechanical stability, III-V semiconductors can function in environments where common silicon or gallium arsenide (GaAs) based devices will not operate or at least need to be protected by specially designed packages [3].

In addition to possessing favorable mechanical properties, III-V nitride material systems have large direct bandgaps that range from 4.2 eV for GaN to 6.2 eV for AlN, making them immune to many thermally activated processes [4]. Other favorable

electrical properties include large heterojunction conduction band discontinuities, high charged carrier saturation velocity, and low dielectric constants [5].

Because the study of III-V devices is still in its formative years, many reports offer only anecdotal evidence of dramatically improved radiation hardness. Bulk AlGaN and GaN is apparently more radiation hard than both Si and GaAs, primarily owing the hardness to the WBG and high nitrogen displacement energy [6]. Furthermore, published reports by various authors have all concluded that irradiated III-V-based devices exhibit more radiation hardness than both Si and GaAs-based devices [7], [8]. However, many reports are device and radiation dependent, providing coherent yet inconclusive results. Of particular interest is the effect of neutron irradiation on $\text{Al}_{0.27}\text{Ga}_{0.73}\text{N}/\text{GaN}$ modulation-doped field-effect transistors (MODFETs) with wide gate widths and 0.27 aluminum mole fraction. To date, there is no published report documenting the hardness of these transistor devices to neutron irradiation.

Given that many satellite systems are required to operate in the high radiation environment of space for between five to fifteen years, a clear understanding of radiation effects is essential for successful and confident integration of MODFETs into space-borne systems. Such an endeavor requires prior knowledge and characterization of device and material responses to radiation. In characterizing the problem, one must ask the following questions: What environment is the device likely to encounter, and how do radiation interactions within the device alter its behavior? Theory, modeling, and experimentation are employed as a threefold approach to answer these questions. It is now appropriate to establish the problem statement, which will be the focus of this thesis.

Problem Statement

What are the effects of 1 MeV Equivalent (Si) Neutrons on the transport mechanism of charged carriers within $\text{Al}_{0.27}\text{Ga}_{0.73}\text{N}/\text{GaN}$ MODFETs? Specifically, what is the temperature dependence of the current-voltage characteristics and what is the neutron damage constant of GaN for transconductance?

Hypothesis

The introduction of a high density of defect donors by neutron irradiation result in an increased two-dimensional electron gas, gate leakage, and drain current. Sufficiently high densities of donor defects cause total failure of the transistor action. Additionally, the introduction of dislocations and surface states significantly increase defect-assisted tunneling current through the Schottky contact and AlGaN layer. Limited by the creation, persistence, and location of defects, these particular AlGaN/GaN MODFETs are intrinsically radiation hardened with respect to Si or GaAs-based field-effect transistors.

Objectives

1. Determine the effects of a long-term room temperature anneal on previously electron irradiated $\text{Al}_{0.27}\text{Ga}_{0.73}\text{N}/\text{GaN}$ MODFETs.
2. Determine neutron fluences and doses that change MODFET operation and induce failure of transistor action.
3. Correlate radiation induced damage with possible change in carrier transport mechanism.
4. Determine the neutron damage constant of GaN for transconductance as a function of neutron fluence.
4. Determine post neutron irradiation annealing behavior.

Scope

This research is limited to a specific study on the effects that 1 MeV equivalent (Si) neutrons have on $\text{Al}_{0.27}\text{Ga}_{0.73}\text{N}/\text{GaN}$ MODFETs. Experimentation consists of current-voltage (I-V) measurements in the wide temperature range of 80-300 K. Irradiations within the Ohio State University Research Reactor (OSURR) are conducted at both 80 K and ambient core temperature. A determination of the dominant carrier transport mechanism at various neutron fluences is made along with the first ever neutron damage constant of GaN for transconductance. Other useful measurement techniques such as capacitance-voltage (C-V), Hall Effect, or deep level transient spectroscopy (DLTS) must be considered outside the scope of this study. Instead, all conclusions will be resolved from experimental results, modeling, and theoretical considerations as they relate to the transport of charged carriers from the gate metal interface through the AlGaN layer and into the conduction channel.

Approach

The approach of this research endeavor includes a threefold methodology of continuous theoretical development, modeling, and experimental measurements. Theoretical development primarily consists of utilizing and modifying existing theory to create a more complete representation of observed MODFET behavior. No new theoretical considerations are established. Instead, measurements are interpreted within the framework of existing knowledge, and applied innovatively. Modeling consists of fitting experimentally obtained Schottky diode current measurements to expected mechanisms of charged carrier transport over/through the Schottky barrier. Experimental

measurements involve a full suite of temperature-dependent I-V (I-V-T) characteristics including: drain and gate current, threshold voltage, transconductance, and the extraction of relevant Schottky diode parameters.

The overall measurement approach requires both pre- and post-irradiation characterization baselines. Initiated the day preceding an irradiation, measurements typically take 8-12 hours. The primary disadvantage of this technique is the risk of device breakage prior to irradiation and potential loss of preirradiation characterization baseline measurements. That is to say, twelve-hour lead-time is desired for all testing, however, compressed schedules dictate otherwise.

An initial approach to device irradiation requires a continuous irradiation and measurement capability at 80 K. Low temperature irradiations are desired to reduce thermally activated annealing effects within the semiconductor material. Within the framework of the radiation test plan, the initial approach involves irradiating-to-failure testing and subsequent irradiations to a fluence less than failure levels. The OSURR facility capable of accommodating *in situ* measurements at cryogenic temperatures is the beam port (BP). However, unless stringent radiation safety requirements are met, facility managers mandate an alternate approach.

One such alternate approach is the abandonment of the cryogenic and continuous measurement requirements. Irradiations conducted within the pneumatically actuated rabbit tube (PART) are accommodative of the relaxed requirements. When irradiating within the PART, the overall experimental approach is only slightly changed. Because devices are pneumatically transported close to the core, fluences are five

orders-of-magnitude (OOM) greater than the BP and temperatures only slightly elevated above 300 K (maximum temperature is approximately 305 K with a continuous circulation of 300 K ambient air.) Therefore, shorter irradiations can be conducted to achieve fluences in a wide range. The initial plan called for irradiations at extremely high neutron fluences in order to bracket a fluence region of interest. This method yielded results contrary to the previously stated assumption and no upper limit was found. Instead, at increasing fluences, annealing was accelerated and successive irradiations became less and less effective. At sufficiently high neutron fluences of 10^{15} to 10^{16} n-cm⁻², irradiations acted to anneal devices at a faster rate than damage could be introduced.

The final experimental approach was to return to the beam port and conduct *in situ* measurements at 80 K. Alterations to the experimental apparatus yielded a decreased radiation hazard. However, an anomalous electrical behavior was observed once the system was loaded into the beam port. Although this method is optimal, a combined failure mechanism of static-discharge damage to the heterostructure and packaging epoxy breakdown rendered this entire data set unusable.

Throughout the research endeavor, both irradiation approaches are utilized. Discussion of each individual irradiation run and methodology is described in Chapter IV.

Assumptions/Limitations

Throughout experimentation, assumptions based on accepted practices of radiation testing of electronics are made. They are:

- 1) *In situ* measurements are short with respect to overall irradiation time. Thereby the assumption of negligible accumulated dose during measurements is valid.
- 2) Accumulated dose from intended and unintended reactor power changes are negligible. During irradiation, negative feedback mechanisms tend to decrease overall RX reactivity and decrease power output. Therefore, all unintended power changes are conservative in nature. Additionally, intended power changes occur quickly on the time scale of irradiation times that may be hours in length.
- 3) Accumulated dose from fission gamma rays and gamma rays originating from within the device are negligible. During irradiation, gamma production from fission product decay and activation can add significant dose to a device. However, a simplifying assumption is that the device dimensions are significantly small in comparison to the mean free path of a gamma-ray and little energy is deposited in the region of interest.

Sequence of Presentation

Divided into six chapters and three supporting appendices, the thesis is laid out in a manner in which a reader with an average understanding of semiconductor physics will find this document comprehensible. Chapter I is a cursory introduction to AlGaN/GaN MODFETs and is intended to give the reader a big-picture overview of the motivating factors for conducting this research endeavor. Chapter I includes the information necessary to determine what the research is attempting to answer, the scope of the research, assumptions necessary to conduct the experiment, and the author's hypothesis. Chapter II is an elucidation of the current state-of-technology relevant to this discourse. Included is further explanation for the motivation of using AlGaN/GaN MODFETs and summaries of current or critically important radiation effects studies that provide context for results reported within this document. Chapter III details the theory behind AlGaN/GaN MODFET charge control and Schottky gate contacts. Chapter IV provides important experimental procedures including details of the fabrication process, irradiation experiments, and dosimetry. Chapter V presents the results of the irradiations and provides relevant analysis and discussion. Finally, the conclusions and recommendations for further work are presented in Chapter VI. Appendix A presents a table of common GaN and AlN parameters. Appendix B contains a tutorial on Schottky diode parameter extraction methods. Since typical methods have many limitations, an alternate Schottky contact charge carrier transport model is introduced and explained in full detail. Appendix C contains the results of an annealing study conducted at 80 K following a nine-month room temperature anneal.

II. Current State of Technology

Purpose

Although a complete literature review has been conducted, not all of the literature review objectives are presented in this format. However, within the present chapter, a review of the current state-of-technology is presented along with a summary of relevant irradiation studies.

The Need for Group-III Heterostructures

The continuous need for high speed, high-power-density electronic devices requires analysis of advanced structures on new semiconductor materials. Among those materials are GaN, indium nitride (InN), and AlN of the group-III nitride family of semiconductors. When alloyed with their ternary and quaternary alloys, a new class of material systems with bandgaps that range from 1.9 to 6.2 eV becomes possible. Furthermore, the wide direct bandgap is ideal for band-to-band light generation, making group-III nitrides particularly advantageous for the fabrication of optoelectronic devices such as short wavelength light emitting diodes (LED) and lasers working in the blue and near ultraviolet (UV) spectral ranges [9]. In addition to the optoelectronic applications of the III-V nitrides, radio and microwave frequency high-power-density transistors may become the enabling technology for myriad of sophisticated systems such as broadband wireless networks, electric hybrid vehicles, compact collision avoidance radars for vehicles, and others. Exhibiting low thermal generation rates, a high breakdown field (>5 MV/cm), high saturation velocity, and the ability to operate at frequencies up to 140 GHz, nitride systems are an important endeavor for the military, with particular

regard to radiation hardened terrestrial and space systems. The ability to operate such devices in high temperature, high power/voltage, and radiation environments is critical. To date, no material/device combination can satisfy all of these requirements.

A wide bandgap alone does not make a good semiconducting material. Other figures of merit, such as the intrinsic carrier concentration and mean displacement energy (E_d) are both essential descriptors of the robustness and advantage of group-III nitrides over traditional material systems. Figure 1 illustrates the temperature dependency of various frequently used semiconductor materials, showing that nitride semiconductors are more robust at higher temperatures and in a wider range than their commonly used counterparts Si and GaAs. Figure 2 shows the empirical relationship of the displacement threshold energy with reciprocal lattice constant. Each figure clearly demonstrates the advantage of group-III nitride materials with respect to traditional semiconductors in terms of both temperature and purported radiation hardness, respectively.

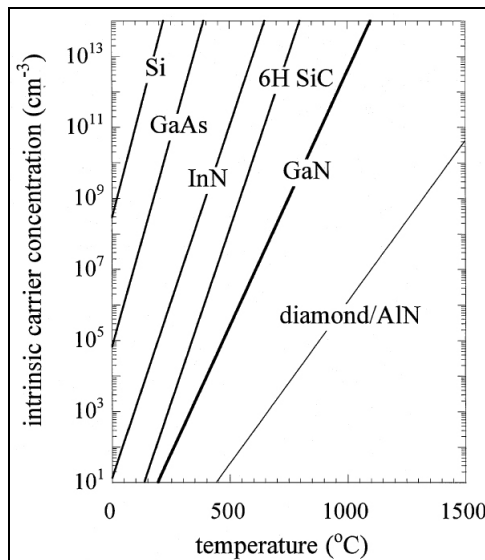


Figure 1. Intrinsic Carrier Concentration of commonly used semiconductor materials [10].

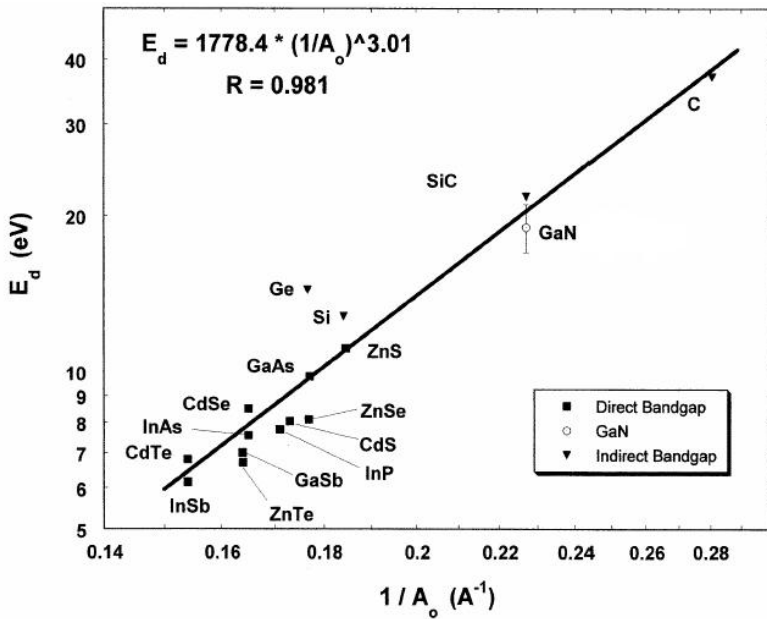


Figure 2. Empirical relationship between E_d and reciprocal lattice constant [11].

Recent advancements in the understanding of fundamental device physics operation and materials processing techniques have made a wide array of group-III nitride heterostructures possible. These include surface-acoustic wave devices, solar blind UV detectors, Bragg reflectors, waveguides, UV and visible LEDs, laser diodes, and quantum devices such as high electron mobility transistors [12].

An application under intense investigation is sensing. Sensing is a multifaceted discipline requiring both passive and active systems to characterize some predetermined parameter of interest. Often, difficulties arise when the signal of importance lies in a narrow band, signal intensity changes by OOM, the environment is awash with ambient radiation, and the environment is harsh and uncontrollable. Many times, surviving the inhospitable environment can be the main obstacle to successful sensor deployment and excessive ancillary protection equipment can make an entire design prohibitive.

The large band gap of GaN and other nitride semiconducting materials ensure that problems from unwanted thermal or optical interferences are minimized [13]. “UV sensors that operate in the solar blind region (260-290 nm) have high detectivity because the ozone layer absorbs solar radiation at those wavelengths, thus virtually eliminating the radiation noise [12].” In addition to being able to detect terrestrial sources of UV radiation, the APA Optics Group demonstrated a three OOM drop in responsivity over 10 nm (past the desired wavelengths) for their UV sensitive detector [12]. The high selectivity of GaN in comparison to silicon-based devices negates the need for bulky supplementary filtering equipment, freeing valuable platform space [12]. Another distinctive advantage of GaN UV detectors is the so called ‘automatic gain control’. Honeywell has demonstrated a detector design in which the gain decreases rapidly with increasing UV intensity and has very low resistance at low light levels [12]. Additionally, strong chemical bonding between Gallium and Nitrogen widens the forbidden gap in the electronic density of states, giving rise to exceptionally advantageous mechanical, thermal, and chemical stability [14].

Currently, the most commercially viable application of III-V semiconductor materials is in the area of light emitting diodes. Until recently, applications of LEDs were limited by their inability to produce intense light as well as their limited range of wavelengths. However, LEDs have undergone a tremendous advancement in performance and now are compact, reliable, inexpensive light sources.

The primary advantage of GaN LEDs is that there is a direct energy bandgap for optical emission. Meaning, the highest energy point of the valence band is directly below

the lowest energy point of the conduction band at the same value of momentum. Energy released during band-to-band electron-hole (e-h) recombination is converted primarily into radiation (radiant recombination) of wavelength determined by the energy gap. Although the band-edge emission of GaN is in the UV region, appropriate alloying with nitrides such as AlGaN or InGaN pushes the emission into the yellow or even red. The new breed of GaN-based LEDs exhibit brightness levels and longevities that exceed the requirements for many high demand applications. For the first time, full color, all semiconductor displays are possible when red LEDs are combined with blue and green [15]. Furthermore, by covering LEDs with phosphorescent dye, white light LEDs with an equivalent blackbody temperature of 6000 °C are possible [16]. When used in place of incandescent light bulbs, group-III nitride based LEDs consume 80-90% less power, last ten times as long, and produce virtually no waste heat [12].

Although LEDs currently represent the primary market for GaN, the coming years will see rapid expansion and integration of both radio and microwave frequency nitride transistors. Silicon and GaAs control nearly 100% of the \$5 Billion USD radio and microwave frequency semiconductor market [16]. However, because group-III nitrides exhibit superior material properties, the total GaN electronic-device market is expected to reach \$500 million USD by the end of this decade. Radio frequency (RF) and microwave applications are likely to be the largest share of the GaN device market, targeting both military and commercial applications. Table 1 describes the competitive advantages of GaN devices over conventional technologies such as Si or GaAs-based devices. In every single category, GaN devices excel over conventional technology.

Table 1. Advantages of GaN-Based Transistors [17].

Need	Enabling Feature	Performance Advantage
High Power/Unit Width	Wide Bandgap, High Field	Compact, Ease of Matching ^a
High Voltage Operation	High Breakdown Field	Eliminate/Reduce Step Down ^b
High Linearity	MODFET Topology	Optimum Band Allocation
High Frequency	High Electron Velocity	Bandwidth, μ -Wave/mm Wave
High Efficiency	High Operating Voltage	Power Saving, Reduced Cooling ^b
Low Noise	High Gain, High Velocity	High Dynamic Range Receivers
High Temperature Operation	Wide Bandgap	Rugged, Reliable, Reduced Cooling
Thermal Management	SiC Substrate	High Power Densities with Reduced Cooling Needs
Technology Leverage	Direct Bandgap Allows for Lighting	Driving Force for Technology; Low Cost

^a “The high power per unit width translates into smaller devices that are not only easier to fabricate, but also offer much higher impedance. This makes it much easier to match them to the system, which is often a complex task with conventional devices in GaAs (for e.g., a matching ratio ten times larger might be needed for a GaAs transistor, increasing overall complexity and cost) [17].”

^b “The high-voltage feature eliminates or at least reduces the need for voltage conversion. Commercial systems (e.g., wireless base station) operate at 28 V and a low-voltage technology would need voltage step down from 28 V to the required voltage. However, GaN devices can easily operate at 28 V and potentially up to 42 V. The higher efficiency that results from this high operating voltage reduces power requirements and simplifies cooling, an important advantage, since cost and weight of cooling systems is a significant fraction of the cost of a high-power microwave transmitter [17].”

The need for GaN-based heterojunction devices is clear and their importance to the DoD and private sectors are enormous. Group-III nitride compound semiconductors far exceed the physical properties of silicon and “as a result, its capabilities - such as amplifying (without distorting) high-frequency RF signals, withstanding high temperatures, emitting blue and green light - make GaN ideally suited for a wide range of electronic and optoelectronic applications [18].” As seen in Figure 3, the commercial applications for Gallium Nitride are wide-ranging and nearly limitless. Although commercial integration of GaN-based devices can occur on a short timescale, militarization requires further investigation before its benefits are accepted. Additionally, the use of GaN-based devices in radiation rich environments necessitate a greater understanding of their radiation response, warranting additional studies.

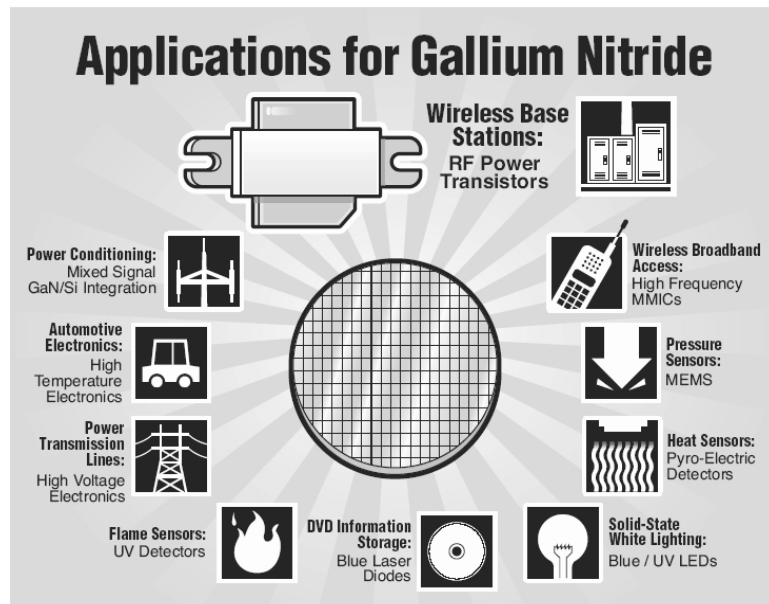


Figure 3. Potential Applications of GaN-based devices [18].

Radiation Effects on $\text{Al}_{0.27}\text{Ga}_{0.73}\text{N}/\text{GaN}$ Heterostructures

Previous radiation characterizations conducted on various group-III nitride materials have revealed intrinsic radiation hardness. However, the distinction between material radiation hardness and device radiation hardness is often lost on those not intimately familiar with radiation effects in complex material systems. The review of the current state-of-technology will focus on device level testing of AlGaN/GaN heterostructure devices. Results of previous material testing are integrated into the discussion of device behavior as appropriate.

Although there have been advancements in the fundamental understanding of some aspects of MODFET operation, overall, the results can best be described as inconclusive (see the following sections pertaining to various irradiation experiments). Most previous efforts have focused on proton irradiations with less frequent discussion of photon, electron, and neutron radiation studies. In fact, to date, no device-level neutron irradiation studies have been published on AlGaN/GaN MODFETs. Additionally, there is a noticeable dearth of information regarding the current transport mechanisms in AlGaN/GaN heterostructures and radiation induced changes.

Since no means of mass producing high-quality AlGaN/GaN MODFETs has been formulated, it comes to no surprise that radiation damage studies are often device dependent and frequently raise more questions than they answer. However, it is particularly noteworthy to mention one irregularity that is present in all radiation studies of GaN-based devices. Namely, although the presented results are commonly in opposition to each other (i.e. drain-to-source current increase/decrease, Schottky barrier

height increased/decreased, threshold voltage shift direction and magnitude, etc.), the common consensus is that GaN-based heterostructures are radiation hard. That is to say, whether authors observe contradictory results or not, both are able to argue the intrinsic radiation hardness of GaN. The following sections broken down by radiation type will be my attempt to summarize the current state of radiation testing on GaN-based devices. In no way can this be a complete regurgitation of all previous radiation testing on AlGaN/GaN devices. Instead, only articles of key importance are highlighted.

Photon Radiation

GaN-based devices exhibiting high power/temperature capabilities are of interest for space-borne applications such as satellite communication systems in addition to the nuclear industry and military uses. Therefore, it should come to no surprise that some of the earliest radiation experiments sought to characterize the ionizing radiation response of AlGaN/GaN MODFETs.

“The mechanism of damage creation by gamma photons is well known. At the energy of ^{60}Co gamma photons, the interaction of gamma radiation with the material occurs mainly through generation of high energy Compton electrons, which in turn dissipate their energy through various mechanisms creating a large number of secondary electron-hole pairs. ... The secondary carriers’ main influence on the device behavior occurs by changing occupancy of traps in insulating layers. ... In addition to the effects of secondary carriers, displacement of atoms may also result from the absorption of a gamma photon through interaction of the Compton electron with nuclei. The displacement damage results in reduction in carrier lifetimes at low doses and reduction in mobility and compensation of dopants at higher doses. Previous investigations of the effects of ^{60}Co radiation ... has shown that the irradiation results in generation of defects, with the defect creation rates depending on sample quality and doping level. Possible creation of nitrogen vacancies and desorption of nitrogen from [the] surface were indicated. It was suggested ... that irradiation results in simultaneous generation of mutually compensating defects. A possible candidate is the generation of nitrogen vacancies, and interstitials. ... The generation rates for these defects were found to be the same. Theoretical studies have also shown that

nitrogen vacancies create donor states in the conduction band, and the interstitials create acceptor states in the mid-gap [19].”

Using a ^{60}Co gamma source, Luo *et al.* irradiated MODFETs of different gate dimensions up to 600 Mrad total gamma dose at 298 K [20]. At doses less than 300 Mrad, little change in the reverse breakdown voltage (V_b), threshold voltage (V_{th}), or transconductance (g_m) was observed [20]. However, at the maximum dose of 600 Mrad, V_b became more negative by a factor of two, V_{th} shifted negative an unspecified magnitude, g_m decreased 20-45% depending on the gate dimensions, and the saturation drain-source current (I_{ds}) increased slightly [20].

Post irradiation I-V characteristics show that “gate leakage is significantly decreased in the low-bias region ($< 0.5\text{ V}$) where surface generation recombination is dominant and also at higher voltage, due to an increase in channel resistance [20].” It can be shown that the resistivity of the GaN layer is inversely proportional to both the carrier density and electron mobility in the two-dimensional electron gas (2DEG). Therefore, a decrease in either parameter will result in an increase in resistivity. Luo *et al.* asserts that the decrease in V_b is consistent with a reduction of effective doping in the 2DEG due to radiation induced deep state trapping [20].

Figure 4 illustrates the transfer characteristics for a $1.2 \times 200\text{ }\mu\text{m}^2$ MODFET pre and post gamma irradiation. The threshold voltage is given by Equation 1.

$$V_{th} = V_{bi} - e^{(N_d + N_T)a^2/2\varepsilon} \quad (1)$$

where V_{bi} is the built-in voltage, N_d is the donor density in AlGaN, N_T is the trap density, a is the active layer thickness, and ε is the dielectric constant. Therefore, in

order for the threshold voltage to increase in magnitude, the net of $N_d + N_T$ must also increase [20]. The net term of $N_d + N_T$ is trap density dominated [20]. Figure 4 illustrates a decrease in the maximum extrinsic transconductance. Since the transconductance can be represented as $\delta I_d / \delta V_g$, the decrease must originate from a reduced drain current. Luo *et al.* theorizes that the reduced drain current is due to a reduction of carrier density in the 2DEG. This is consistent with their assertion that a decrease in either the carrier mobility or carrier density is the mechanism responsible for the decrease in V_b [20].

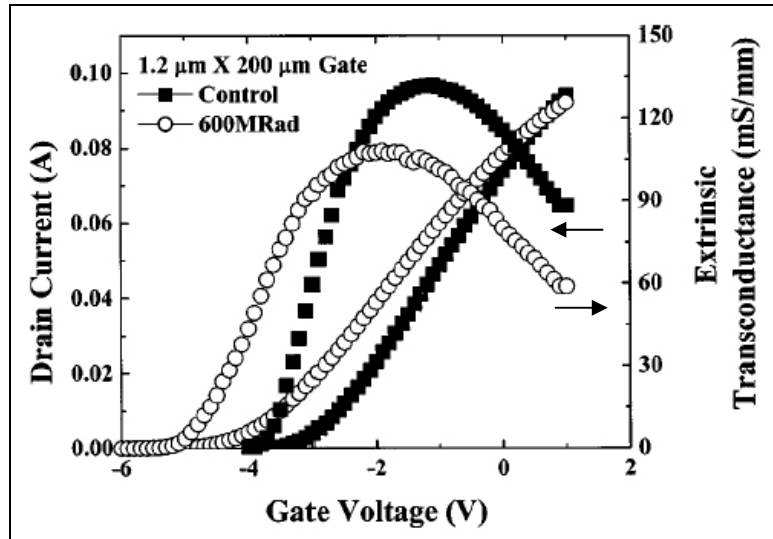


Figure 4. Transfer characteristics for a $1.2 \times 200 \mu\text{m}^2$ MODFET pre and post 600 Mrad total dose gamma irradiation [20].

In addition to the aforementioned effects of gamma irradiation, the authors observed a ‘slight’ increase in the drain-source saturation current (Figure 5). Remaining self-consistent in their reasoning, Luo *et al.* suggest that I_{ds} increases due to increased GaN resistivity. The increased resistivity reduces the gate bias seen by the 2DEG due to screening by the high resistance AlGaN layer [20]. A decrease in the initial slope of I_{ds} at

low biases accompanied the increase of I_{ds} at higher gate biases, suggests a change in either the carrier mobility or density [20].

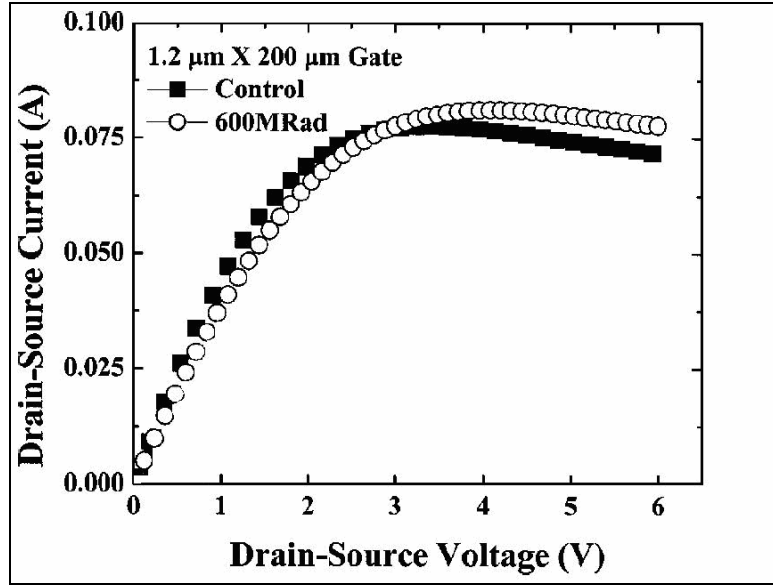


Figure 5. I_{ds} - V_{ds} characteristics for a $1.2 \times 200 \mu\text{m}^2$ MODFET pre and post 600 Mrad total dose gamma irradiation [20].

The variation of gate dimensions has a pronounced effect on both V_b and g_m . For a gate length of $1.2 \mu\text{m}$, at 600 Mrad total dose, V_b decreased by a factor of nearly three when the gate width was decreased from 200 to $100 \mu\text{m}$. Similarly, g_m decreased by a factor of three for the same change in gate width. Both relationships are nearly linear [20].

In attempting to draw decisive conclusions from the results published by Luo *et al.*, two difficulties arose that limit direct comparisons to other publications: sample specific results and missing dosimetric information. As stated previously, manufacturability is a fundamental issue preventing widespread deployment of GaN-based devices. This leads to experimental results that are highly dependent on the

specific device structure, Aluminum molar fraction, contact types, material quality, processing methods, and particularly transistor dimensions. Secondly, dosimetric information is incomplete and the experiment cannot be replicated or independently verified. Units of dose must be related to a specific material. A ‘rad’ is the amount of energy deposited in a material (i.e. Si or SiO₂ is typically referenced). Additionally, proper dosimetric information must include the rate at which the energy is deposited. Since this basic information is lacking, the stated doses may be off by a factor of two and specific dose rate effects cannot be addressed. This shortcoming is not isolated to the referenced research. One study that attempts to address these issues is by Aktas *et al.*

Aktas *et al.* irradiated Silicon nitride (SiN_x) passivated AlGaN/GaN MODFETs with ⁶⁰Co gamma rays to a total dose of 600 Mrad (Si) at 343 K. Using dosimetric polymer films, the nominal dose rate was determined to be about 2 Mrad (Si)/hr [19]. Overall, the I-V and g_m characteristics exhibited similar behavior to that reported by Luo *et al.*. This can be seen in Figure 6 and Figure 7.

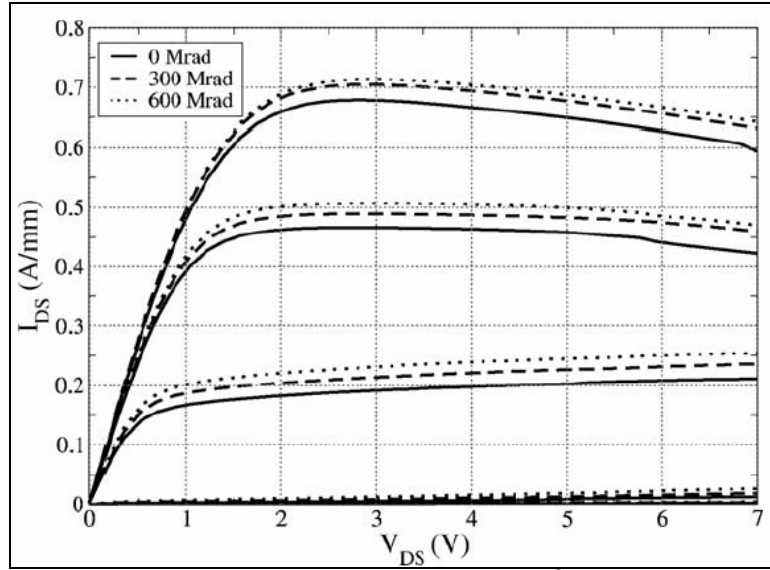


Figure 6. I_D - V_{DS} characteristics of a $0.25 \times 150 \mu\text{m}^2$ AlGaN/GaN MODFET at various gamma irradiation doses [19].

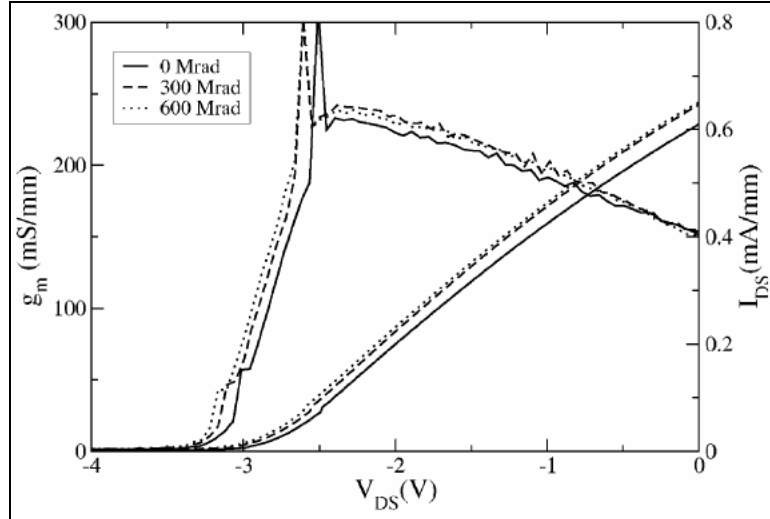


Figure 7. Transfer characteristics of a $0.25 \times 150 \mu\text{m}^2$ AlGaN/GaN MODFET at various radiation doses. The anomalous spike is an artifact of taking the derivative of the saturation drain current as a function of the gate voltage [19].

Aktas *et al.* report a maximum V_{th} shift of -0.1 V and a maximum g_m decrease of only 3%. In conjunction with the threshold voltage shift, the saturation current at constant gate bias also increased [19]. Luo *et al.* suggested that the changes were due to a *decrease*

in effective carrier density in the 2DEG. In contrast, Aktas *et al.* hypothesized an *increased* carrier density is responsible. In order to determine the mechanism of radiation-induced changes, Aktas *et al.* used Hall Effect and Transmission Line Method (TLM) measurements to gain further insight. Surprisingly, the sheet carrier density remained constant at all doses. The contact resistance, sheet resistivity, and Hall mobility exhibited no significant changes at all doses up to 600 Mrad (Si) [19]. In order to explain these phenomena, Aktas *et al.* suggests that the threshold voltage shift is due to an increase in carrier density that is localized under the gate [19].

“Depending on the AlGaN mole fraction and the thickness of the AlGaN layer, the band alignment may be such that the acceptors would be negatively charged under the SiN_x passivation, but be partially neutral close the metal interface under the gate. Thus, under the gate, some of the donors generated by irradiation will contribute electrons to the channel. The reduction in mobility through remote and local ionized impurity scattering would be limited, since the fields from the compensating defects will tend to cancel each other far away from the defects. From this model, we also see that the effect of radiation may depend on the parameters of the AlGaN barrier layer [19].”

This model depends on the assumption of mutually compensating acceptor and donor defects that have been previously reported by Look *et al.* [21].

Aktas *et al.* has formulated a theory to explain the increased drain current by hypothesizing an increase in carrier density locally below the gate. The hypothesis is based on experimental data obtained from SiN_x passivated AlGaN/GaN MODFETs. However, a recent study conducted by Mishra *et al.* does not report the same drain current behavior as seen by Aktas *et al.*, but does support measurements of both constant carrier concentration and mobility [22].

Mishra *et al.* irradiated both passivated and unpassivated (0.7 and $0.5 \times 100 \mu\text{m}^2$ gate dimension respectively) AlGaN/GaN MODFETs to total doses from 1.5 to 20 Mrad (Si) at a nominal dose rate of 2krad (Si)/min at 300 K [22]. The authors report that the passivated device had an approximately 12% decrease in drain current at 5 Mrad (Si) compared to an 8% drop for the unpassivated device. Both devices showed nearly the same gate leakage increase of approximately 200% at 10 Mrad (Si) total dose [22].

The radiation hardness of GaN to ionizing radiation is nearly an accepted fact. That is, radiation-induced defect production rates for GaN are lower than for Si and GaAs [22]. It can be seen in Figure 8 that 10 keV x-rays have little effect on the transfer characteristics or g_m up to a total dose of $30 \text{ Mrad (SiO}_2)$ in AlGaN/GaN MODFETs [23]. A study conducted by Umana-Membreno *et al.* reports findings that support this supposition. GaN is intrinsically radiation hard, but device hardness may be limited by the electrical contacts [24].

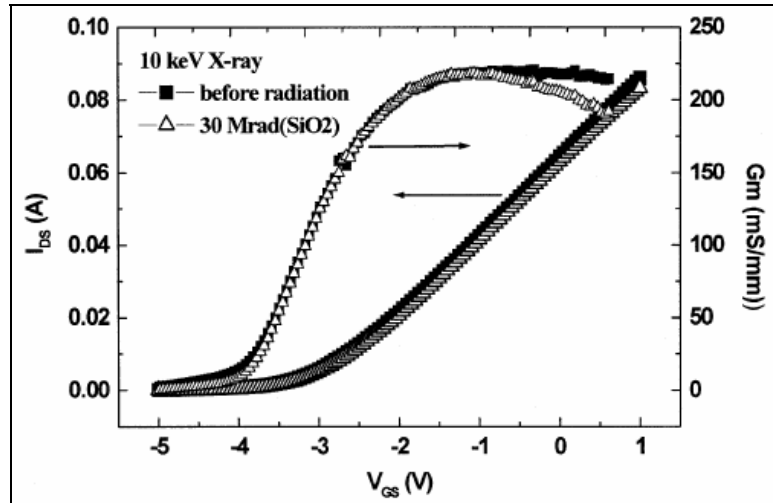


Figure 8. Transfer characteristics for AlGaN/GaN MODFETs before and after 10-keV X-ray irradiation at fluences up to $30 \text{ Mrad (SiO}_2)$ [23].

Using a combination of I-V, C-V, and DLTS measurements, Umana-Membreno *et al.* was able to characterize the radiation response of Ni/n-GaN Schottky diodes. The authors found that the Schottky barrier height (SBH) extracted from C-V measurements (ϕ_B^{C-V}) increased a maximum of 15% at a total dose of 21 Mrad (Si) and the barrier height extracted from I-V measurements (ϕ_B^{I-V}) remained unchanged at all doses [24]. This analysis presumes an intimate, homogeneous and defect-free metal-semiconductor (m-s) junction, which is typically not the case. Non-idealities are thought to arise from effects associated with metal-induced gap states, dislocation-related leakage paths, and interfacial defects. The high density of dislocations act as efficient current leakage paths that increase total current transport (so called defect-assisted tunneling). Thus, the true SBH is underestimated and the ideality factor becomes greater than unity for pure ballistic injection over a potential barrier.

Radiation induced defects were monitored using isothermal DLTS. Upon irradiation, three defects with activation energies of 88, 104, and 144 meV were produced at a combined rate of $2.12 \times 10^{-3} \text{ cm}^{-1}$. These defects are consistent with the activation energies of nitrogen-vacancy-related defects found in electron irradiated n-GaN diodes [24]. In addition to the aforementioned radiation-induced defects, three deep-level defects with activation energies of 265, 355, and 581 meV were detected within the sample prior to irradiation. However, these defects did not manifest any noteworthy change in concentration during irradiation up to a total dose of 21 Mrad (Si) [24].

Mishra *et al.* report work on gamma-irradiated *n*-GaN Ni/Au Schottky diodes. The accumulated total dose ranged from 0.2 to 21 Mrad (Si) at a dose rate of 2 krad/min

[25]. The reverse I-V characteristics showed degradation for doses above 5 Mrad (Si) and at the maximum dose of 21 Mrad (Si) the reverse leakage current density increased nearly four OOM [25]. In addition to the tremendous degradation of the reverse I-V characteristics, the SBH increased from 1.14 eV to 1.30 eV at 300K for a 21 Mrad (Si) total dose [25]. Finally, Mishra *et al.* reported the ability to anneal out the reverse I-V degradation at low temperature with no effect on the radiation induced defects. However, the increased SBH is persistent to temperatures greater than 350 °C [25]. This study illustrates the importance of whole device testing in conjunction with material testing.

Subsequent studies on the effects of gamma radiation on AlGaN/GaN Schottky structures and MODFETs have provided strong evidence that the GaN material is intrinsically hard and that the degradation of device characteristics is highly dependent upon electrical contacts at the metal gate/AlGaN interface.

Electron Radiation

Ionascut-Nedelcescu *et al.* observed the radiation hardness of GaN LEDs and films and reported a two OOM increase of radiation hardness of GaN when compared to GaAs [11]. Ionascut-Nedelcescu *et al.* attribute this radiation hardness to strong bond between Gallium and Nitride.

“A measure of this bond strength is the energy required to displace an atom from its lattice position or simply the atomic displacement energy, denoted by E_d . This parameter has been measured in several semiconductors and empirically determined to be inversely proportional to the volume of the unit cell. ... Independent of this empirical method, it was deduced by analyzing the transport properties of electron-irradiated GaN films, that E_d (Ga) is 20.5 eV and E_d (N) 10.8 eV. In the case of GaAs, E_d was directly measured and found to be 9.8 eV [11].”

Ionascut-Nedelcescu *et al.* set out to determine E_d for GaN by irradiating with relativistic electrons. The method entailed measuring the displacement damage constant associated with the electroluminescence signal as a function of electron energy. By determining the electron threshold energy for damage creation, E_d could then be deduced. The authors obtained a threshold energy of 440 keV, which corresponded to an E_d value of 19 ± 2 eV [11]. As you can see from Figure 2, the experimental value of GaN falls within the expected range when using only the reciprocal of the lattice constant. The empirical relationship and experimental results both support the assertion that GaN is a radiation hard semiconductor material.

Additional authors have published results from experiments on electron irradiated GaN. They include Z-Q Fang *et al.*, D.C Look *et al.*, and S. A. Goodman *et al.* to name a few. Through a series of papers entitled “Deep centers in as-grown and electron- irradiated n-GaN” [26], “Defect Donor and Acceptor in GaN” [21], “On the Nitrogen Vacancy in GaN” [27], and “Electron irradiation induced defects in n-GaN” [28], the authors were able to identify defects created by electron irradiation and classify them as either shallow or deep and as either acceptor or donors. Fang *et al.* discovered that 1 MeV electrons are capable of creating nitrogen vacancy (V_N) related centers with thermal activation energies of 0.06 eV [26]. Look *et al.* studied the effects of high-energy (0.7-1 MeV) electron radiation on GaN and observed that irradiation produced shallow donors and deep or shallow acceptors at equal rates [21]. Additionally, Look *et al.* were able to determine that an electrically active dominant defect in GaN

could be produced by 0.42 MeV electrons. The defect is a 70 meV donor and is most likely an isolated nitrogen vacancy [27].

Although these studies offer great insight into the radiation hardness of GaN, device level testing is necessary in order to evaluate the hardness of GaN-based devices for integration into complex systems. As part of an intensive study, J.M. Sattler conducted the first ever study of the effects of electron irradiation of AlGaN/GaN MODFETs. J.M. Sattler irradiated AlGaN/GaN MODFETs at 80 K with 0.45 to 1.2 MeV electrons to fluences up to $6 \times 10^{16} \text{ e}^- \text{-cm}^{-2}$. Following irradiation, low temperature I-V measurements were recorded, providing dose-dependent measurements. Additionally, I-V-T measurements were made following room temperature (RT) annealing [29]. J.M. Sattler reported three significant radiation induced changes in AlGaN/GaN MODFETs: 1) increased gate current, 2) increased drain current, and 3) RT annealing of induced damage.

Through a process of deduction and elimination, Sattler proposes an explanation for the increased gate current. Sattler reasoned that defect-assisted tunneling is more likely the dominant transport mechanism than that of either direct tunneling or thermionic emission [29]. Sattler makes an assumption that the traps are uniformly distributed throughout the AlGaN layer and that they are located in an energy band within the barrier height. This assumption is supported by a study conducted by Karmalkar *et al.* [30]. Additionally, in a study of ohmic contacts to AlGaN/GaN heterostructures, Qiao *et al.* found that tunneling of electrons from the 2DEG can dominate carrier transport across the AlGaN barrier layer [31]. Additional supporting evidence is reported by Khan *et al.*,

who reported a six OOM reduction in gate leakage resulting from the integration of an oxide region between the gate contact and the AlGaN layer in metal-oxide-semiconductor heterostructure field-effect transistors (MOS-HFETs) [32]. The addition of an oxide layer and subsequent reduction in gate leakage is evidence that the AlGaN layer is vulnerable to carrier transport.

From these findings Sattler concludes that the increase in gate leakage is caused by radiation-induced trap creation [29]. Although the nature of the traps is unknown, the electron energy was sufficiently high enough to cause trap creation throughout the AlGaN layer. “Furthermore, because electrons have an extremely low non-ionizing energy loss (NIEL) it can be assumed that the activation energy of these traps is low [29].” Nozaki *et al.* report discovering AlGaN traps with an activation energy of only 0.28 eV [33]. Therefore, it is probable that this particular low energy trap or similar yet-to-be discovered traps are created in the AlGaN layer by low energy electron radiation.

Sattler reports that the second major radiation effect observed was the large increase in drain current. Sattler narrows down the reason for increased drain current to two possibilities: 1) an increase in carrier concentration of the 2DEG, or 2) the carrier concentration remained unchanged but the carrier mean velocity of the 2DEG increased [29]. Since various authors have reported a relatively constant carrier concentration throughout irradiation, by process of elimination, the carrier mean velocity of the 2DEG is expected to increase. Other authors have consistently observed behavior in opposition

to that of J.M. Sattler and a definitive mechanism responsible for these differences has yet to be proposed.

The third major radiation effect observed was the ability to anneal out radiation-induced damage at RT. The annealing behavior supports Sattler's assertion that low activation energy traps created within the AlGaN layer are responsible for the increased drain current and subsequently annealed out at higher temperatures [29].

Appendix C contains a study of the annealing effects following a nine-month anneal. The characterized devices are those previously irradiated by J.M. Sattler.

Proton Radiation

Luo *et al.* conducted a device specific investigation on the effects of 40 MeV protons on AlGaN/GaN MODFETs [34]. Their motivation is geared toward the application of these devices in low earth orbit (LEO) assets. Therefore, doses equivalent to over 100 years in LEO were delivered to the devices [34]. Clearly, no thought was given to the dose rate effect to these devices. I can only surmise that Luo *et al.* used fluxes much too high to be comparable to the actual space environment. Nevertheless, Luo *et al.* report a greater than 30% decrease in g_m , decrease in reverse breakdown voltage, decrease in I_{ds} , and decrease in gate leakage at low gate biases. Post irradiation annealing at 300 °C resulted in a nearly 70% recovery of the initial g_m and I_{ds} values and the devices still exhibited transistor action [34]. The authors attribute the damage to a decrease in carrier concentration of the 2DEG and an increase in the 2DEG resistance from the creation of deep electron traps.

White *et al.* examined the effects that 1.8 MeV proton irradiation (nominally 300 K) had on AlGaN/GaN MODFETs [35]. Figure 9 shows the MODFET source-drain I-V characteristics before irradiation and after two successive proton exposures. It can be clearly seen that the proton irradiation induces a decrease in the saturation drain current. Figure 10 shows plots of both drain-source current and transconductance vs. gate-source voltage. Using DLTS, White *et al.* concluded that proton-irradiation creates spatially localized changes in the electronic properties of the heterostructure. Both a reduction of the internal electric field strength and creation of charged defects in the AlGaN layer were noted [35]. These defects directly reduce the charge density along the 2DEG in addition to decreasing the saturation current. White *et al.* hypothesize that reduction of electron concentration within the 2DEG is responsible for the decreased saturation current, drain current, and transconductance [35].

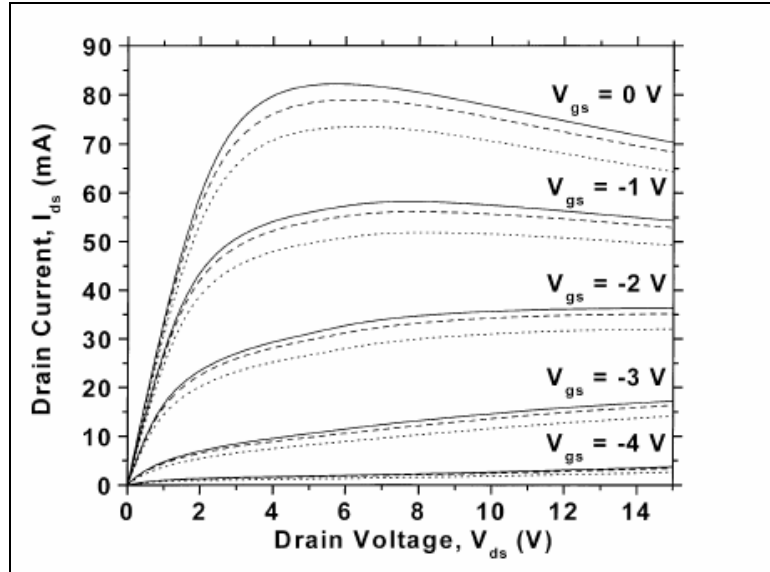


Figure 9. Common-Source I-V Curves - Pre-Irradiation (Solid Curves), Post $10^{11} \text{ p}^+ \cdot \text{cm}^{-2}$ (Dashed Curves), and Post- $10^{12} \text{ p}^+ \cdot \text{cm}^{-2}$ (Dotted Curves) [35].

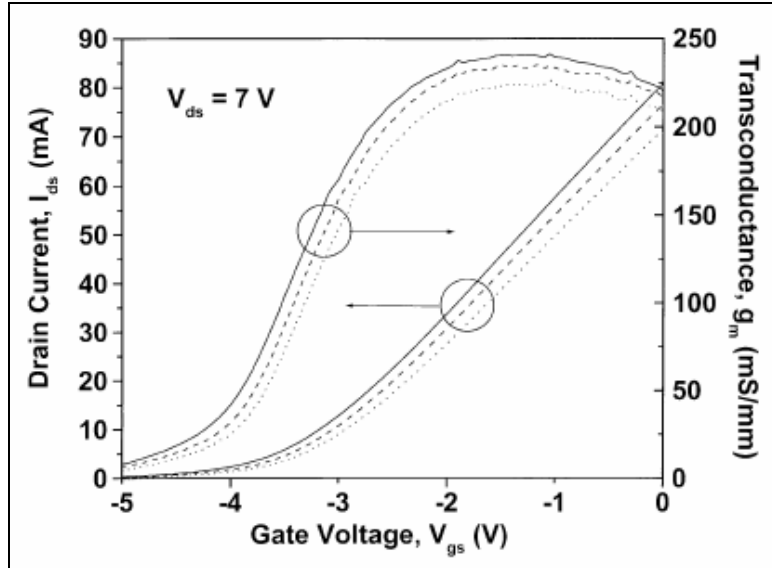


Figure 10. Transfer characteristics and g_m . Pre-Irradiation (Solid Curves), Post $10^{12} \text{ p}^+ \cdot \text{cm}^{-2}$ (Dashed Curves), and post $5 \times 10^{12} \text{ p}^+ \cdot \text{cm}^{-2}$ (Dotted Curves) [35].

In follow-up work, White *et al.* again characterized 1.2 MeV proton irradiated MODFETs and corresponding unprocessed materials. Irradiation was carried out at RT and all measurements made approximately one week later. White *et al.* again observed decreasing drain saturation current with increasing proton fluence (Figure 11). The transistor is essentially operational until $10^{15} \text{ p}^+ \cdot \text{cm}^{-2}$. Also shown in Figure 12, is the catastrophic drop-off in g_m and increase in V_{th} as a function in increasing fluence. Utilizing the same model presented as Equation 6, White *et al.* hypothesize partial changes in the quantities of the SBH, donor/acceptor concentration, conduction band discontinuity, and polarization sheet charge density. Small changes in the net polarization and/or various degrees of relaxation fully account for the observed shift in V_{th} up to $10^{15} \text{ p}^+ \cdot \text{cm}^{-2}$. Fluences greater than this require a greater than 60% reduction in polarization charge to account for the threshold voltage shift. However, the measured

reduction in sheet charge does not support this supposition (Figure 13). Therefore, White *et al.* conclude that the observed degradation in saturation current and transconductance is a result of decreasing channel mobility.

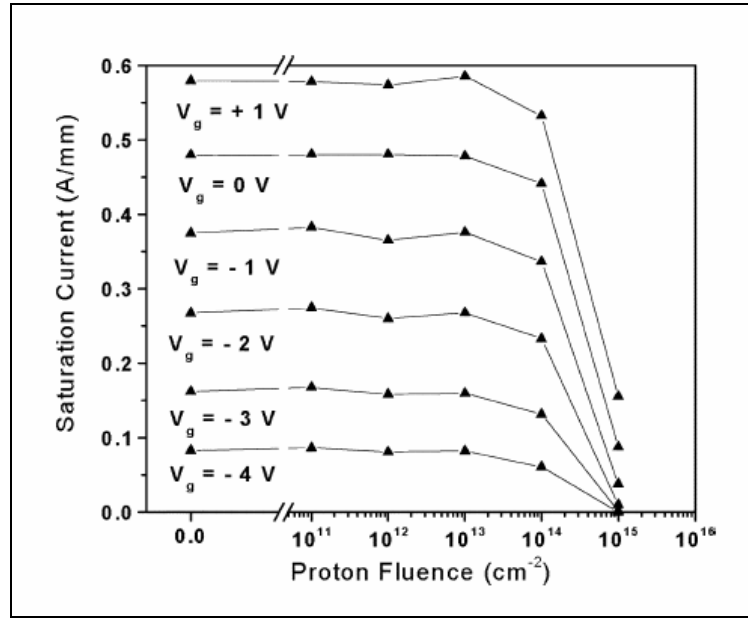


Figure 11. Drain saturation current as a function of proton fluence [36].

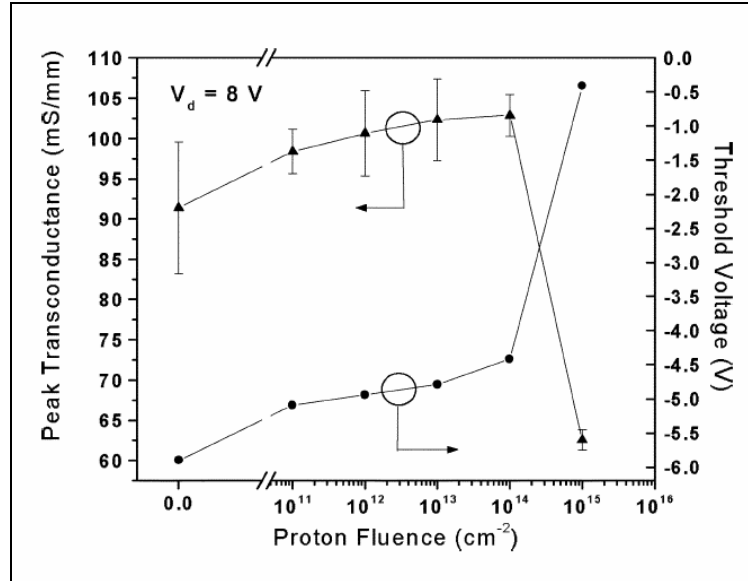


Figure 12. Extracted threshold voltage and peak transconductance as a function of proton fluence [36].

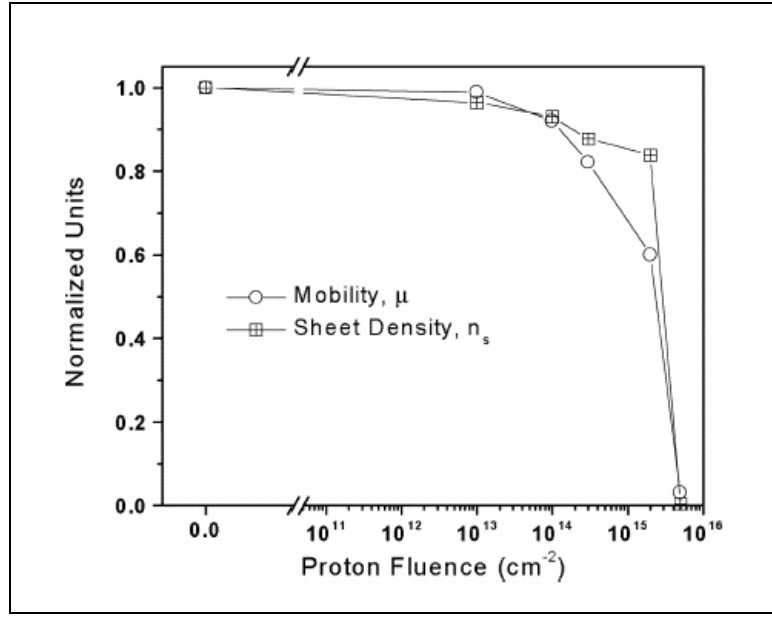


Figure 13. Normalized mobility and 2DEG sheet density, extracted from RT Hall effect measurements. The initial 2DEG mobility and sheet density were $987 \text{ cm}^2 \cdot \text{V}^{-1} \cdot \text{s}^{-1}$ and $1.03 \times 10^{13} \text{ cm}^{-2}$ [36].

The results obtained by White *et al.* are largely confirmed and reproduced by others. Gaudreau *et al.* investigated the effects of 2 MeV proton irradiation at RT on AlGaN/GaN MODFETs. Devices were irradiated in the same fluence range as that by White *et al.*. The irradiation was shown to reduce the carrier density by half and the mobility by three OOM [37]. The researchers concluded that changes in mobility are more dependent on radiation than sheet charge density. Therefore, systems that derive a preponderance of its performance from mobility are likely to function at a constant level of irradiation until critical fluence. Additional fluence past the critical fluence is likely to cause abrupt catastrophic device failure [37].

Hu *et al.* report on the response of AlGaN/GaN MODFETs for a range of proton energies from 1.8 MeV to 105 MeV [7],[23]. At fluences up to $10^{13} \text{ p}^+ \cdot \text{cm}^{-2}$ for 15-, 40-, and 115-MeV protons, the authors report minimal radiation-induced damage

that quickly anneals out at RT [23]. However, at fluences as low as 10^{12} p⁺·cm⁻² of 1.8 MeV protons, a 10.6% decrease in drain saturation current and 6.1% decrease in the maximum transconductance were observed [23]. Both Figure 14 and Figure 15 illustrate the effects of 1.8 MeV protons. The authors of this study do not attempt to hypothesize the damage or annealing mechanism. Instead, they merely report the experimental results and assert that modeling shows that a 1.8 MeV proton is more damaging than a higher energy proton. I assert that you do not need modeling to make that statement. It is clear that high energy protons will have a very low interaction probability in the 3.54 μ m thick sensitive area of the reported device.

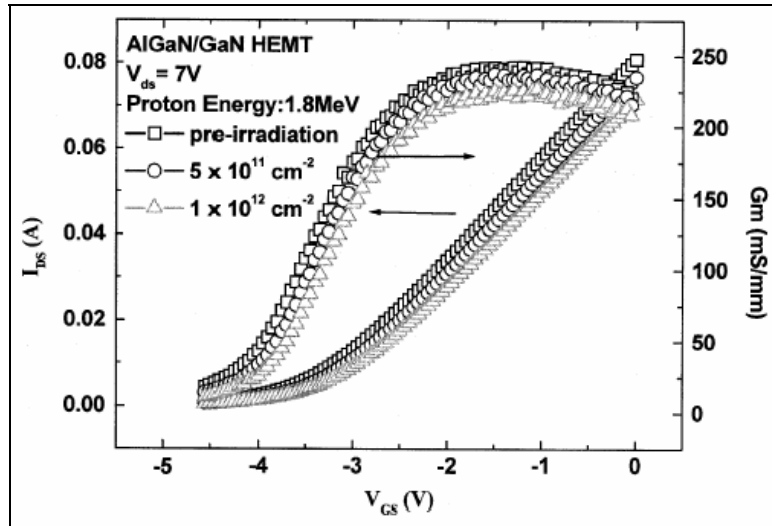


Figure 14. Transfer characteristics for AlGaN/GaN MODFETs before and after 1.8-MeV proton irradiation at different fluences [23].

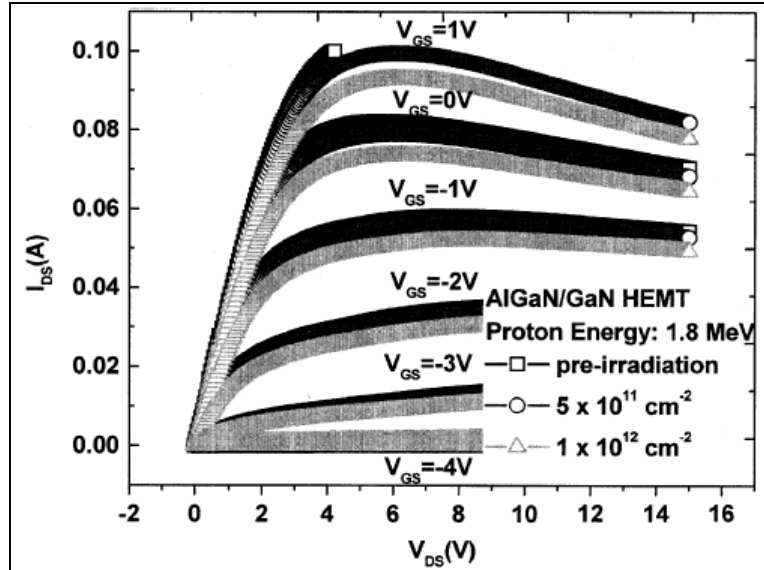


Figure 15. I_{ds} – V_{ds} characteristics for AlGaN/GaN MODFETs before and after 1.8-MeV proton irradiation at different fluences at RT [23].

In a subsequent study also conducted by Hu *et al.*, the researchers report the effects of 1.8 MeV protons on an AlGaN/AlN/GaN MODFETs [7]. In this study, the authors proclaim that GaN-based devices are extremely radiation tolerant and that the primary damage mechanism is caused by displacement damage [7]. Hu *et al.* report no significant degradation at fluences of $10^{13} \text{ p}^+ \cdot \text{cm}^{-2}$ for 15-, 40-, and 105-MeV protons. In addition, no degradation was observed for 1.8-MeV protons at fluences below $10^{13} \text{ p}^+ \cdot \text{cm}^{-2}$ [7]. The authors observed a positive threshold voltage shift and a corresponding decrease of drain current at fluences above $10^{13} \text{ p}^+ \cdot \text{cm}^{-2}$ [7]. At fluences of $10^{15} \text{ p}^+ \cdot \text{cm}^{-2}$ and $3 \times 10^{15} \text{ p}^+ \cdot \text{cm}^{-2}$ the drain saturation current drops to 50% and 80% of its original pre-irradiation value respectively [7]. The maximum g_m is nearly constant at all proton-energies up to a fluence of about $10^{14} \text{ p}^+ \cdot \text{cm}^{-2}$ [7]. At $3 \times 10^{15} \text{ p}^+ \cdot \text{cm}^{-2}$ 1.8-MeV protons, the maximum g_m is degraded by 55% [7]. Hu *et al.* also report a positive V_{th} shift of nearly 50% [7]. At a fluence of between $10^{15} \text{ p}^+ \cdot \text{cm}^{-2}$ and $3 \times 10^{15} \text{ p}^+ \cdot \text{cm}^{-2}$, an

approximately 30% decrease in the carrier mobility and carrier sheet density was observed [7]. The authors hypothesize that displacement damage is responsible for the decrease in saturation drain current, decreased g_m , and positive V_{th} shift. The degradation is likely due to a decrease in both carrier concentration and mobility within the 2DEG resulting from carrier scattering and carrier removal [7]. Hu *et al.* suggest that defect centers created within the 2DEG cause the decrease in sheet carrier concentration.

Research Justification

Clearly there is a need for GaN-based technology for niche applications. However, it will not be long before the beneficial aspects of GaN are desired elsewhere. The military is keenly interested in GaN-based devices for both satellite protection measures and advanced integrated sensor/computing systems. In addition to the military's interest, GaN is viewed as a commercially important material. Applications of GaN can already be found in both the high brightness LED market and high-power microwave frequency market for cellular communications. As the applications of GaN-based devices expand, the need for understanding their radiation response increases. The best example of this can be seen in the desire to use GaN-based devices on space-borne platforms, where devices are exposed to an unrelenting barrage of proton, neutron, electron, and photon radiations. The current state of technology is uncertain. Although the radiation hardness of GaN is nearly universally accepted, contradictory experimental behaviors are observed. A neutron irradiation study on AlGaN/GaN MODFETs is the next step in a logical progression of radiation testing and would greatly contribute to the general knowledge of AlGaN/GaN MODFETs.

III. Theory

This chapter provides a brief background in the theory of AlGaN/GaN heterojunctions and radiation interactions with matter. Although the thesis is a stand-alone document, the reader is expected to have a thorough understanding of semiconductor device physics before attempting to delve into this subject matter. Only key areas of interest will be investigated.

MODFET Charge-Control Model

An ideal heterojunction consists of a semiconductor crystal in which changes between participating atoms are abrupt. Poorly controlled interfaces such as Silicon Dioxide/Silicon are not atomically abrupt and have many dislocations in the crystalline structure. Such disparities can leave dangling bonds and cause dislocation defects, which trap charge carriers and degrade system performance.

Until recently, accepted wisdom was that lattice constants needed to match in order to minimize interface states. However, advancements in material processes have shattered that long held belief and created a new class of quantum controlled ‘strained-layer’ heterojunctions. The essential idea is that if one of the semiconductors forming a heterojunction is sufficiently thin, the lattice mismatch is accommodated by a deformation (strain) in the thin layer. Within the strained-layer interface, a high mobility, high carrier concentration, two-dimensional electron gas forms. The representation of a conventional high electron mobility transistor (HEMT, synonymous with MODFET) structure shown in Figure 16 illustrates the basic arrangement of 2DEG-controlled devices. Variations to the basic structure may include the addition of surface passivation

layers (to decrease surface states), alternating layers of doped and unintentionally doped (UID) AlGaN and GaN, nucleation layers between the GaN and substrate, and other modifications. With respect to an AlGaN/GaN material system, AlGaN is deposited in a thin layer typically ten to forty nm thick on bulk GaN.

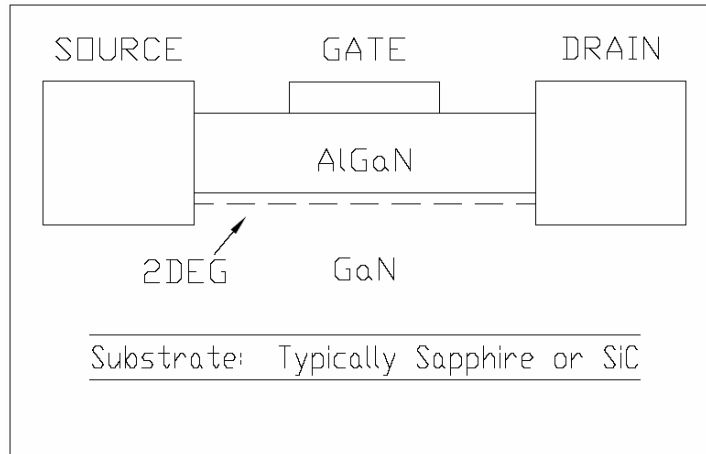


Figure 16. Basic MODFET structure with the x-axis in/out of the page and z-axis top to bottom (not to scale).

Although the 2DEG formation mechanism is thought to be well known, the control parameters are still undetermined and hence heterostructure behavior not fully understood. There are however, prevailing models that capture many of the observed behaviors of 2DEG-controlled systems. The material offered within this section will be presented in the following order: 2DEG band structure and formation, derivation of the 2DEG electron and sheet charge density, and correlation of I-V transfer characteristics to the 2DEG formation mechanisms.

The band structure of complex group-III nitride heterostructures is easiest understood by examining band theory. Figure 17 shows the AlGaN/GaN interface and subsequent quantum well formation at the interface. Trapped within a sheet-like

quasi-triangular quantum well, the nearly two-dimensional gas has a nominal thickness of approximately 2.5 nm when the sheet concentration is on-the-order of $10^{13} \text{ e}^- \cdot \text{cm}^{-2}$ [37]. In addition to being nearly two-dimensional, the thickness is less than the de Broglie wavelength ($\lambda = h/p$) for an electron within the 2DEG, resulting in 2DEG formation. In solving the Schrödinger equation, the potential is separable into both the perpendicular and parallel components, setting up standing waves in the thickness direction (z), and quantizing the energy [37]. Thus, it becomes possible to collapse the quantum well and turn the device off when an integer number of half-wavelengths no longer fit within the quantum well.

AlGaN and GaN are typically as-grown n-type materials. Consequently, the majority carriers are electrons. However, two-dimensional hole gas (2DHG) devices have been demonstrated, but the reduced mobility (in general) of holes makes them less attractive. 2DHG devices are beyond the scope of this discussion [38].

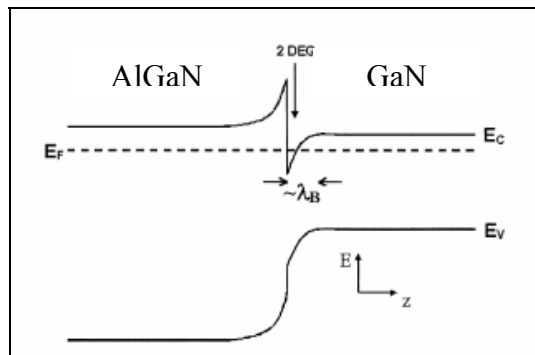


Figure 17. Qualitative description of an AlGaN/GaN interface [37].

From the band structure, it is easy to visualize quantum-well-confined electrons traversing the device with a gas like behavior. However, the band structure alone tells us nothing of quantum well formation. Additionally, one must ask how the electrons

populate the well and what processes affect the flow of charged carriers in the 2DEG? In order to answer these questions, further investigation into the piezoelectric and polarization properties of AlGaN and GaN is necessary.

Semiconductor materials of the group-III nitrides are pyroelectric in nature: meaning they exhibit large nonvanishing spontaneous polarization (SP) (polarization at zero strain) constants. Crystallographic polarities of atomic layers are observed in tetrahedrally oriented wurtzite group-III nitrides [39], [12]. Figure 18 illustrates the crystallographic polarity of the binary compound GaN.

Wurtzite structured binary A-B compounds lack inversion symmetry along the c-direction (parallel to the z-axis). Consequently, the sequence of atomic layers is reversed along the $[0001][000\bar{1}]$ directions. “Because of this non-centrosymmetry and large ionicity associated with the covalent metal nitrogen bond, a large spontaneous polarization oriented along the hexagonal c-axis occurs [39].”

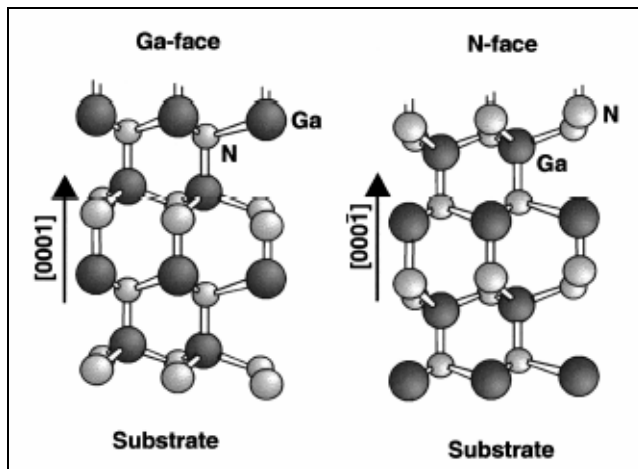


Figure 18. Crystalline structure of wurtzite Ga-face and N-face GaN [39].

Since the lattice constant for GaN is greater than that of AlN, and the AlGaN layer is grown intentionally thin, a tensile strain is generated within the AlGaN layer. The resulting strain induces a piezoelectric polarization (PE) which adds to the net SP. Because the SP and PE constants for AlGaN are larger than GaN, a gradient of net polarization points towards the substrate in 2DEG formation for Ga-faced heterojunctions. The resulting electric field always points in opposition to the net polarization. Figure 19 shows the directions of the spontaneous and piezoelectric polarization for given Ga-face, strained AlGaN/GaN heterostructures.

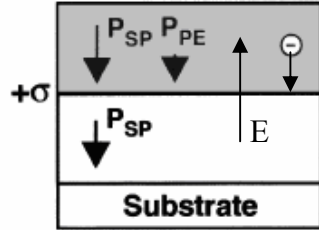


Figure 19. Polarization induced sheet charge density[39].

The tensile strain caused by the growth of $\text{Al}_x\text{Ga}_{1-x}\text{N}$ on GaN results in a net polarization given by [17] in Equation 2.

$$P(x) = P_{SP}(x) + P_{PE}(x) = 0.02x + 0.019x^2 \quad (2)$$

where x is the mole fraction of aluminum in the $\text{Al}_x\text{Ga}_{1-x}\text{N}/\text{GaN}$ material system.

If the polarization induced sheet charge density (σ) is positive, free electrons will migrate and tend to compensate the stationary positive polarization induced charge. Free electrons from the n-type AlGaN layer are motivated to congregate at the AlGaN/GaN interface due to the strong electric field, whereas, free electrons from the n-type GaN are motivated by diffusion processes alone. It is widely believed that ionized donor

impurities within the bulk n-AlGaN are the primary contributor of electrons in the 2DEG. However, electrons from the n-GaN and ohmic metal contacts are also possible contributors to the free electron gas. At extremely high dopant levels, Schottky barriers become more ohmic-like and can also contribute via tunneling mechanisms into the AlGaN. Assuming that the AlGaN/GaN band offset is reasonably high and the interface roughness is low, a 2DEG will form. The polarization induced sheet charge density at the interface is then given by:

$$|\sigma(x)| = \left| P_{PE}(Al_xGa_{1-x}N) + P_{SP}(Al_xGa_{1-x}N) - P_{SP}(GaN) \right| [39] \quad (3)$$

$$|\sigma(x)| = \left| 2 \frac{a(0) - a(x)}{a(x)} \left(e_{31}(x) - e_{33}(x) \frac{C_{13}(x)}{C_{33}(x)} \right) + P_{SP}(x) - P_{SP}(0) \right| [39] \quad (4)$$

where $a(x)$ is the lattice constant, $e_{31}(x)$ and $e_{33}(x)$ are piezoelectric constants, and $C_{13}(x)$ and $C_{33}(x)$ are the elastic constants. Linear interpolation between the physical properties of AlN and GaN yield a set of Aluminum content (Al-content) dependent equations for $Al_xGa_{1-x}N$ listed in Table 2.

Table 2. Al mole fraction dependent parameters for $Al_xGa_{1-x}N/GaN$ MODFETs.

Parameter	Expression	Units	Reference
$\varepsilon(x)$	$(-0.5x + 9.5)8.854x10^{-12}$	$C \cdot m^{-1} \cdot V^{-1}$	[39]
$\phi_m(x)$	$(1.3x + 0.84)$	eV	[39]
$\Delta E_c(x)$	$(1.197x + 0.7x^2)$	eV	[39]
$C_{13}(x)$	$(5x + 103)$	GPa	[40]
$C_{33}(x)$	$(-32x + 405)$	GPa	[40]
$a(x)$	$(-0.077x + 3.189)10^{-10}$	m	[39]
$e_{31}(x)$	$(-0.11x - 0.49)$	GPa	[40]
$e_{33}(x)$	$(0.73x + 0.73)$	GPa	[40]
$P_{SP}(x)$	$(-0.052x - 0.029)$	$C \cdot m^{-2}$	[40]

Thus, for a system with Al-content $x = .27$, the polarization induced sheet charge density is approximately 0.019 C-m^{-2} and the sheet charge (σ_e) is nearly $1.2 \times 10^{13} \text{ cm}^{-2}$ [39].

In order to develop a reliable physics based model for MODFETs, an accurate estimation of the 2DEG density at the interface is essential. A number of charge-control models have been developed and are currently available. Although helpful, many models generally require simplifying assumptions (semi-empirical formulations) that may not accurately represent observed device behavior. Some models assume a linear dependence of 2DEG density with gate bias and tend to underestimate the density near threshold. Other models assume nonlinear dependencies, but resort to non-physical fitting parameters or use computationally rigorous iterative techniques. Perhaps the most commonly used charge-control model involves that of solving Schrödinger's and Poisson's equations both self-consistently and simultaneously. This method also requires excessive computational effort in converging to a solution. The following computationally efficient, closed form, physics based charge-control model is proposed by Rashmi *et al.* [41], [42], [43], [44], [45].

The 2DEG sheet charge density formed at the heterojunction is given as:

$$n_s(x, z) = \frac{\varepsilon(x)}{q \cdot (d_d + d_i + \Delta d)} (V_{gs} - V_c(z) - V_{th}(x)) [41] \quad (5)$$

where q is the electronic charge, $\varepsilon(x)$ is the Al-content dependent dielectric constant, d_d is the AlGaN cap thickness, d_i is the UID AlGaN layer thickness, Δd is the effective 2DEG thickness, V_{gs} is the applied gate-to-source voltage, $V_c(z)$ is the channel potential

at position z , and $V_{th}(x)$ is the Al-content dependent threshold voltage. All parameters are fixed during device fabrication (or possibly changed during irradiation) except that of the applied gate-to-source voltage. Therefore, V_{gs} toggles the 2DEG sheet charge density, which results in the desired transistor action.

The threshold voltage is strongly dependent on the polarization charge density and is related as:

$$V_{th}(x) = \phi_b(x) - \Delta E_c(x) - \frac{qN_d d_d^2}{2\varepsilon(x)} - \frac{\sigma_{pol}(x)}{\varepsilon(x)}(d_d + d_i) \quad (6)$$

where $\phi_b(x)$ is the Al-content dependent SBH and $\Delta E_c(x)$ is the Al-content dependent conduction band discontinuity given in Table 2. The doping density of the AlGaN barrier is N_d , and $\sigma_{pol}(x)$ is related to the strained and unstrained layers as in Equation 7 below.

$$\sigma_{pol}(x) = \sigma_{pseudomorphic}(x) - \sigma_{relaxed}(x) \quad (7)$$

where $\sigma_{pseudomorphic}(x)$ has the same meaning as Equation 3 and represents the polarization of a fully strained system. The polarization in a relaxed system is given by:

$$\sigma_{relaxed}(x) = 2r(x) \frac{a(0) - a(x)}{a(x)} \left(e_{31}(x) - e_{33}(x) \frac{C_{13}(x)}{C_{33}(x)} \right) \quad (8)$$

where $r(x)$ is the Al-content dependent degree of relaxation. The following relaxation relationship is valid for AlGaN thickness ranging from 20-40 nm:

$$r(x) = \begin{cases} 0 & \text{for } 0 \leq x \leq 0.38 \\ 3.5x - 1.33 & \text{for } 0.38 \leq x \leq 0.67 \quad [39] \\ 1 & \text{for } .67 < x \leq 1 \end{cases} \quad (9)$$

Figure 20 is a schematic of the AlGaN/GaN structure used in derivation of the presented charge-control model. Although the device shown has a doped cap (d_d) of n-type AlGaN, the model also accurately represents devices in which the doped cap is removed. Figure 21 illustrates the energy diagram and the physical meaning of the various parameters. In both Figure 20 and Figure 21, m represents the mole fraction of aluminum.

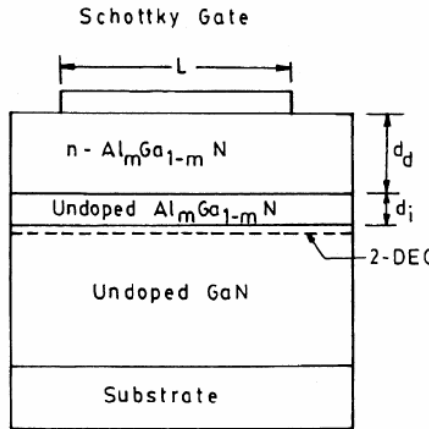


Figure 20. Schematic representation of AlGaN/GaN MODFET design used in derivation of the presented charge-control model [44].

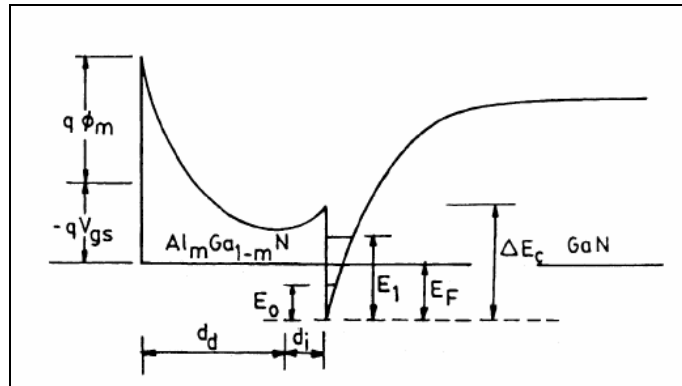


Figure 21. The energy band profile of the modeled AlGaN/GaN MODFET [44].

The drain current in the 2-DEG channel can be obtained from the current density equation as:

$$I_{ds}(x, z) = Wq\mu(z) \left(n_s(x, z) \frac{dV_c(z)}{dz} + \frac{k_B T}{q} \frac{dn_s(x, z)}{dx} \right) \quad (10)$$

where W is the gate width, k_B is the Boltzmann constant, T is temperature, and $\mu(z)$ is the field-dependent electron mobility given in Equation 11.

$$\mu(z) = \frac{\mu_0}{1 + \left(\frac{\mu_0 E_c - v_{sat}}{E_c v_{sat}} \right) \frac{dV_c(z)}{dz}} \quad (11)$$

where μ_0 is the low-field mobility, E_c is the critical electric field, and v_{sat} is the saturation drift velocity. Combining Equations 10 and 11 into Equation 12 yields:

$$I_{ds}(x, z) \left(1 + \left(\frac{\mu_0 E_c - v_{sat}}{E_c v_{sat}} \right) \frac{dV_c(z)}{dz} \right) = \frac{W\mu_0\varepsilon(x)}{(d_d + d_i + \Delta d)} \left(V_{gs} - V_{th}(x) - V_c(z) - \frac{k_B T}{q} \right) \frac{dV_c(z)}{dz} \quad (12)$$

By integrating Equation 12 with boundary conditions 13a/b, the drain-to-source current is obtained in the linear region of the I-V characteristics.

$$V_c(z)|_{z=0} = I_{ds}(x) R_s \quad (13a)$$

$$V_c(z)|_{z=L} = V_{ds} - I_{ds}(x)(R_s + R_d) \quad (13b)$$

$$I_{ds, LN}(x) = \frac{-A_2(x) + \sqrt{A_2(x)^2 - 4A_1(x)A_3(x)}}{2A_1(x)} \quad (14)$$

with

$$A_1(x) = \left(\frac{\mu_0 E_c - v_{sat}}{E_c v_{sat}} \right) (2R_s + R_d) - \left(\frac{W\mu_0\varepsilon(x)}{2(d_d + d_i + \Delta d)} \right) (R_d^2 + 2R_s R_d) \quad (15a)$$

$$\begin{aligned}
A_2(x) = & \left(\frac{W\mu_0\varepsilon(x)}{d_d + d_i + \Delta d} \right) \\
& \left(V_{ds} (R_s + R_d) - \left(V_{gs} - V_{th}(x) - \frac{k_B T}{q} \right) (2R_s + R_d) \right) \\
& - L - V_{ds} \left(\frac{\mu_0 E_c - v_{sat}}{E_c v_{sat}} \right)
\end{aligned} \tag{15b}$$

$$A_3(x) = \left(\frac{W\mu_0\varepsilon(x)}{d_d + d_i + \Delta d} \right) \left(\left(V_{gs} - V_{th}(x) - \frac{k_B T}{q} \right) V_{ds} - \frac{V_{ds}^2}{2} \right) \tag{15c}$$

where R_s and R_d are the parasitic source and drain resistances illustrated in Figure 22.

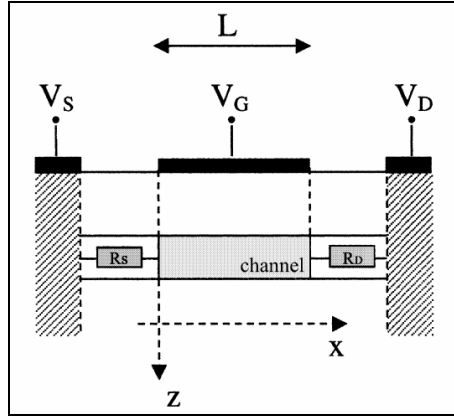


Figure 22. Schematic diagram illustrating the parasitic resistance [12].

By assuming that the carrier mobility, electric field, and channel potential approach μ_0 , E_c , and $V_{dsat}(x)$ respectively at the onset of saturation, the drain saturation current $I_{dsat}(x)$ is obtained.

$$I_{dsat}(x) = \left(\frac{W\varepsilon(x)\mu_0 E_c}{d_d + d_i + \Delta d} \right) \left(\left(V_{gs} - V_{th}(x) - \frac{k_B T}{q} \right) - V_{dsat}(x) \right) \tag{16}$$

where $V_{dsat}(x)$ is the drain saturation voltage obtained when $I_{dsat}(x)$ is equated with $I_{dsat}(x)|_{V_{ds}=V_{dsat}(x)}$ and is given by:

$$V_{dsat}(x) = \frac{-B_2(x) - \sqrt{B_2(x)^2 - 4B_1(x)B_3(x)}}{2B_1(x)} \quad (17)$$

where

$$\begin{aligned} B_1(x) &= \gamma(x) + \left(\frac{W\mu_0\varepsilon(x)}{d_d + d_i + \Delta d} \right) \left(\left(\frac{\mu_0 E_c - v_{sat}}{E_c v_{sat}} \right) - \frac{1}{2} \right) \\ &\quad - \left(\frac{W\mu_0\varepsilon(x)}{d_d + d_i + \Delta d} \right)^2 E_c (R_s + R_d) \end{aligned} \quad (18a)$$

$$\begin{aligned} \gamma(x) &= \left(\frac{W\mu_0\varepsilon(x) E_c}{d_d + d_i + \Delta d} \right)^2 \left(\frac{\mu_0 E_c - v_{sat}}{E_c v_{sat}} \right) (2R_s + R_d) \\ &\quad - \left(\frac{W\mu_0\varepsilon(x)}{d_d + d_i + \Delta d} \right)^3 \frac{E_c^2}{2} (R_d^2 + 2R_s R_d) \end{aligned} \quad (18b)$$

$$\begin{aligned} B_2(x) &= \left(\frac{W\mu_0\varepsilon(x)}{d_d + d_i + \Delta d} \right) \left(\left(\frac{\mu_0 E_c \left(V_{gs} - V_{th}(x) - \frac{k_B T}{q} \right)}{v_{sat}} \right) + E_c L \right) \\ &\quad - 2 \left(V_{gs} - V_{th}(x) - \frac{k_B T}{q} \right) \gamma(x) \\ &\quad + \left(\frac{W\mu_0\varepsilon(x)}{d_d + d_i + \Delta d} \right)^2 E_c \left(V_{gs} - V_{th}(x) - \frac{k_B T}{q} \right) (3R_s + 2R_d) \end{aligned} \quad (18c)$$

$$\begin{aligned} B_3(x) &= \gamma(x) \left(V_{gs} - V_{th}(x) - \frac{k_B T}{q} \right) \\ &\quad - \left(\frac{W\mu_0\varepsilon(x)}{d_d + d_i + \Delta d} \right) \left(V_{gs} - V_{th}(x) - \frac{k_B T}{q} \right) L E_c \\ &\quad - \left(\frac{W\mu_0\varepsilon(x)}{d_d + d_i + \Delta d} \right)^2 \left(V_{gs} - V_{th}(x) - \frac{k_B T}{q} \right)^2 E_c (2R_s + R_d) \end{aligned} \quad (18d)$$

Transconductance is a small-signal parameter that governs the current-driving capability of field effect devices and is particularly important in estimating RF and microwave performance.

“The transconductance is the most important parameter for optimization of FET high-frequency behavior. The major part of the gain mechanism is embodied in the active channel transconductance, which is evaluated as [43]”

$$g_m(x) = \left. \frac{dI_{ds}(x)}{dV_{gs}} \right|_{V_{ds}} \quad (19)$$

Substitution of Equation 16 into Equation 19 yields the transconductance in the saturation region, and is given as:

$$g_{msat}(x) = \left(\frac{W\mu_0\varepsilon(x)E_c}{d_d + d_i + \Delta d} \right) (1 - \alpha(x)) \quad (20)$$

where

$$\begin{aligned} \alpha(x) = & \left(\frac{-1}{2B_1(x)} \right) \left(1 + \frac{B_2(x)}{\sqrt{B_2(x)^2 - 4B_1(x)B_3(x)}} \right) \beta_1(x) \\ & + \frac{1}{\sqrt{B_2(x)^2 - 4B_1(x)B_3(x)}} \beta_2(x) \end{aligned} \quad (21)$$

with

$$\begin{aligned} \beta_1(x) = & \left(\frac{W\mu_0\varepsilon(x)}{d_d + d_i + \Delta d} \right) \left(\frac{\mu_0 E_c}{v_{sat}} \right) - 2\gamma(x) \\ & + \left(\frac{W\mu_0\varepsilon(x)}{d_d + d_i + \Delta d} \right)^2 E_c (3R_s + 2R_d) \end{aligned} \quad (22a)$$

$$\begin{aligned} \beta_2(x) = & 2\gamma(x) \left(V_{gs} - V_{th}(x) - \frac{k_B T}{q} \right) - L E_c \left(\frac{W\mu_0\varepsilon(x)}{d_d + d_i + \Delta d} \right) \\ & - 2E_c \left(V_{gs} - V_{th}(x) - \frac{k_B T}{q} \right) (2R_s + R_d) \left(\frac{W\mu_0\varepsilon(x)}{d_d + d_i + \Delta d} \right)^2 \end{aligned} \quad (22b)$$

Because the 2DEG is ultimately controlled by the Al-content of the AlGaN barrier, it is essential to incorporate both spontaneous and piezoelectric polarization into any charge-control model. The model proposed by Rashmi *et al.* has been rigorously developed and confirms well with experimental data. This current model does not include the effects of electron traps, surface states, and dislocations, all of which act to reduce 2DEG concentration and generally degrade performance. Therefore, any observed radiation effects can only be interpreted within the structure of this and other presented models.

It should be noted that other $\text{Al}_x\text{Ga}_{1-x}\text{N}/\text{GaN}$ field effect transistor models have been proposed and validated against experimental data. Two such models include those proposed by Morkoç *et al.* and Albrecht *et al.*, both of which are more restrictive [12], [46].

Rectifying Contacts and Charged Carrier Transport

High quality, efficient, thermally stable, reliable electrical contacts are crucial to device performance. Electrical contacts are necessary to turn a collection of bulk semiconductor materials into useable controllable devices. Contacts to bulk materials can be either ohmic or rectifying in nature.

Ohmic contacts are typically low resistance metal contacts that have linear or quasi-linear current voltage characteristics, do not inject minority carriers into the active regions of the device, or significantly degrade device behavior in any other manner [47]. “An accumulation-type contact is the preferred ohmic contact because electrons in the metal encounter the least barrier to their flow into or out of the semiconductor [47].”

They are so-called accumulation-type contacts because majority carriers accumulate compared to their density in an intrinsic bulk semiconducting material [47].

Rectifying contacts on the other hand are typically depletion type contacts that present a barrier to the flow of electrons into or out of the semiconductor bulk. Rectifying or Schottky contacts are an important class of m-s junctions. Schottky structures determine the process of charged carrier flow into the semiconductor from the metal and vice versa. In the case of AlGaN/GaN MODFETs, Schottky contact gates are the direct control mechanism of the current flow within the 2DEG as indicated in Equation 5. The three types of m-s contacts are illustrated in Figure 23, where the upper portion shows the m-s system before contact and the bottom portion after contact. The work function of the metal and semiconductor are represented as the product of the electronic charge and potential (ϕ), where χ is the electron affinity, ϕ_B is the SBH, and V_{bi} is the built-in voltage.

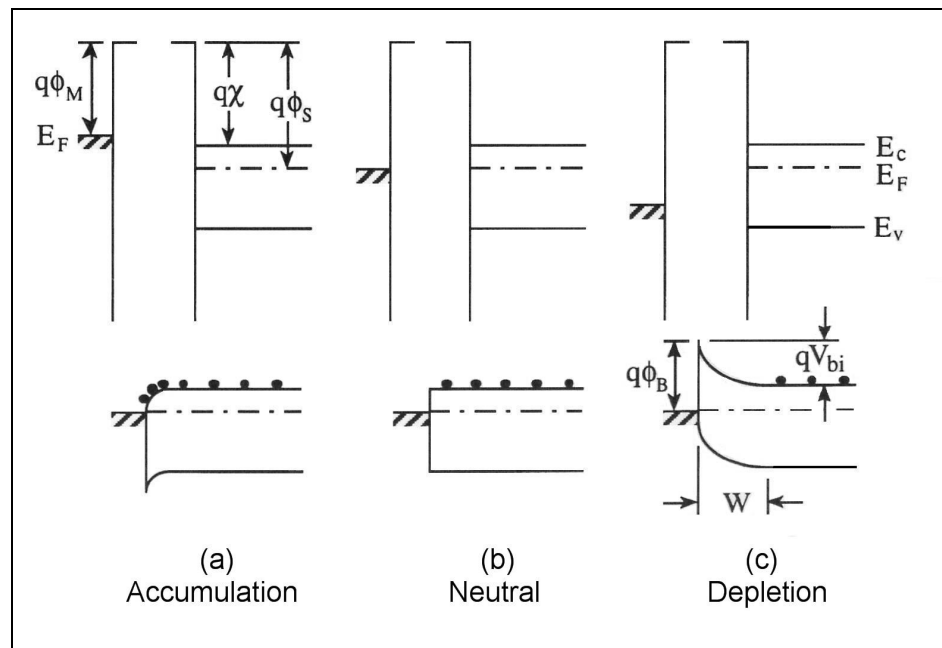


Figure 23. Metal-semiconductor contacts [47].

The nature of the electrical behavior of Schottky structures is still not fully understood. Schottky structures can be measured in a variety of ways, including C-V, I-V, and photoelectric effect. However, the only measurement method that is within the scope of this research project is that of temperature-dependent current-voltage measurements. Although I-V-T measurements present specific difficulties, I-V-T is by far the most commonly used measurement technique to obtain the effective Richardson constant (A^{**}). Therefore, there are numerous methods of extracting the commonly referenced Schottky structure parameters such as SBH, ideality factor (n), and A^{**} .

The process in which electrons are ballistically injected over a potential barrier is known as thermionic emission (TE). First derived in 1942 by Bethe, TE theory is based on three simplifying assumptions that render the shape of the potential barrier immaterial. The result of Bethe's derivation forms the basis of all Schottky contact analysis. Bethe's derived formulation is given in the following equation:

$$I = I_0 \left(\exp \left[\frac{qV}{kT} \right] - 1 \right) \quad (23)$$

where I_0 is the TE saturation current given as:

$$I_0 = A A^{**} T^2 \exp \left[\frac{-q\phi_{b0}}{kT} \right] \quad (24)$$

where A is the effective diode area, A^{**} is the aforementioned Richardson constant, T is the temperature, and ϕ_{b0} is the zero bias SBH (apparent barrier height). The effective Richardson constant is given by:

$$A^{**} = \frac{4\pi q m^* k^2}{h^3} \quad (25)$$

where m^* is the effective mass of an electron within the semiconductor material and h is Plank's constant.

Because practical devices are rarely ideal, an ideality factor is introduced to describe deviation from a pure TE scenario. For devices in which all current transport is due to TE, $n = 1$. All other mechanisms act to increase total current and for any $n > 1$, TE will underestimate current flow. The definition of n is given below as

$$n = \frac{q}{kT} \frac{d \ln I}{dV} \quad (26)$$

The non-ideal TE model then becomes

$$I = A A^{**} T^2 \exp\left[\frac{-q\phi B}{kT}\right] \exp\left[\frac{qV}{nkT}\right] \left(1 - \exp\left[\frac{-qV}{kT}\right]\right) \quad (27)$$

where the diode is biased at a sufficiently high voltage ($V \gg kT$) to ensure thermionic emission. The last exponential in Equation 27 becomes vanishingly small and results in the reduced equation:

$$I = I_0 \left(\exp\left[\frac{qV}{nkT}\right] - 1 \right) \quad (28)$$

Use of the TE model of current flow through the m-s interface can cause significant deviation in the extraction of the SBH, n , and A^{**} because other transport mechanisms are ignored. If accurate parameter extraction is desired, additional current transport processes such as generation-recombination, tunneling, and current leakage through the contact periphery, must all be properly accounted for. Therefore, detailed analysis of the current flow will be taken piecewise to account for various mechanisms.

The current transport in m-s junctions is primarily due to majority carriers. Under forward bias, electrons from the semiconductor conduction band can be transported to the metal by three mechanisms (Figure 24): 1) electrons can traverse the presented barrier by ballistic injection over the barrier (TE), 2) electrons can quantum-mechanically tunnel through the barrier (field emission: FE), or 3) electrons can undergo a thermally assisted tunneling process known as thermionic field emission (TFE). A model of charged carrier transport (based on these three types of barrier actions) that agrees well with experimental data is presented below [48], [49], [4]. Modification of Bethe's original formulation of TE yields the current density due to both TE and tunneling components.

$$J_{s \rightarrow m} = \frac{A^{**}T}{k} \int_0^{\infty} T(\zeta) \exp \left[\frac{-q(V_{b0} + V_n + \zeta - \Delta\phi)}{kT} \right] d\zeta + \frac{A^{**}T}{k} \int_0^{q(V_{b0} - \Delta\phi)} F_s T(\eta) (1 - F_m) d\eta \quad (29)$$

where the parameters are illustrated in the energy band diagram of a m-s Schottky contact in Figure 25. Descriptions of the relevant parameters used throughout this model are explained in Table 3.

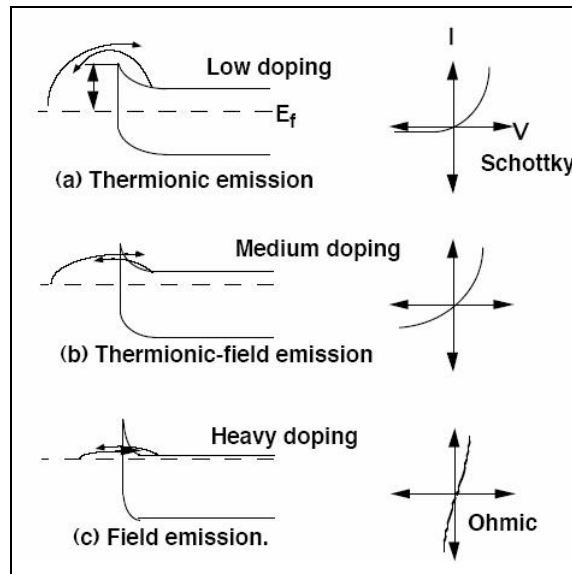


Figure 24. Conduction mechanisms for m-s contacts.

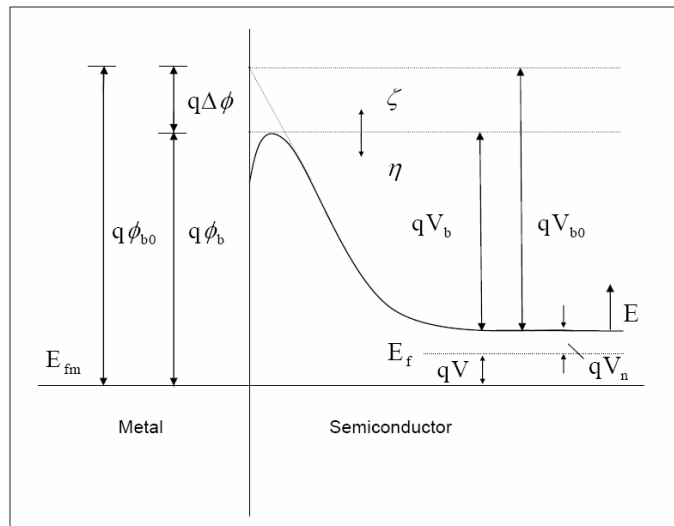


Figure 25. Band diagram of a Schottky barrier contact under forward bias [48].

Table 3. Parameter descriptions for Figure 25.

Symbol	Definition
E_f	Quasi-Fermi level of the semiconductor
E_{fm}	Fermi level of the metal
E_c	Bottom of the semiconductor conduction band
E	Energy of an electron measured from the bottom of the conduction band
ζ	Electron energy above the top of effective barrier
$T(\zeta)$	Quantum transmission coefficient of electrons over the effective barrier
η	Electron energy below the top of the conduction band
$T(\eta)$	Quantum transmission coefficient of electrons below the effective barrier (through the barrier)
V	Applied voltage
$qV_n = E_c - E_f$	Conduction band and quasi-Fermi level difference
$q\phi_{b0}$	SBH of the m-s contact ignoring image force lowering
$q\Delta\phi$	Imaging force lowering of the SBH
$q\phi_b = q\phi_{b0} - q\Delta\phi$	Effective SBH
$qV_b = qV_{b0} - q\Delta\phi$	Effective flat band voltage
F_s, F_m	Semiconductor and Metal Fermi-Dirac distribution functions

From Figure 25, we obtain the following:

$$\eta = qV_b - E \quad (30)$$

and

$$qV_b = q\phi_b - qV_n - qV \quad (31)$$

Rewriting Equation 29 results in the current density in the forward bias regime.

$$\begin{aligned} J_{s \rightarrow m} &= \frac{A^{**}T}{k} \int_0^{\infty} T(\zeta) \exp\left[\frac{-q(V_b + V_n)}{kT}\right] \exp\left[\frac{-\zeta}{kT}\right] d\zeta \\ &+ \frac{A^{**}T}{k} \int_0^{qV_b} F_s T(\eta) (1 - F_m) d\eta = A + B \end{aligned} \quad (32)$$

Assuming that $T(\zeta) = 1$, the first term of Equation 32 becomes the case of pure thermionic emission.

$$A = A^{**}T^2 \exp\left[\frac{-q\phi_b}{kT}\right] \exp\left[\frac{-qV}{kT}\right] \quad (33)$$

The second term of Equation 32 is for the case of direct tunneling through the base of a triangular barrier. Direct tunneling is generally omitted. Instead, other currents such as defect-assisted tunneling and others of an ohmic nature are lumped into a single current leakage component. This method is used because the total current is the sum of the direct current from the metal to the semiconductor and vice versa and implicitly implies that resistance is low [49]. Low resistance cannot be assumed and therefore must be considered as an additional mechanism adding to total current through a contact when assuming pure TE.

The current due to quantum-mechanical tunneling for a moderately to heavily doped semiconductor or for operation at low temperatures, except very low biases, can be written as [50]:

$$I_{TFE} = I_t \left(\exp \left[\frac{qV}{E_0} \right] - 1 \right) \quad (34)$$

where I_t is the saturation value of the current I_{TFE}

$$I_t = \frac{A^{**} T \left(\pi q E_{00} (\phi_{b0} - V - \eta) \right)}{k \cosh \frac{E_{00}}{kT}} \exp \left[-\frac{q\eta}{kT} - \frac{q(\phi_{b0} - \eta)}{E_0} \right], \quad (35)$$

and E_0 is a barrier transparency dependent parameter. The image-charge lowering can be included by replacing ϕ_{b0} with ϕ_b . In the derivation provided by Padovani and Stratton, E_0 and E_{00} have the following meanings [50]:

$$E_0 = E_{00} \coth \left(\frac{E_{00}}{kT} \right) \quad (36)$$

$$E_{00} = \frac{q\hbar}{2} \sqrt{\frac{N_d}{m^* \varepsilon_s}} \quad (37)$$

E_{00} is the characteristic direct tunneling energy and is generally used to determine the importance of TE current. Thermionic emission is typically dominant when $E_{00} \ll kT$, FE becomes important when $E_{00} \gg kT$, and TFE is important when $E_{00} \gg kT$ [51]. Here, it is assumed that all of the donors are ionized and the effective mass is that of the conduction band for n-type semiconductors. Additionally, if the doping is moderately high, η can be neglected [49].

Another mechanism, which causes diode current to deviate from ideal, is that of generation-recombination (GR). Generation-recombination occurs when minority carriers are injected across a junction. At zero-bias, the depletion region of a Schottky contact is in thermal equilibrium. That is, the generation rate of e-h pairs is balanced by the rate of recombination. In the presence of an applied bias, the equilibrium state is perturbed and the net generation or recombination rate depends upon the polarity and magnitude of applied bias. In a forward bias condition (n-type material), electrons from the neutral bulk semiconductor and holes from the Schottky contact are injected into the depletion region. The excess e-h pairs recombine in the depletion region and give rise to a forward bias recombination current. If on the other hand, the Schottky contact is reverse biased, e-h pairs in excess of thermal equilibrium are generated in the depletion region. A reverse current arises when the excess e-h pairs are swept out of the depletion region by the electric field.

Similar to that of a p-n junction, the diode current due to GR can be given as [49],[52]:

$$I_{gen-recomb} = I_{gr} \left(\exp \left[\frac{qV}{2kT} \right] - 1 \right) \quad (38)$$

where

$$I_{gr} = \frac{qn_i w}{2\tau} \quad (39)$$

and w is the thickness of the semiconductor depletion region, n_i is the intrinsic electron concentration, and τ is the electron effective lifetime [52].

Regarding the effects of series and parallel resistances, both mechanisms act to increase the ideality factor when assuming pure TE. When assuming pure TE it is proper to extract n using the slope of the linear region in a semilogarithmic I-V plot. The slope of the linear region is given as:

$$m = \frac{q}{nkT} \quad (40)$$

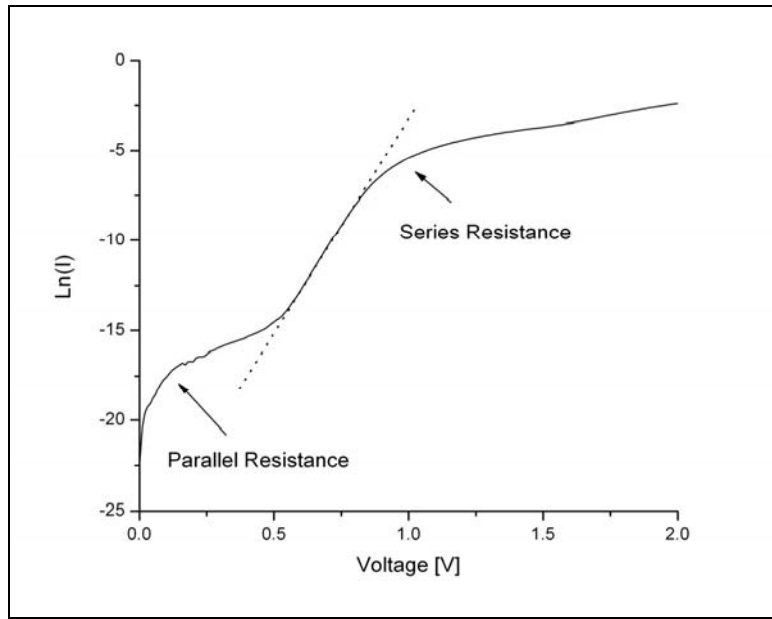


Figure 26. Effects of resistance on Schottky diode parameter extraction.

However, as you can see in Figure 26, the upper limit of the interval is effected by series resistance while various other mechanisms push the lower interval limit up, thus reducing the linear region. From this method, the saturation current for TE can be obtained from the y-intercept at $\ln(I_0)$. Series resistance will tend to decrease the slope of the curve and result in an artificially high y-intercept for the linear fit, and consequently a lower apparent SBH. Similarly, the ideality factor will increase and no physical interpretation in calculating the SBH from Equation 28 is justified [53]. Any

case in which mechanisms other than TE are active, Equation 28 will overestimate the saturation value and importance of TE.

Schottky contacts formed on AlGaN and GaN experience currents that are many OOM greater than predicted by the TE model alone. Large anomalous currents adversely affect device performance and are a subject of intense investigation. Many believe that a high density of unintentionally introduced defect donors is present near the AlGaN surface [54], [55].

“With regard to the origin of unintentional surface donors, a recent theoretical calculation has predicted that the nitrogen vacancy V_N and the oxygen in the nitrogen site O_N behave as donor states near the conduction band [54].”

Because the presented model does not assume pure TE, the excess current is well accounted for in the forward bias regime and this model is sufficient for analysis within the scope of this research project. Figure 27 is the equivalent circuit used to create a model that includes contributions from TE, TFE, FE, GR, resistances, and other miscellaneous tunneling effects. In the proposed model shown as Equation 41, I_{te} , I_{gr} , and I_t are the TE, GR, and tunneling saturation currents respectively, and all other symbols have their usual meanings.

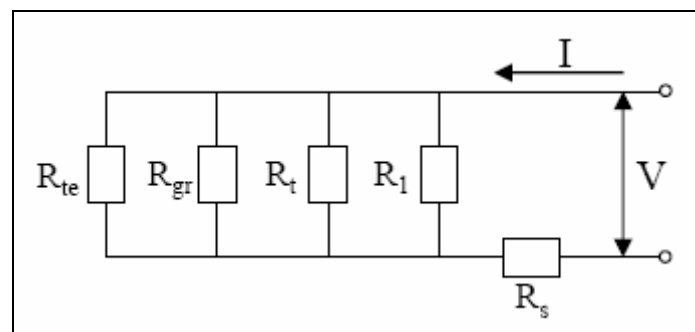


Figure 27. Proposed dc equivalent circuit of a Schottky structure [52].

$$\begin{aligned}
I_{TOTAL} = & I_{te} \left(\exp \left[\frac{q(V - IR_s)}{kT} \right] - 1 \right) \\
& + I_{gr} \left(\exp \left[\frac{q(V - IR_s)}{2kT} \right] - 1 \right) \\
& + I_t \left(\exp \left[\frac{q(V - IR_s)}{E_0} \right] - 1 \right) \\
& + \frac{V - IR_s}{R_1}
\end{aligned} \tag{41}$$

where $V \rightarrow (V - IR_s)$, is the voltage drop across the barrier region. The leakage current,

$I_L = \frac{V - IR_s}{R_1}$, is another parallel component of the total current. It is caused by surface leakage and can usually be significantly reduced by various designs and fabrication techniques. In practice, it is the component which appears to by-pass the m-s interface altogether (defect-assisted tunneling) and is often thought of as a large leakage resistor, R_1 , in parallel to it.

By choosing the correct saturation currents, resistances, and tunneling parameter, a fit to experimental data can be achieved in a wide temperature and applied bias range. A robust numerical analysis routine is necessary to fit the six unknown parameters to experimental data. An outline of a fitting routine and comparison to the traditional diode extraction method is available in Appendix B

IV. Experimental Procedures

Device Fabrication and Packaging

The transistor structures used throughout this study were manufactured by AFRL/SNDD at Wright-Patterson Air Force Base, Ohio on wafers grown by Cree Inc^c. The wafer consisted of a 2 μm thickness of UID GaN grown on a 413 μm 4H-Silicon Carbide (4H-SiC) substrate, followed by approximately 25 nm of 27% mole fraction Aluminum, AlGaN. The wafer was grown by metal-organic vapor-phase epitaxy (MOVPE) and mesa isolated by reactive ion etching. Ohmic (Ti/Al/Ni/Au; 35/230/50/20 nm) and Schottky (Ni/Au; 20/280 nm) contacts were patterned using photolithography to form MODFETs of varying gate dimensions and miscellaneous test structures (C-V ring, Van der Pauw, transfer length, to name a few). Figure 28 shows a post-processed wafer with individual reticles visible. An expanded view of each reticle is shown as Figure 29. Finally, each diced reticle is packaged (Figure 30). The open-faced package allows electrons to penetrate the device during electron-irradiation testing. A more robust packaging system is necessary for future neutron-irradiation studies.

^c Prior to shipping the wafer, Cree Inc. determined the room temperature carrier concentration and mobility to be $1.3 \times 10^{13} \text{ cm}^{-2}$ and $1,300 \text{ cm}^2 \cdot \text{V}^{-1} \cdot \text{s}^{-1}$, respectively [29].

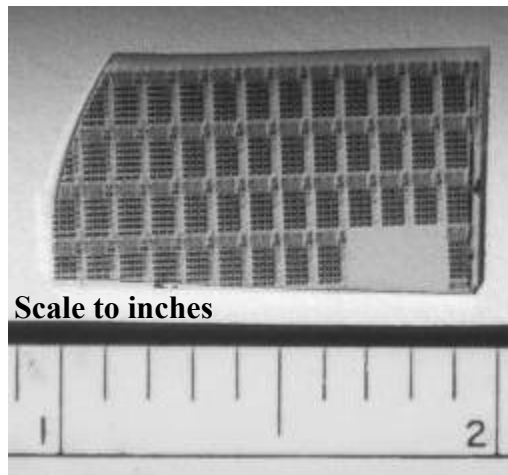


Figure 28. AlGaN/GaN/4H-SiC Wafer segment.

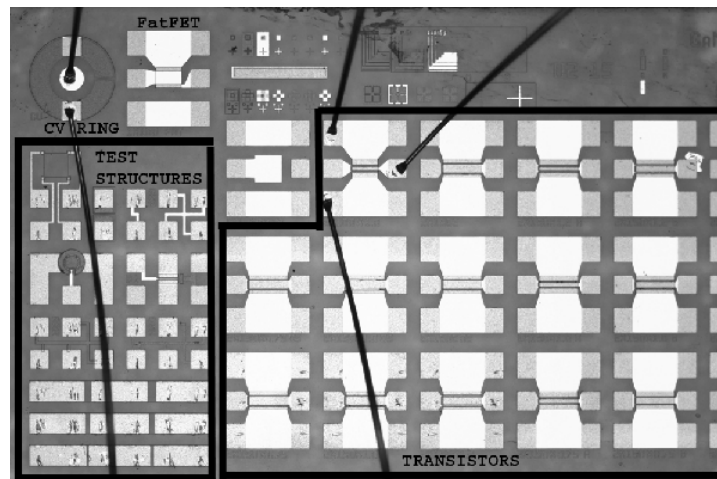


Figure 29. Reticle containing MODFET and test structures [29].

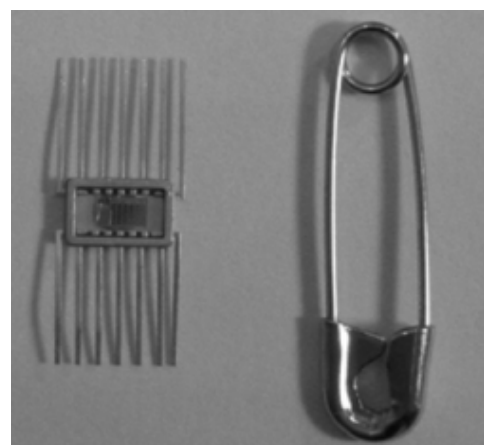


Figure 30. Packaged reticle [29].

Although each reticle contains myriad of useable devices, the only device investigated in this study is that of the FATFET. The FATFET is simply a large single-gate MODFET that is well suited for irradiation testing. The FATFET has a nominal gate width of 50 μm (MODFET gate size is 1.2 μm), small width-to-length ratio, and has greater than 20 times the gate surface area of the double-gated MODFETs located on the reticle. The large mesa area of a FATFET is ideal for observing radiation-induced changes in the 2DEG and eliminating current detection limitations of Schottky measurements. A 20x magnification of the FATFET in use is shown in Figure 31.

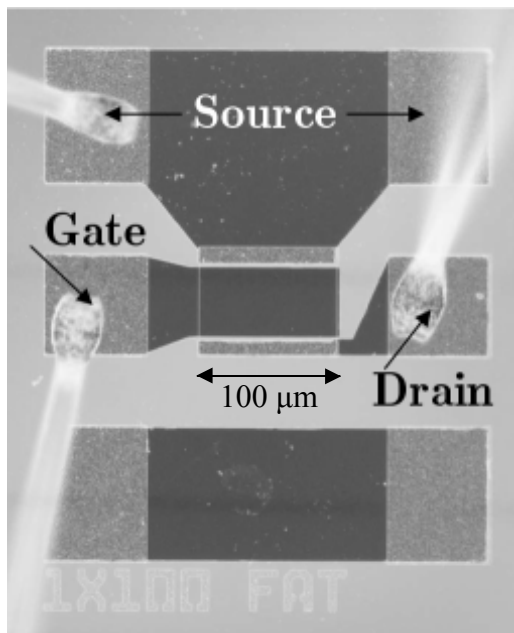


Figure 31. Wired FATFET with appropriate contacts shown.

Neutron-Specific Experimental Considerations

Unlike other radiation sources, the considerations necessary to conduct neutron experiments are unique. The issue of utmost concern with neutron irradiation is activation. Devices, cables, sample holders, etc. with large activation cross sections (e.g. copper, gold, nickel) may become radioactive upon neutron bombardment. In addition to issues of safety, activated devices may hinder the ability to run desired tests and may require a considerable “cool off” period. Therefore, in order to reduce activation, samples are cadmium (Cd) shielded. As seen in Figure 32, Cd has nearly a 4 decade decrease in absorption cross section over one decade of increasing energy past the cutoff of 0.2 eV [56],[57]. Ignoring resonance absorption, neutrons of energy greater than about 1.5 eV pass through Cd with little attenuation.

Although activation can be reduced with proper choices of shielding, fission gamma rays are a significant source of additional accumulated dose and are difficult to avoid. Gamma loading during neutron irradiation can be reduced with shielding by lead and other high Z materials (although it also reduces the neutron fluence). Although the scope of this research limits detailed analysis of accumulated gamma dose, at a maximum NIEL dose of 392 krad (Si), the gamma dose is expected to be significantly less than that the gamma doses of 600 and 21 Mrad (Si) reported by Luo *et al.* and Mishra *et al.*, respectively. No further discussion is given to this matter.

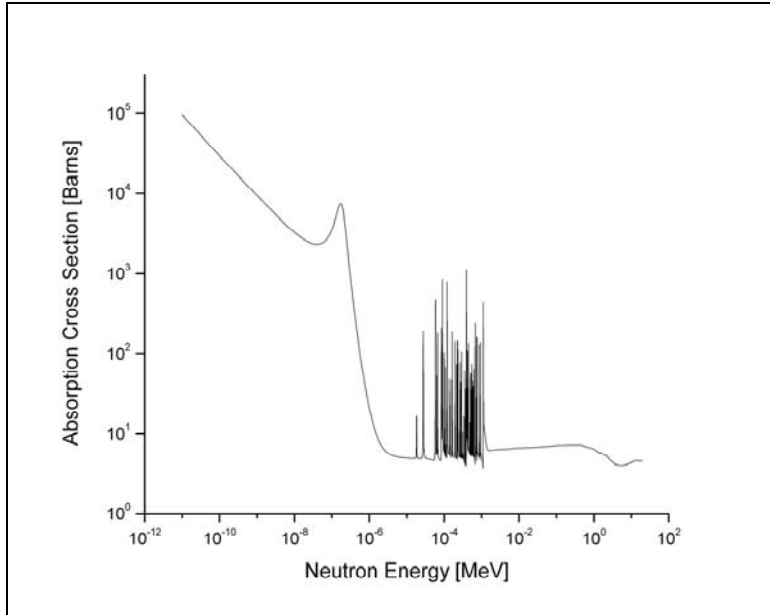


Figure 32. Absorption cross section of Cadmium.

Pre-irradiation Characterization

Prior to conducting irradiation experiments, newly packaged devices were characterized and all experimental equipment exercised to ensure proper working order. The equipment necessary for this phase of testing included an Omega temperature meter configured for a type-K thermocouple, two Keithley 237 Source Measurement Units (SMU), a National Instruments General Purpose Interface Bus (GPIB), and laptop computer for computer control and data acquisition. Figure 33 shows the equipment used for electronic measurements throughout this research. Although initial testing included only I-V characteristics, expansion of testing capabilities eventually necessitated a measurement-type switch box (discussion to follow) shown as Figure 34. A schematic diagram of the setup in its final form is shown as Figure 35. Although not specifically

stated, every measurement was conducted in darkness and consisted of a minimum of four measurements for *in situ* irradiations or eight measurements for PART irradiations.

The computer control and data acquisition program written in Visual Basic is available in electronic form upon request.



Figure 33. Experimental setup showing electronic measurement equipment.



Figure 34. Measurement-type control switch.

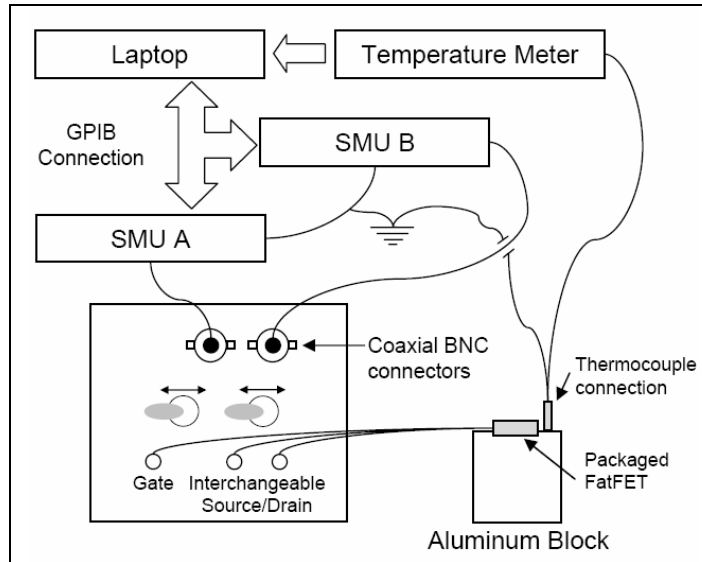


Figure 35. Schematic representation of experimental equipment setup.

Characterization of FATFETs can generally be broken down into four distinct categories: single temperature I-V characteristics, single-temperature transfer characteristics, single-temperature Schottky characteristics, and temperature-dependent Schottky characteristics.

The physical device configuration for both the I-V and transfer measurements is identical. In each case, one SMU applies a gate-to-source voltage bias (measures gate-to-source current) and the other SMU applies a drain-to-source voltage bias (measures drain-to-source current). In both measurement types, the SMUs are referenced to a common source/ground. Typically, in an I-V measurement the applied gate bias is stepped in increments from -4.0 to 0.0 V as the drain voltage is swept from 0.0 to 15.0 V at each gate voltage. In a transfer measurement however, the drain-to-source voltage is held constant in the saturation region ($\approx +6.0$ V) as the gate is swept from -4.0 to +3.0 V.

Measurements of the Schottky contact require a different physical configuration altogether. In order to measure the Schottky diode behavior, the source and drain are tied together (ground) as the gate voltage is swept from -4 to +3 V. Only one SMU is required for Schottky measurements. However, in order to accomplish quick changes between I-V and Schottky measurements, a measurement-type switch box is utilized. Effectively, in the I-V configuration, only the source is used as the common ground. However, in the Schottky configuration, both the drain and source are referenced as common grounds. The SMU tied to both the source and drain is placed in standby mode. Bench top testing demonstrated that the affect of using such a switch box is negligible.

The final measurement is that of the temperature-dependent Schottky characteristics. This measurement differs very little from the single temperature measurement. Since no active temperature control systems are employed, the temperature-dependent Schottky characteristics are simply a continuous loop of single measurements with an accompanying temperature reading during an unaided liquid nitrogen (LiN) burn off. Sample mounting was achieved through careful placement of the individual devices on the cold finger using thermally conductive grease. The device was secured to the block by placing unused package leads under a washer and nut. Wire contacts were isolated to avoid shorting and the block slowly lowered into a LiN bath. Typical burn off cycles last between 8-12 hours. Due to the increased humidity, condensation formed on the device during warm up. To prevent this from occurring, the precharacterization temperature ramps conducted at Wright-Patterson Air Force Base were made under dry nitrogen ambients.

The resultant data is analyzed with a data-conditioning program written in Fortran. The program sorts and averages the data appropriately, outputs the temperature profile, and creates both Mathematica and Excel friendly input files. The program is available in electronic form upon request.

In addition to the electronic equipment required for measurements, a plethora of Dewar designs accompanied this research. Figure 36 and Figure 37 show a wooden cradle designed to fit within the 7" section (outer section) of the BP. A borosilicate evacuated-glass Dewar surrounded by cadmium sheeting is supported by the cradle. With the Dewar, an Aluminum cylinder approx 1" diameter by 2.5" high acts as a cold finger. As a large thermal mass, the block is ideal for mounting both the device, thermocouple sensor, and grounding lead. Additionally, when the system is not within the BP, dark conditions are maintained with a Styrofoam lid. Figure 40 shows a Dewar system designed to operate within the 6" BP section.



Figure 36. Dewar shown in wooden cradle designed to fit within the 7" section of the beam port. Inset shows Cadmium shielded thermal block.



Figure 37. Wooden cradle used for both *in situ* beam port measurements and benchtop characterizations at 80 K in darkness.



Figure 38. 6" Dewar system for *in situ* measurements at 80 K within the BP.

Long Term Anneal Study

Upon successful completion and fielding of a robust acquisition program, previously electron irradiated FATFETs were analyzed. Devices A0408 and A0409 were irradiated by J.M. Sattler and placed in storage at RT. Following a nine month anneal, both devices were again characterized at RT and 80 K. The results of this annealing study are available in Appendix C.

Irradiation Experiments

Essentially six distinct reactor runs were utilized to gather enough data to coherently discuss and confirm observed device behavior. Each run was marked with specific difficulties that degraded the overall quantity and quality of data. Each run is discussed in detail below.

All irradiations utilized the OSURR. The OSURR is a 500 kW, natural convection, pool-type reactor. During operation at high loads, two supplementary cooling loops and an auxiliary water supply can be used to force cool the pool. The OSURR is loaded with approximately 3.9 kg of 19.5% enriched uranium silicide. The irradiation facilities used include a 2" diameter PART and BP. Both have 'direct look' to the core (Figure 39). Standard methods of dosimetry are employed for spectrum determination and are discussed in detail in later section within this chapter.

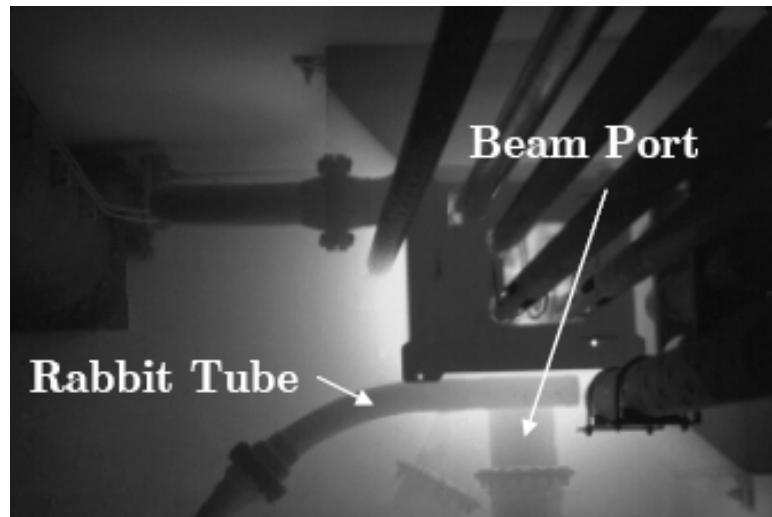


Figure 39. OSURR core and relative placement of irradiation facilities.

Devices irradiated by J.M. Sattler were bracketed between $1 \times 10^{14} \text{ e}^- \cdot \text{cm}^{-2}$ and $1 \times 10^{16} \text{ e}^- \cdot \text{cm}^{-2}$. The relationship of the NIEL rate loss for electrons and neutrons is well characterized for Silicon. Taking advantage of this relationship allows for a ballpark estimate of the starting fluence of neutrons, which should roughly correspond to Sattler's previous work. In Si, 1 MeV neutrons are roughly 100 times more effective at causing displacement damage than an electron of equal energy. That is to say, the number of damage-equivalent 1 MeV electrons per particle is >100 for 1 MeV neutrons. Therefore,

assuming non-ionizing energy loses only, the required neutron fluence is two OOM lower than previously reported electron fluences. Finally, because the relationship for electrons and neutrons in GaN is unknown, the fluence is further reduced by an OOM. Two advantages arise from the method. 1) Direct comparisons of 1 MeV Eq (Si) fluences for GaN and Si-based devices can be made and 2) Doses are easily reported in rad (Si).

The first irradiation experiment conducted on 20DEC04 was designed to scrutinize the proposed radiation test plan. The Dewar apparatus was placed in the BP to characterize the setup and obtain a spectrum of the BP (Figure 40). An initial spectrum is critical to ensure that the fluence is a) not too high as to make irradiation times exceedingly short, and b) not too low as to bound the upper limit. The essential issue with this setup is that the gamma-shutter of the beam port must remain open when using the 7" section. This essentially turns the BP into a neutron-howitzer. In order to reduce the potential radiation hazard, a polyurethane (poly) plug capped with Cd was placed within the 6" section, ahead of my apparatus. The first layer of Cd effectively absorbs already thermalized neutrons, allowing only epi-Cd neutrons to traverse the poly plug. The poly plug has a high hydrogen content, which effectively thermalizes neutrons, which in turn get absorbed by the second layer of Cd. Additionally, the Dewar is Cd covered and has a high boron concentration. Finally, the BP was heavily shielded with lead and concrete bricks interlaced with Cd sheets (Figure 41). The reactor (Rx) was run at 100 kW (10% power) for 30 minutes. Neutron and gamma levels appeared to be in a safe range.



Figure 40. Insertion of Dewar apparatus into beam port for *in situ* measurements (LEFT) and polyurethane plug to moderate streaming neutrons (RIGHT).



Figure 41. Shielding of the beam port with lead bricks (LEFT) and concrete blocks (RIGHT) to attenuate neutron-induced gamma radiation.

The second experiment was conducted from 04-05JAN05. On 04JAN05, device A12 was prepared for an overnight characterization run. The device was mounted to the thermal block, cooled to 80 K, and successfully characterized. The device functioned throughout the evening and completed the 14 hour temperature ramp from 80 K to 295 K. On 05JAN05, A12 was cooled down again and prepared for *in situ* irradiation measurements. However, final testing indicated an anomalously large gate leakage current indicative of static-discharge damage. The device became gate leakage dominated and rendered unusable. In its place, device A25 was prepared for *in situ* irradiation

measurements. A25 has no temperature-dependent precharacterization Schottky data due to the failure of A12. Only a baseline characterization at 80 K was completed.

Almost as soon as Rx steady-state was achieved at 7.5 kW, a serious neutron hazard was discovered and power was limited to a maximum of 5 kW. The power reduction was necessary to maintain safe neutron radiation levels outside of the Rx and Rx building. The total irradiation time was 148 minutes and a total NIEL dose of only 5.4 rad (Si) was achieved. At 5 kW it would take nearly 15 hours to achieve only 33 rad (Si) total NIEL dose and nearly 16.5 years for 326 krad (Si).

In order to speed the process, an entirely new irradiation plan was devised. Instead of *in situ* measurements at 80 K within the BP, subsequent irradiations would be conducted at ambient temperature within the PART (Figure 42). Since the total flux of the PART is five OOM greater than the BP configuration, nearly 5 decades of fluence are obtainable simply by altering the power level.

The third irradiation experiment consisted of reusing device A25 and was conducted over a two day period from 05-06JAN05. A25 was rebaselined so that a fresh starting point was known. A full suite of I-V, transfer, and Schottky measurements was made at 80 K. In addition, a complete temperature-dependent Schottky measurement was made from 80 K to 292 K. On 06JAN05, NASA had use of the BP and I piggybacked off their power settings to irradiate A12 in the PART.

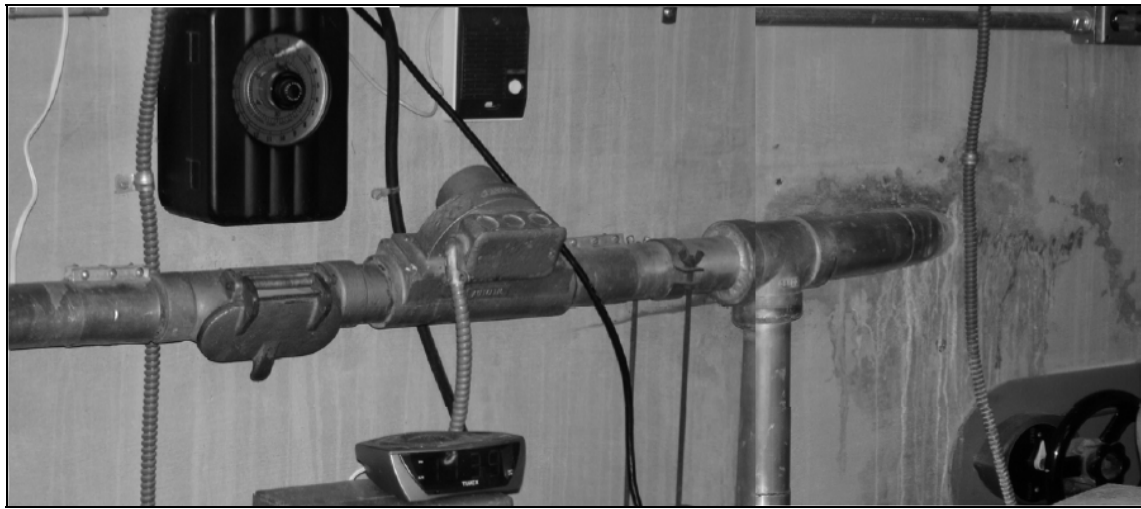


Figure 42. Pneumatically actuated rabbit tube with automatic timer shown.

The device packaging for irradiation in the PART was relatively straightforward. The device was loaded in to a small plastic vial and the leads secured. The vial was wrapped in Cd sheeting, placed within a PART sample carrier, and packed with cotton (Figure 43). Irradiation time was set on the automatic timer with an additional half second added for travel time for short irradiations. Upon completion of the desired fluence, the device was surveyed and then immediately immersed in LiN. Two small holes were cut into the plastic vial on the top and bottom to allow LiN to reach the device. While in the LiN bath, leads were soldered to the exposed wires. After thermal equilibrium was reached a full measurement suite was conducted and the process repeated.

Table 4 shows desired fluence, power setting, and subsequent radiation times for device A25. Following irradiation to 6×10^{12} n-cm⁻², a broken package lead rendered A25 inoperable. The package can be repaired however; any application of heat effectively nullifies irradiation-induced damage. Therefore, A25 was no longer used.

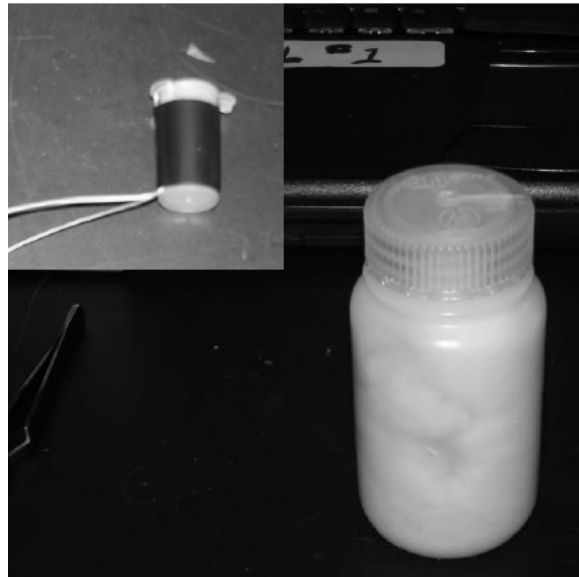


Figure 43. Rabbit Tube sample carrier.

Table 4. A25 PART Irradiation Experiment Summary (06JAN05).

Desired 1MeV Eq Fluence [n-cm ⁻²]	% Rx Power	Successive Irradiation Times [sec]
2x10 ¹¹	0.40	3
4x10 ¹¹	0.40	3
6x10 ¹¹	0.40	3
8x10 ¹¹	0.80	2
10 ¹²	0.80	2
2x10 ¹²	0.80	8
4x10 ¹²	0.80	16
6x10 ¹²	1.60	8
10 ¹²	1.60	16
2x10 ¹²	1.60	41
4x10 ¹²	3.20	41
6x10 ¹²	3.20	41

The fourth irradiation experiment was conducted over three days (10-12JAN05) and utilized two devices, A27 and A29. A27 was irradiated in the PART in a similar manner as A25. A27 also did not have temperature-dependent pre-irradiation Schottky

data due to the failure of another device during precharacterization. During the cool-down phase the devices are extremely sensitive to the different thermal expansion coefficients of the 4H-SiC, epoxy, and package. Apparently, the epoxy bond between the reticle and package is sensitive to thermal gradient induced strains. Upon weakening of the epoxy, catastrophic separation and destruction of the wire bonds ensue.

Table 5. A27 PART Irradiation Experiment Summary (10JAN05).

Desired 1MeV Eq Fluence [n-cm ⁻²]	% Rx Power	Successive Irradiation Times [sec]
10 ¹¹	0.05	13
5x10 ¹¹	0.2	13
10 ¹²	0.2	16
5x10 ¹²	1.6	16
7.5x10 ¹²	1.6	10
10 ¹³	6.4	3
2.5x10 ¹³	6.4	15
5x10 ¹³	6.4	26
7.5x10 ¹³	12.8	13
10 ¹⁴	12.8	13
2.5x10 ¹⁴	25.6	39

Table 5 shows a summary of the radiation plan conducted for device A27. During cool-down after 2.5×10^{14} n-cm⁻² the device catastrophically failed due to the aforementioned mentioned epoxy problem. However, up to this point, no significant radiation induced changes were observed.

Many devices appeared to be failing due to the repeated cool-down phase and the highest fluences were never reached. Therefore, a test device would be irradiated in the PART and measured at 80 K only four times. A29 was precharacterized at 80 K and irradiated according to the plan listed as Table 6.

Table 6. A29 PART Irradiation Experiment Summary (10JAN05).

Desired 1MeV Eq Fluence [n-cm ⁻²]	% Rx Power	Successive Irradiation Times [sec]
10 ¹⁵	25.6	257
2.5x10 ¹⁵	50	197
5x10 ¹⁵	60	274
10 ¹⁶	90	365

At a total accumulated fluence of 10¹⁶ n-cm⁻², the NIEL dose is 326 krad (Si). At 10¹⁶ n-cm⁻² and 90% Rx power, the devices become highly activated and the Cd thermally warm to the touch. Because the maximum Rx power is 90%, any increased doses from this point will require increasingly long irradiation times. From the real-time data obtained during characterization, it was clear that the increased fluence was not having the desired effect. That is, no discernable radiation-induced changes were observed. Therefore, I decided to stop at 10¹⁶ n-cm⁻². Device A29 was remeasured after a 24 and 48 hour RT anneal.

The fifth radiation experiment was conducted on device A30 to confirm the results observed in A29. The experiment spanned 3 days from 10-12JAN05. A full suite of I-V, transfer, and Schottky measurements were made at 80 K. In addition, a complete temperature-dependent Schottky measurement was made from 80 K to 292 K. On 11JAN05 device A30 was irradiated according to the plan listed as Table 7. Upon completion of the test plan, A30 was again fully characterized, including a complete temperature-dependent Schottky measurement was made from 80 K to 292 K. This is the only device in which a pre- and post-irradiation temperature-dependent Schottky measurement could be conducted.

Table 7. A29 PART Irradiation Experiment Summary (10JAN05).

Desired 1MeV Eq Fluence [n-cm ⁻²]	% Rx Power	Successive Irradiation Times [sec]
10^{11}	0.1	7
2×10^{11}	0.1	7
5×10^{11}	0.5	4
10^{12}	0.5	7
10^{13}	10	6
4×10^{15}	90	292
8×10^{15}	90	292
1.2×10^{16}	90	292

The final experiment took place on 13-14JAN05. The experiment utilized a modified Dewar system that fit within the 6" section of the BP for in situ measurements. The updated system contained two devices and a single gold wire for spectrum unfolding scaling. Of the two devices, only one was electrically active and continuously measured. The other device was to be used for a further annealing study after returning to Wright-Patterson AFB. Both devices were packaged similarly to the PART packaging scheme. Each device was stored in a plastic vial and wrapped in Cd. After the apparatus was loaded into the BP the electrically active device was given a final checkout test. Once the Rx became critical I attempted to measure the device again, I noticed about a three OOM increase in gate leakage and the Schottky contact appeared to be resistance dominated. This behavior is indicative of a static-discharge related destruction mechanism and failure was not radiation-induced. Throughout the remainder of the experiment I used this device to observe when it would fail due to increasing neutron dose. At about the 2nd hour, the device reached the measurement system current compliance for drain and gate current. At this point, the Rx was shutdown and the

devices allowed to radioactively “cool”, whilst remaining cryogenically cooled to 80 K. Upon removal from the apparatus, visual inspection revealed that the reticle had fallen from the package. Upon inspection of the secondary device, I observed the same catastrophic failure mechanism. This method is optimal and desired. However, due to unforeseen difficulties the entire data set and devices were rendered useless.

Dosimetry

Determining the amount of energy deposited within an irradiated device is both challenging and essential. Without accurate dose determination, others may have difficulties in reproducing important research. Irreproducible results cast doubt on the validity of an experiment and may undermine high-quality research. Three key factors in reporting accurate dosimetric data are: 1) prior knowledge of the radiation source and consequential measurement limitations, 2) understanding of basic radiation interactions with matter principles, and 3) comprehension of the expected damage mechanism. These issues are particularly misunderstood and misreported because typical device dimensions are OOM smaller than nominal stopping distances. Classically, doses are overestimated. Monte Carlo simulations are an effective means of determining an actual deposited dose. Although simulations are beyond the scope of this research, well-known dose relationships for Silicon are exploited for comparative purposes.

The OSURR neutron energy spectrum is determined by foil spectroscopy and unfolding techniques. American Society for Testing and Materials (ASTM) approved methodologies are used for spectrum analysis. Gold, Copper, and Cobalt wires (bare and Cd covered) were irradiated for 30 minutes at 100 kW in the Dewar system shown

(Figure 36) in the beam port. From the six samples, a spectrum can be unfolded using the SAND-II program (see Figure 44). Limited by the error in gamma-spectroscopy and subsequent unfolding, the reported spectrum has error of greater than 25%.

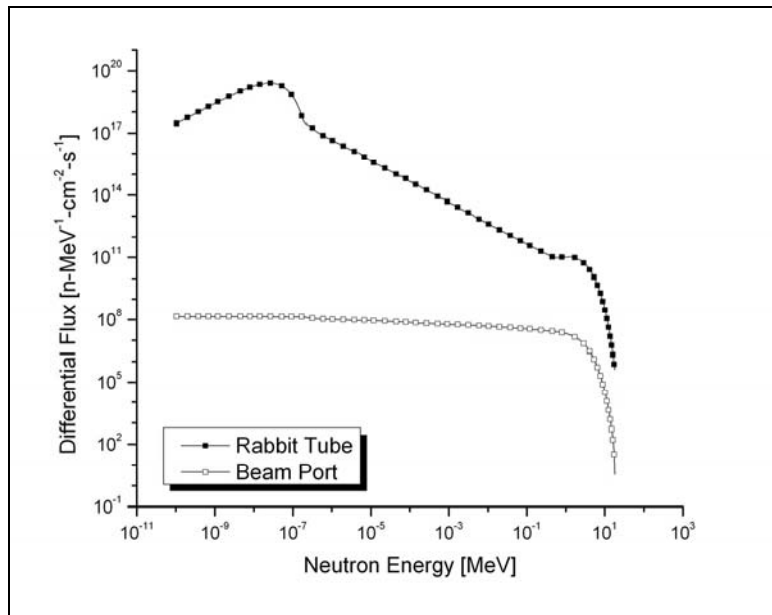


Figure 44. OSURR Neutron Spectrum at 500 kW.

In order to determine the displacement damage effectiveness of various neutron sources (or locations within the reactor), the neutron energy spectrum is reduced to a monoenergetic source with a damage effectiveness equivalent to the entire spectrum. For purposes of radiation testing of electronics, the 1 MeV equivalent neutron fluence for Silicon (1 MeV Eq (Material) or simply 1 MeV Eq) is reported.

The 1 MeV Eq is determined by using MIL-STD-750D METHOD 1017.1. The DoD approved method is outlined in the ASTM E722(1992) standard [58], [59]. The 1 MeV Eq is the fluence required of 1 MeV monoenergetic neutrons to cause the same amount of damage as the entire spectrum for a given material. ASTM E722(1994)

provides the damage functions of both Si and GaAs. Using Equation 42, 1 MeV equivalents can be determined.

$$\phi_{EQ,1MeV,MAT} = \frac{\int_0^{20MeV} \phi(E) F_{D,MAT}(E) dE}{F_{D,1MeV,MAT}} \quad (42)$$

where $\phi(E)$ is the energy-dependent incident neutron energy-fluence spectral distribution, $F_{D,MAT}(E)$ is the energy-dependent neutron displacement damage function for the material of interest (Figure 45), and $F_{D,1MeV,MAT}$ is the displacement damage reference value at 1 MeV. $F_{D,1MeV,Si}$ and $F_{D,1MeV,GaAs}$ are 95 and 70 MeV-mb respectively [59]. Table 8 illustrates the effect of collapsing the spectrum to a 1 MeV Si and GaAs equivalent.

Table 8. Comparison of total flux to 1 MeV Eq neutrons for Si and GaAs.

	Total Flux [n-cm ⁻² -s ⁻¹]	1 MeV Eq (Si) [n-cm ⁻² -s ⁻¹]	1 MeV Eq (GaAs) [n-cm ⁻² -s ⁻¹]
Rabbit Tube ^d	2.63x10 ¹²	1.52x10 ¹³	1.57 x10 ¹³
Beam Port	1.24x10 ⁷	1.95x10 ⁹	2.03x10 ⁹

To determine the NIEL dose of neutrons, a well-known relationship for Silicon is exploited. The neutron NIEL rate at 1 MeV for Silicon is 2.0368 keV-cm²-g⁻¹ [60]. Therefore, maximum dose at 1.2x10¹⁶ n-cm⁻² is 392 krad (Si).

^d Devices placed within the Rabbit tube were Cd shielded. Therefore, the lower limit of integration in Equation 42 is adjusted to the Cd cut-off energy [56]. Devices placed in the beam port need no adjustment because the unfolding is unique to the configuration of the Dewar system (Figure 36).

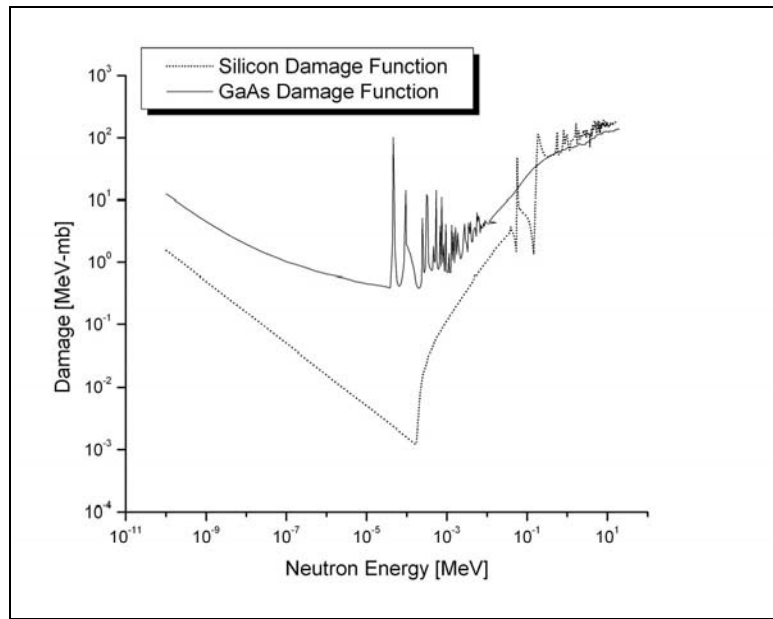


Figure 45. Displacement damage KERMA functions for Si and GaAs.

V. Experimental Results

***In situ* Irradiation Experiment: A25**

The irradiation experiment on device A25 was successful in demonstrating *in situ* measurements at cryogenic temperatures within the BP. Although forced to run at reduced power and duration, a number of startling observations are reported at a total NIEL dose of only 5.4 rad (Si).

The transfer characteristics and extrinsic g_m are shown as a function of neutron fluence in Figure 46. The maximum extrinsic g_m is within the statistical noise and no distinguishable increase observed. However, the slope of the transfer characteristics at the maximum transconductance extrapolated to $V = 0$ yields a decreasing V_{th} (Figure 47).

Even though the total NIEL dose was extremely low, a tremendously large increase in drain current is observed without a correspondingly large increase in gate leakage. All presented I-V characteristics are the gate leakage adjusted drain currents (GLADC). Because the gate leakage is two OOM less than the drain current, adjusting the drain current has little effect. The I-V characteristics are presented as Figure 48 and Figure 49. Note that for Figure 49, the power was reduced 33% at measurement #5 (3.5×10^{10} n-cm $^{-2}$ or 1.14 rad (Si)). The NIEL dose rate up to measurement #5 is nominally 3.44 rad (Si)/hr. After the power reduction, the NIEL dose rate is decreased to 2.30 rad (Si)/hr. The decrease power is clearly noticeable in the decreased slope of increasing drain current after measurement #5 in Figure 49. In fact, nearly 65% of the

increased drain current for $V_g = -2.0$ V occurs in the first 20% of total accumulated NIEL dose.

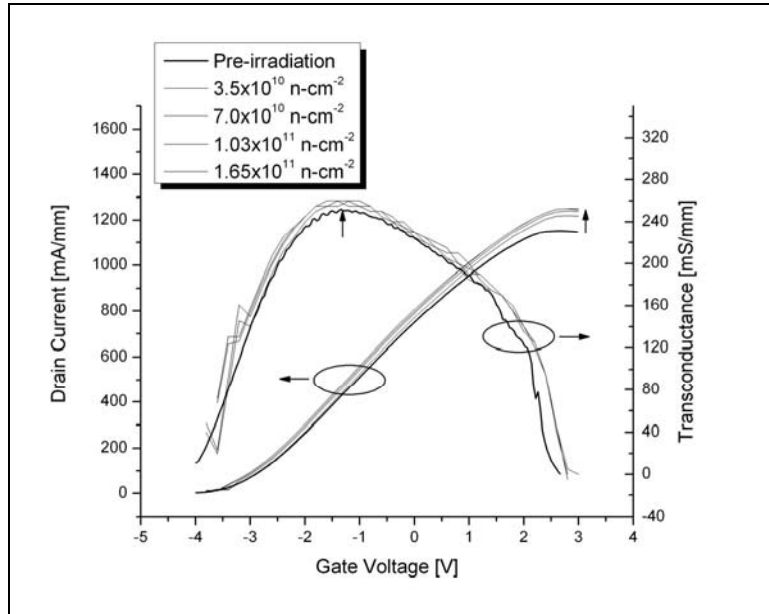


Figure 46. A25: Drain current versus gate voltage and extrinsic transconductance as a function of neutron fluence measured at $V_d = +6.0$ V. The RSD <1.4 %.

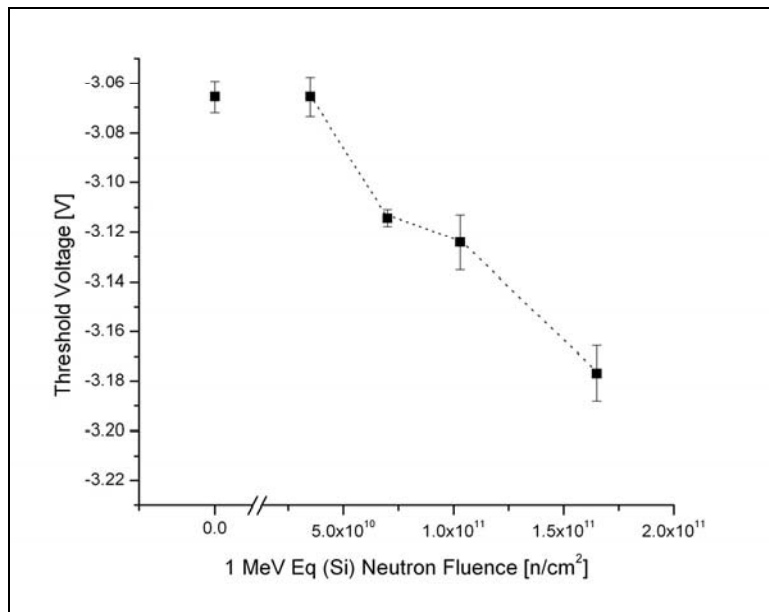
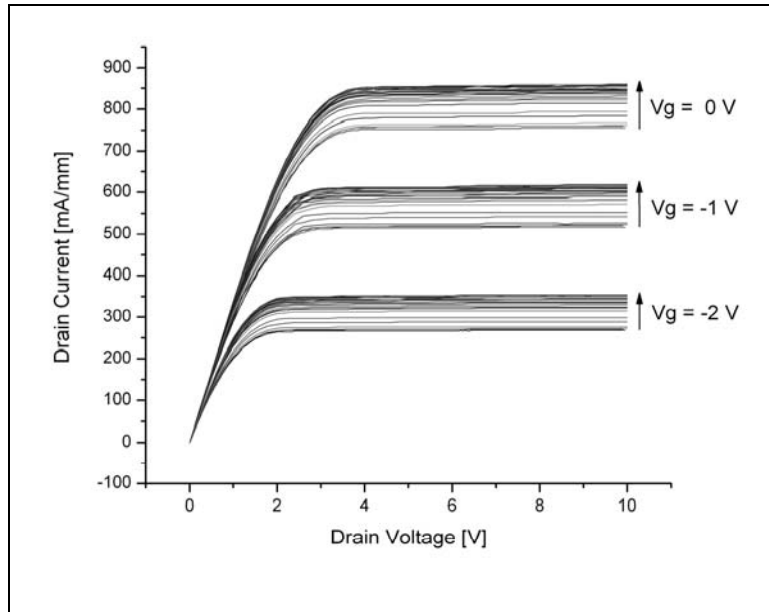


Figure 47. A25: Extracted threshold voltage as a function of neutron fluence.



**Figure 48. A25: I-V characteristics as a continuum of accumulated dose.
The RSD <1.3%.**

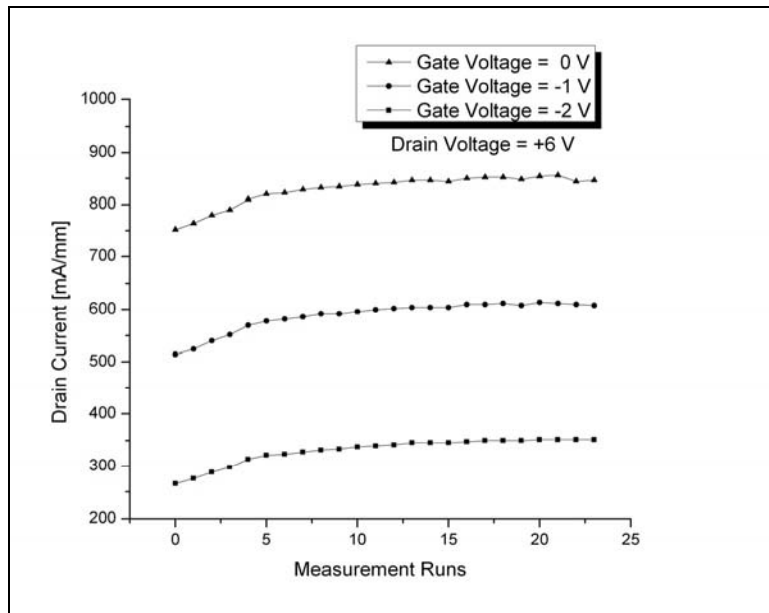


Figure 49. A25: I-V characteristics shown as a function of neutron fluence. The maximum increase in drain current at $V_d = +6.0$ V is 14%, 20%, and 33% for $V_g = 0.0$, -1.0, and -2.0 respectively. The maximum RSD <0.46%.

Measurements conducted from precharacterization (0) to $1.65 \times 10^{11} \text{ n-cm}^{-2}$ (23). Each measurement took ≈ 120 seconds with $\approx 3\text{-}4$ minutes between subsequent measurements.

The gate leakage of device A25 was extremely low and exhibited very little change during irradiation. Figure 50 and Figure 51 both show the gate leakage characteristics as a function of accumulated dose.

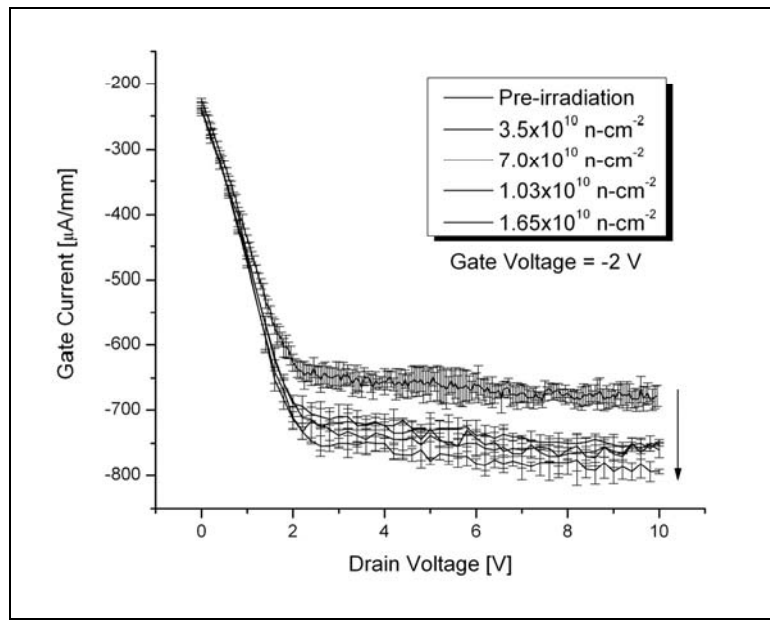


Figure 50. A25: Gate leakage as a continuum of accumulated dose. The arrow denotes a continuous increase of gate current with dose to a maximum increase in magnitude of 16% for $V_g = -2.0$.

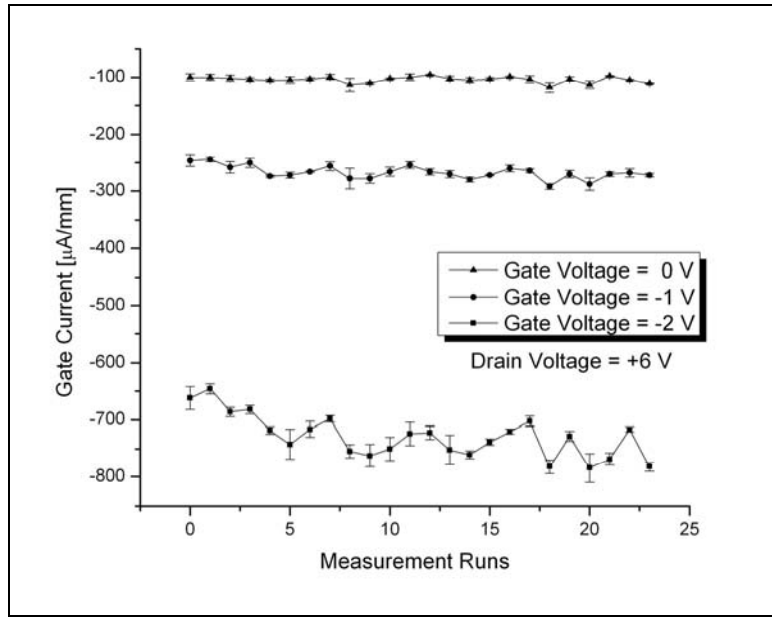


Figure 51. A25: Gate leakage shown as a function of neutron fluence. Measurement run zero represents the pre-irradiation measurement.

Even though the temperature-dependent Schottky measurement was not conducted pre-irradiation, general trends of the single temperature measurement remain valid. In order to obtain a SBH for comparative purposes, the areal Richardson constant AA^{**} is assumed to remain unchanged during irradiation. The post-irradiation value for AA^{**} is $1.0199 \times 10^{-07} \pm 6.0978 \times 10^{-08}$ [A-K⁻²] (Table 15). The SBH increased by approximately 5% at a maximum dose of 5.4 rad (Si). This increase is rather significant given the extremely low NIEL dose. Table 9 is a summary of relevant Schottky diode parameters.

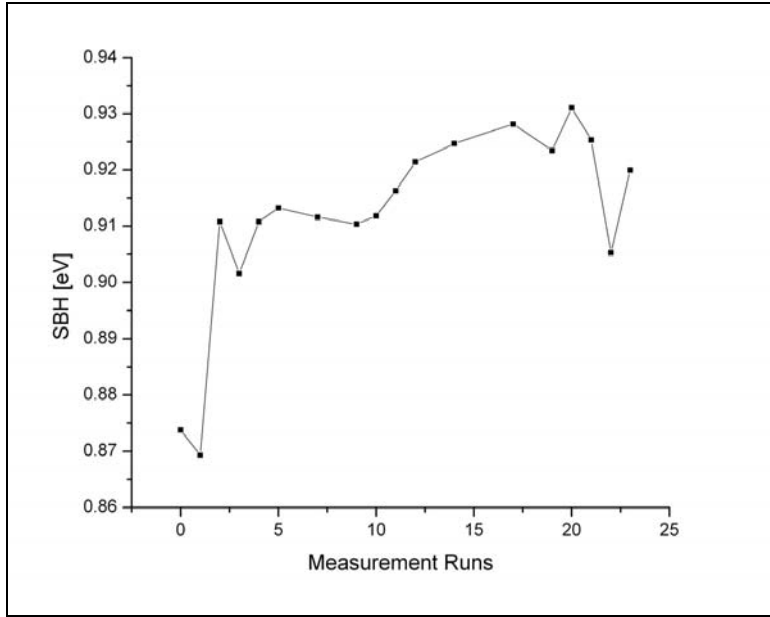


Figure 52. A25: SBH alteration during *in situ* measurements at 80 K. Data points removed that had excessive error in the fitting parameter phi.

Table 9. A25: Summary Table of Observed Schottky behavior.

	SBH [eV]	I_t [A]	E_0 [meV]	R_s [Ω]
Average	0.909 ± 1.94 %	6.22×10^{-12} ± 10.53 %	43.9 ± 1.01 %	27.1 ± 1.75 %
Trend ^e	Increasing	Decreasing	Stable	Stable

Other fitting parameters are shown as Figure 53, Figure 54, and Figure 55. In general, I_{gr} and I_t show decreasing saturation currents. In addition, the reduction in I_t is accompanied by a slight increase in the tunneling parameter E_0 . This relationship is in agreement with Equation 34 in chapter III and in the underlying physics of the problem. That is to say, as the tunneling transparency parameter increases, the barrier becomes more opaque to an electron desiring to tunnel through. Furthermore, R_s shows nearly a

^e I_{te} and I_{gr} are on-the-order of 10^{-65} and 10^{-34} [A] respectively and generally decreasing with increasing fluence.

flat response as parasitic resistance decreases. The decrease in parasitic resistance is also in agreement with the reduction of I_t and increase in SBH. All of the extracted diode parameters are obtained by analysis of data utilizing the six-parameter fitting model discussed in Chapter III.

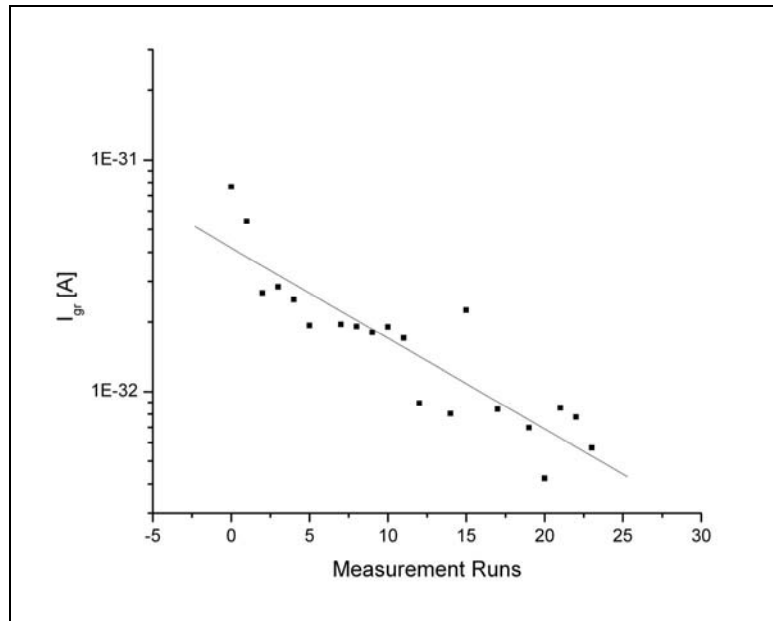


Figure 53. A25: GR saturation current as a function of increasing neutron fluence.

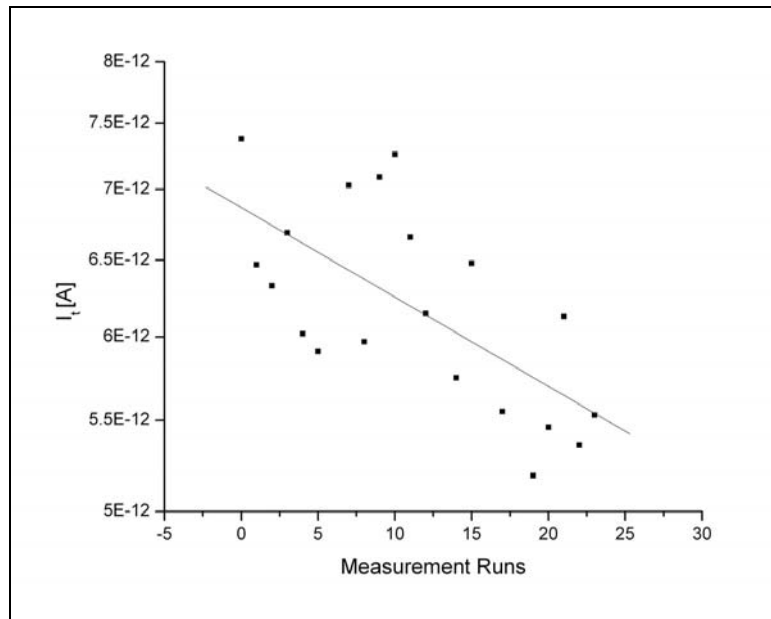


Figure 54. A25: Tunneling saturation current as a function of increasing neutron fluence.

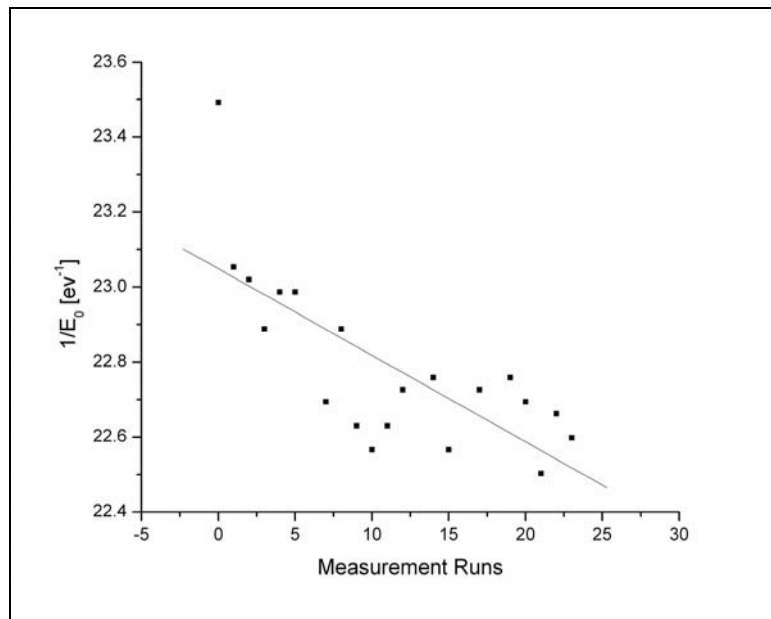


Figure 55. A25: The reciprocal of the tunneling parameter, E_0 as a function of increasing neutron fluence.

Rabbit Tube Irradiation Experiment: A25

Due to radiation safety hazards and an opportunity to gain an extra day at the OSURR, I decided to irradiate at RT within the PART. As previously described, the using of a bracketing technique is employed to determine the fluence at which transistor action fails. The primary assumption being that RT annealing is a slow process, irradiations will be kept short, and measurements made at 80 K “lock in” displacement damage. With these criteria in mind, I set out to continue irradiating device A25.

Before continuing with the radiation plan, device A25 was rebaselined and fully characterized. This included a temperature-dependent Schottky measurement. The temperature profile is shown as Figure 56.

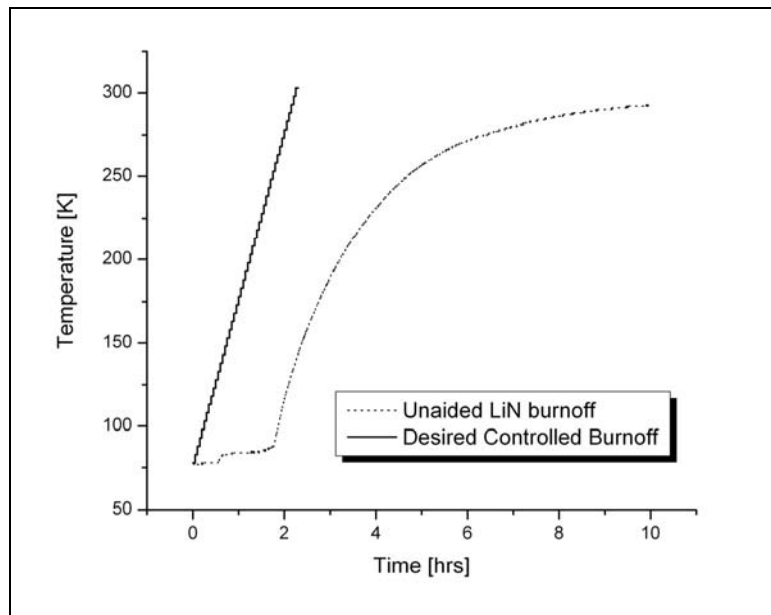


Figure 56. A25: Actual unaided nitrogen burn off shown along with optimal temperature profile.

The following plots are typical of the data extracted from the temperature-dependent experiment (Figure 57, Figure 58, Figure 59, and Figure 60).

Further extraction data is available in Appendix B. The areal Richardson constant, temperature-independent SBH, and E_{00} tunneling parameter were determined to be $1.0199 \times 10^{-7} \pm 6.0978 \times 10^{-8} \text{ A-K}^{-2}$, $0.9832 \pm 8.5796 \times 10^{-3} \text{ eV}$, and $50.9 \pm 0.396 \text{ meV}$, respectively. At 50.9 meV, the system is considered to be FE dominant.

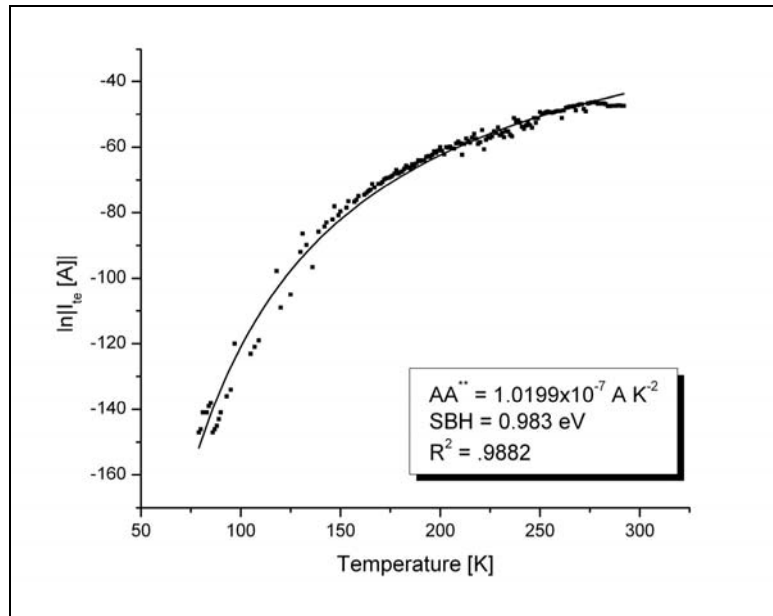


Figure 57. A25: TE saturation current in a wide temperature range.

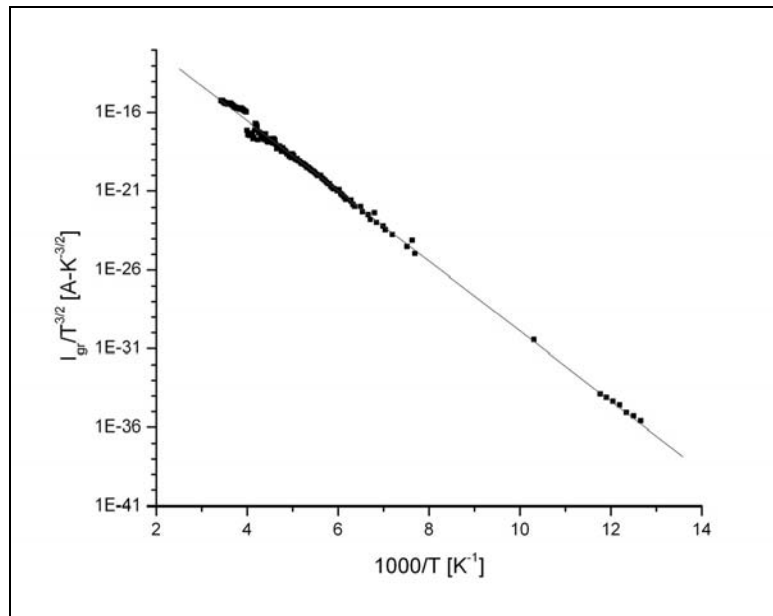


Figure 58. A25: Arrhenius plot of GR saturation current.

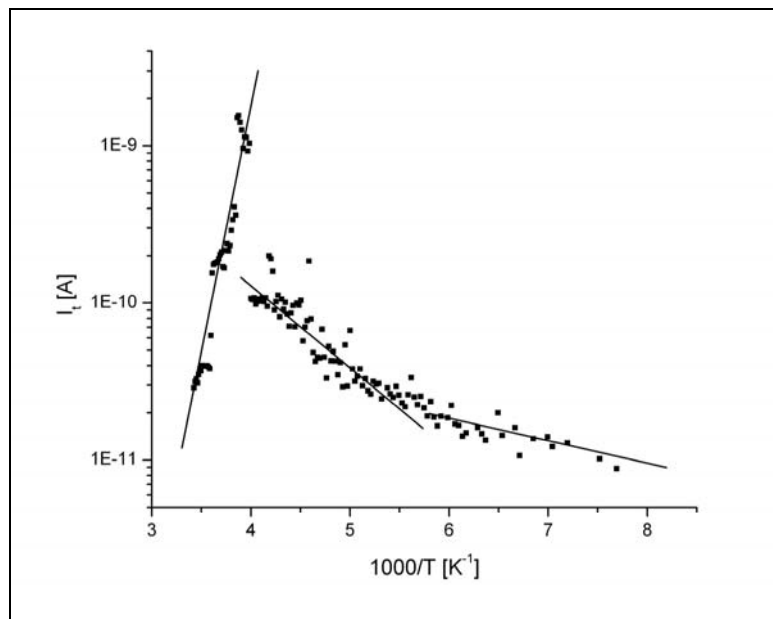


Figure 59. A25: Arrhenius plot of tunneling saturation current with three distinct linear regions shown.

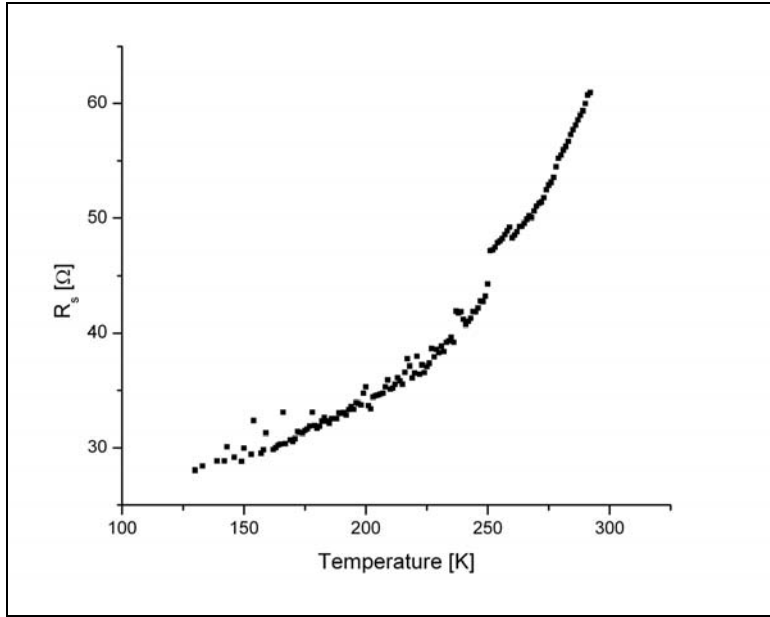


Figure 60. A25: Temperature dependence of series resistance.

Upon characterizing A25 at the end of the temperature profile, no annealing was observed. In effect, the irradiation of the *in situ* measurements would be added to during subsequent irradiations at RT in the PART. Irradiation of device A25 was completed to a total NIEL dose of 1.3 krad (Si) before mechanical failure of the device packaging occurred. The failure mode is similar to static discharge induced damage observed in previous experiments. The transfer characteristics are shown as Figure 61. The maximum RSD of any measurement was 0.8%. The transconductance is not shown and was determined to be statistically unchanged within the entire fluence range. No shift in magnitude or location of the maximum extrinsic g_m was observed.

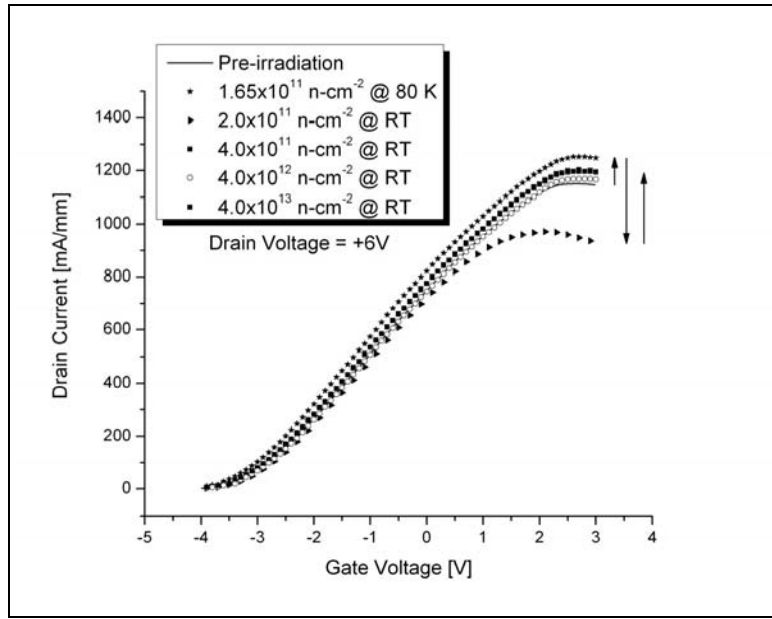


Figure 61. A25: Transfer characteristics at 80 K upon RT irradiation.

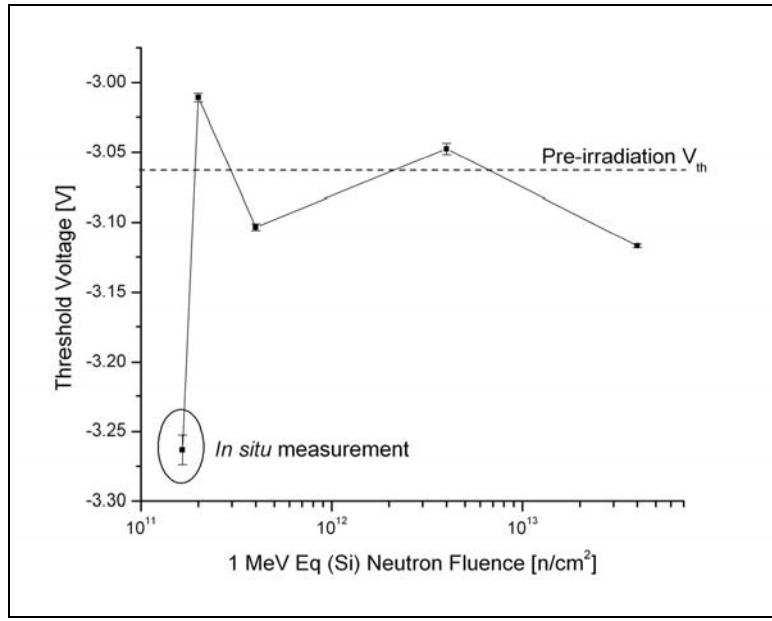


Figure 62. A25: Threshold voltage shift as a function of neutron fluence.

The V_{th} fluctuated about the pre-irradiation value after initially recovering (and overshooting) from the -0.2 V shift. The negatively shifted V_{th} was observed during *in situ* measurements and remained persistent until additional irradiating.

The I-V characteristics also showed an “irradiation annealing” effect where the first irradiation in the PART effectively annealed out the persistent damage remaining from the *in situ* measurement (Figure 63). Similarly, a doubling of the gate current at low fluences levels off with increasing accumulated dose. The gate leakage at the maximum dose is statistically equivalent to the pre-irradiation values.

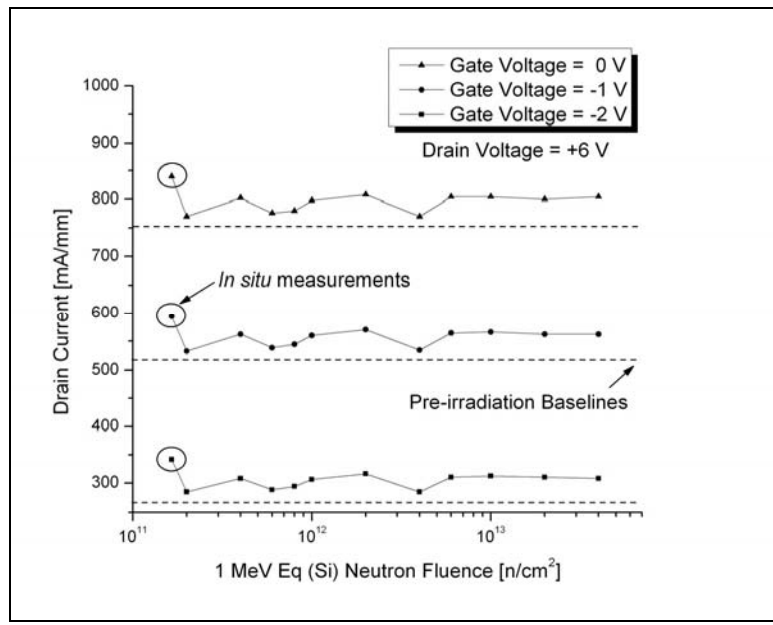


Figure 63. A25: Drain current as a function of neutron fluence at a fixed drain voltage of +6.0 V. The maximum RSD <0.7%.

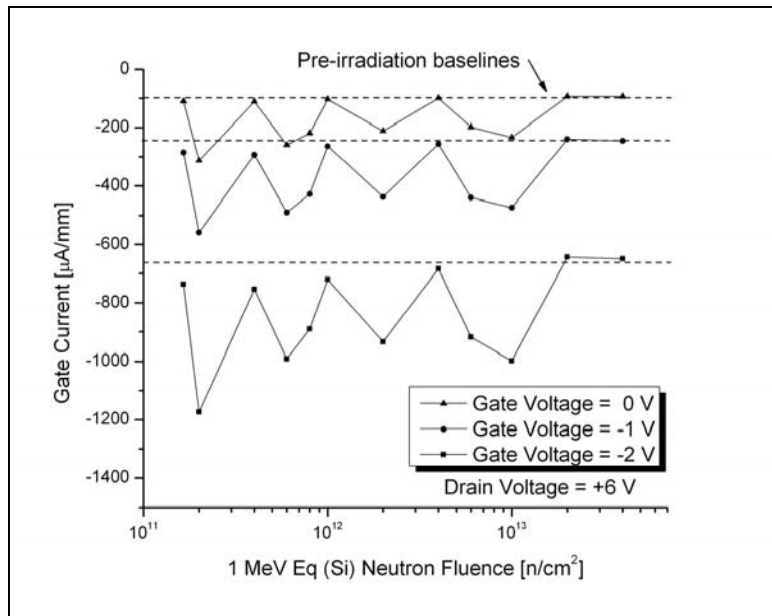


Figure 64. A25: Gate current as a function of neutron fluence at a fixed drain voltage of +6.0 V. The maximum RSD <10%.

Throughout the irradiation, the diode parameters were relatively unchanged and FE is dominant. Table 10 is a summary of relevant Schottky diode parameters and trends.

Table 10. A25: Summary Table of Observed Schottky behavior.

	SBH [eV]	I_t [A]	E_0 [meV]	R_s [Ω]
Average	0.944 ± 1.99 %	1.65×10^{-12} ± 14.75%	46.0 ± 0.66 %	26.8 ± 4.26 %
Trend ^f	5 % Increase	Decreasing	Stable	Stable

Rabbit Tube Irradiation Experiment: A27

In order to confirm the unexpected “irradiation annealing” behavior observed in A25, another device would be irradiated in a similar manner. Device A27 was irradiated at RT in the PART to a total NIEL dose of 8.2 krad (Si). All measurements were made at

^f I_{te} and I_{gr} are on-the-order of 10^{-65} and 10^{-34} [A] respectively and generally decreasing with increasing fluence. R_t fluctuated between 1.5 and 21 M Ω with no discernable trend.

80 K. Transfer measurements and extrinsic g_m are shown as Figure 65 (multiple accumulated dose values not shown for clarity). No shift in either the magnitude or location is observed (outside of statistical uncertainty). Although the transconductance shows no change, V_{th} has a behavior similar to that of A25 (Figure 66). Upon irradiation at low fluences the shift is positive and begins to level off at some negative shift with increasing fluence.

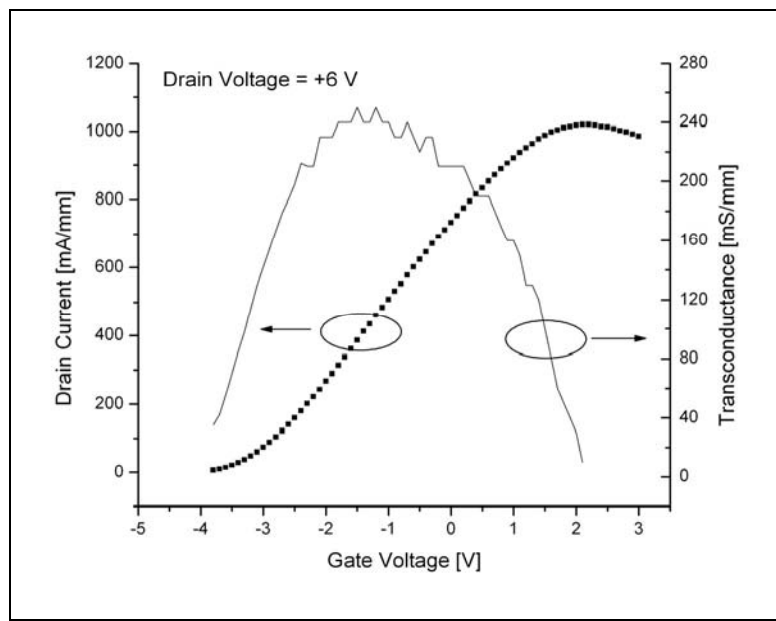


Figure 65. A27: Transfer and extrinsic g_m . The maximum RSD <0.5 %.

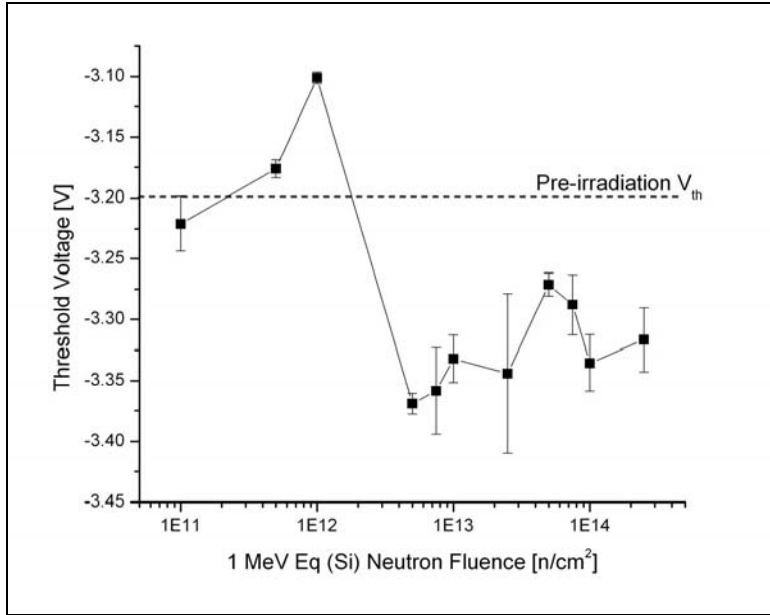


Figure 66. A27: Threshold voltage shift as a function of neutron fluence.

The I-V characteristics of A27 compare well with A25 in the framework of “irradiation annealing”. Device A25 experienced an increased drain current of 14%, 20%, and 33% for $V_g = 0.0$, -1.0, and -2.0 V, respectively. However, at a dose three OOM greater, device A27 experiences half of the increase (Figure 67 and Figure 68). In addition, the gate leakage is only nominally changed at the maximum fluence and remains an insignificant contribution to drain current (Figure 69 and Figure 70).

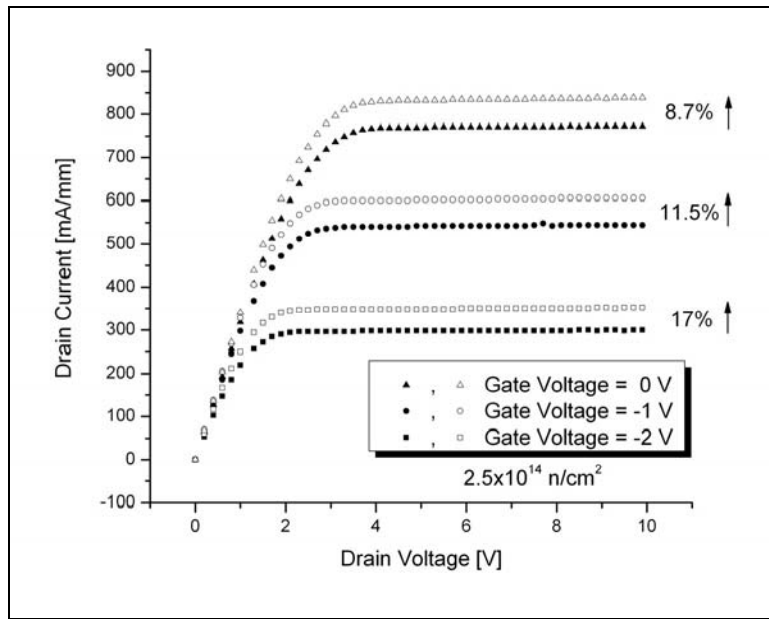


Figure 67. A27: Pre- and post-irradiation characteristics. Closed symbols designate pre-irradiation measurements, and open symbols designate post-irradiation to the specific fluence. Maximum RSD <2%.

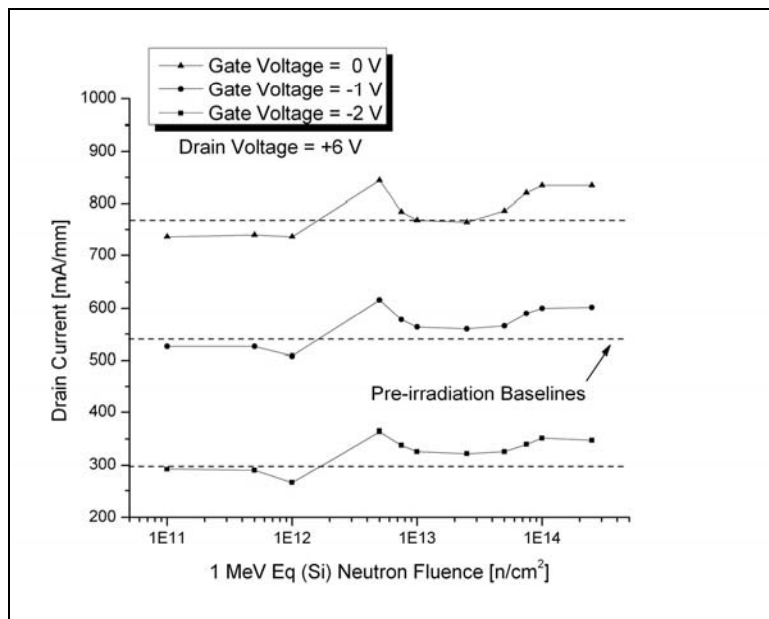


Figure 68. A27: Drain current as a function of neutron fluence at a fixed drain voltage of +6.0 V. The maximum RSD <1%.

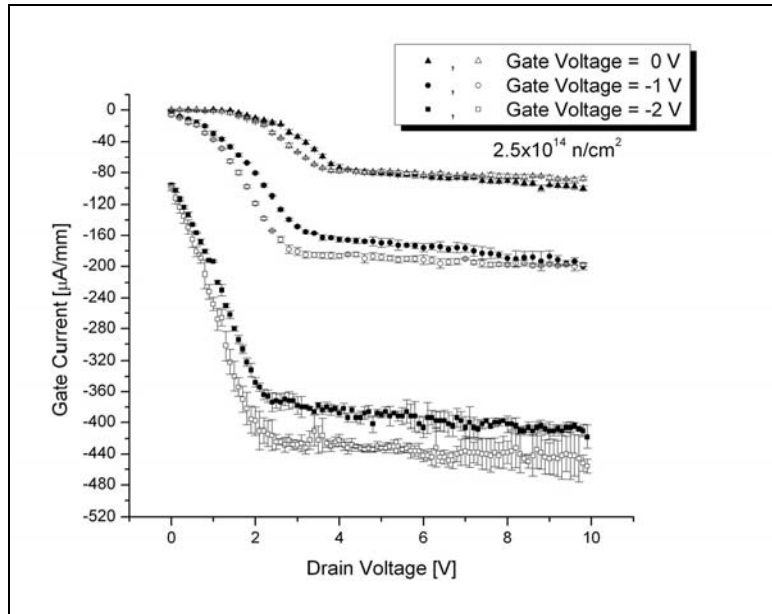


Figure 69. A27: Pre- and post-irradiation gate leakage. Symbols have the same meaning as above.

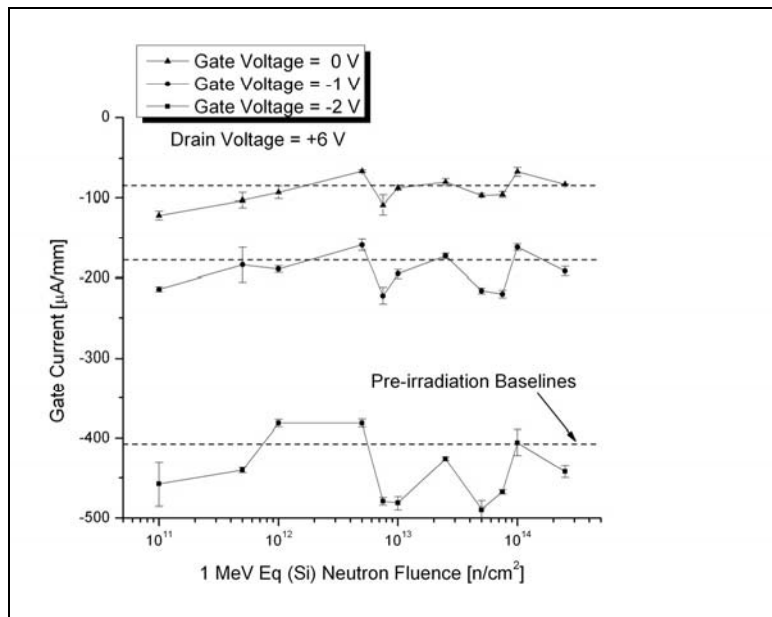


Figure 70. A27: Gate leakage as a function of neutron fluence.

Device A27 exhibited no change in the behavior or mechanism of carrier transport up to a total neutron fluence of $2 \times 10^{14} \text{ n} \cdot \text{cm}^{-2}$. The SBH determined by using an arbitrary

$AA^{**} = 5 \times 10^{-8} \text{ A-K}^{-2}$ yields a pre-irradiation value of 0.857 eV. At the maximum fluence, the SBH increases to 0.917 eV. Simultaneously, R_s is bounded between 23-28 Ω , R_t is bounded between 21-85 M Ω , and the tunneling parameter E_0 is bounded between 35.9-38.7 meV and FE is dominant. There is no explanation for the wide ranging values of parasitic resistance. Table 11 is a summary of relevant Schottky diode parameters and trends.

Table 11. A27: Summary Table of Observed Schottky behavior.

	SBH [eV]	I_t [A]	E_0 [meV]	R_s [Ω]
Average	0.896 $\pm 1.90\%$	2.23×10^{-13} $\pm 21.68\%$	37.6 $\pm 2.38\%$	24.4 $\pm 2.37\%$
Trend ^g	7% Increase	Decreasing	Stable	Stable

Rabbit Tube Irradiation Experiment: A29

The original intent of using the PART was to bracket the upper fluence at which transistor action fails. In order to push the device to extreme limits, an irradiation run was conducted that increased the total NIEL dose from 8.2 krad (Si) to 326 krad (Si) at $10^{16} \text{ n-cm}^{-2}$. Similarly, to previous PART irradiations, device A29 would be irradiated at RT and measured at 80 K. The crucial difference in this run is that the initial fluence is at $10^{15} \text{ n-cm}^{-2}$. At this fluence, no change was observed in the transconductance magnitude or location. However, the V_{th} shifted positive and remained positive throughout irradiation (Figure 71). In addition to the permanent and positive threshold voltage shift, the I-V characteristics exhibited nearly no radiation response. Figure 72 illustrates the

^g I_{te} and I_{gr} are on-the-order of 10^{-65} and 10^{-34} [A] respectively and generally decreasing with increasing fluence. R_t fluctuated between 21 and 86 M Ω with no discernable trend.

pre-irradiation drain current. At a total fluence of 10^{16} n-cm $^{-2}$, the drain current is statistically unchanged. The neutron fluence dependent behavior is shown as Figure 73 below.

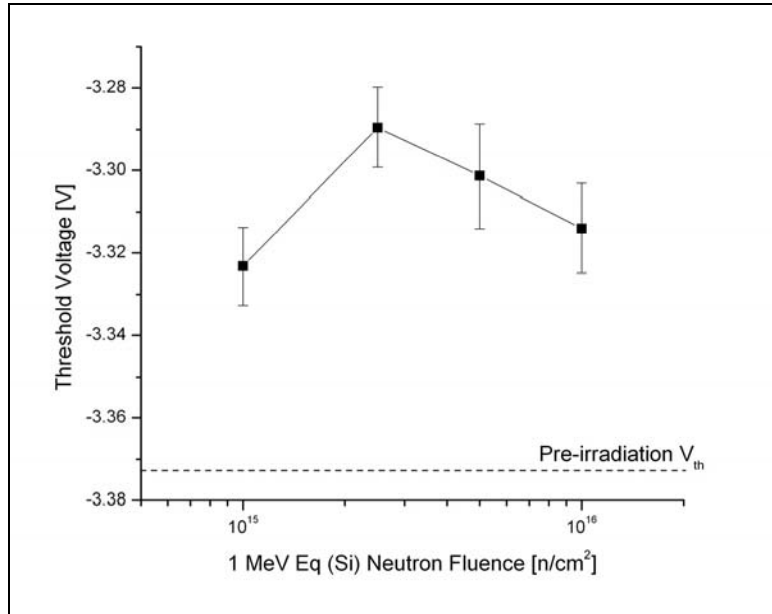


Figure 71. A29: Threshold voltage shift as a function of neutron fluence. The maximum positive shift in V_{th} is 2.5 %.

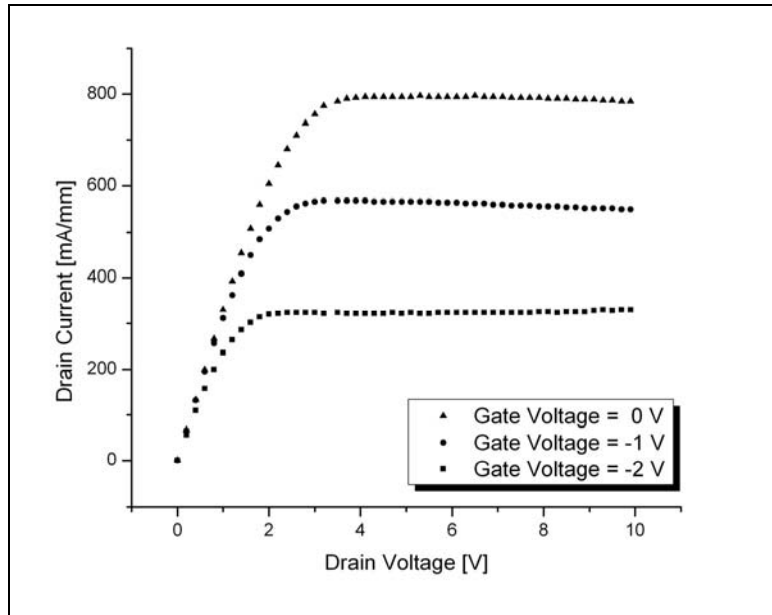


Figure 72. A29: Pre-irradiation I-V characteristics. The maximum RSD <2%.

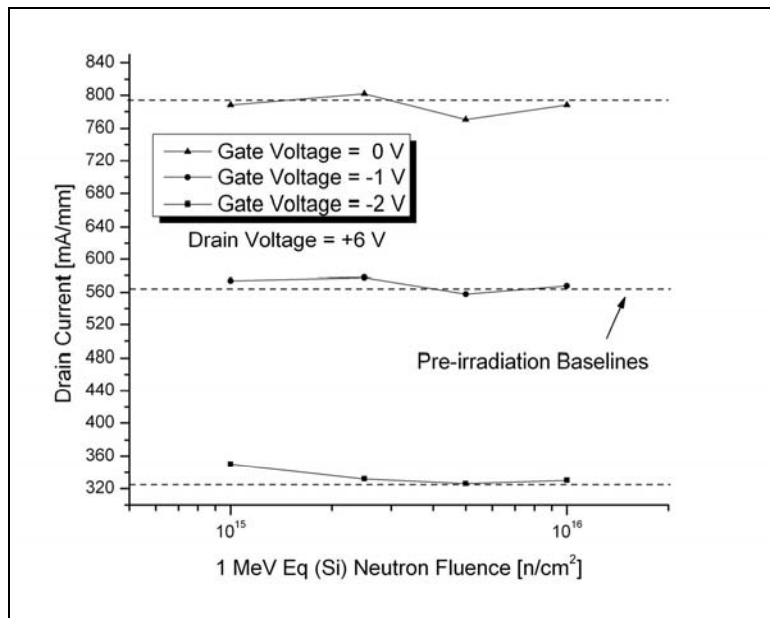


Figure 73. A29: Drain current as a function of neutron fluence at a fixed drain voltage of +6.0 V. The maximum RSD <1.1%.

Perhaps the most surprising result of this irradiation run came from the gate leakage behavior. In all previous irradiations, regardless of the temperature during irradiation, gate current either increased in magnitude or returned to close to the precharacterization value. During this experiment however, the opposite is observed. During high fluence irradiation at RT in the PART, the gate leakage decreased in magnitude in junction with a consistently flat drain current. The pre-irradiation characterization and decreased leakage are shown as Figure 74 and Figure 75.

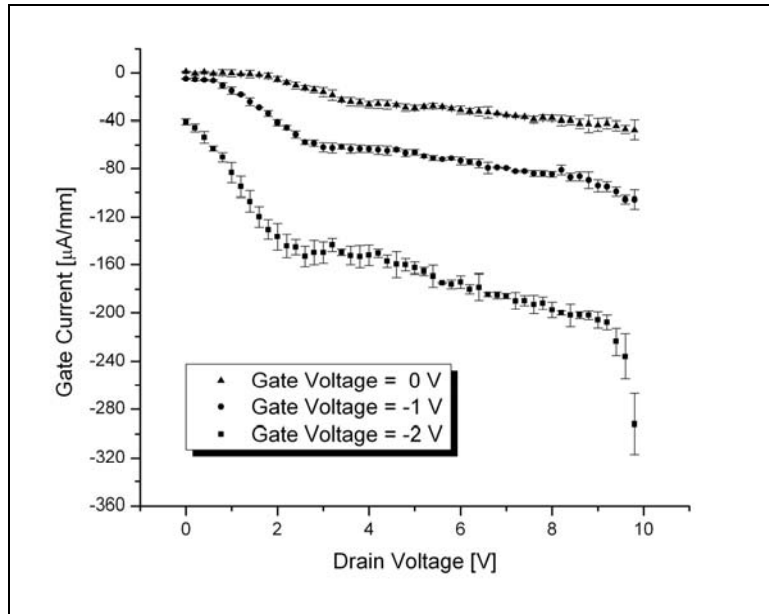


Figure 74. A29: Pre-irradiation gate leakage characteristics.

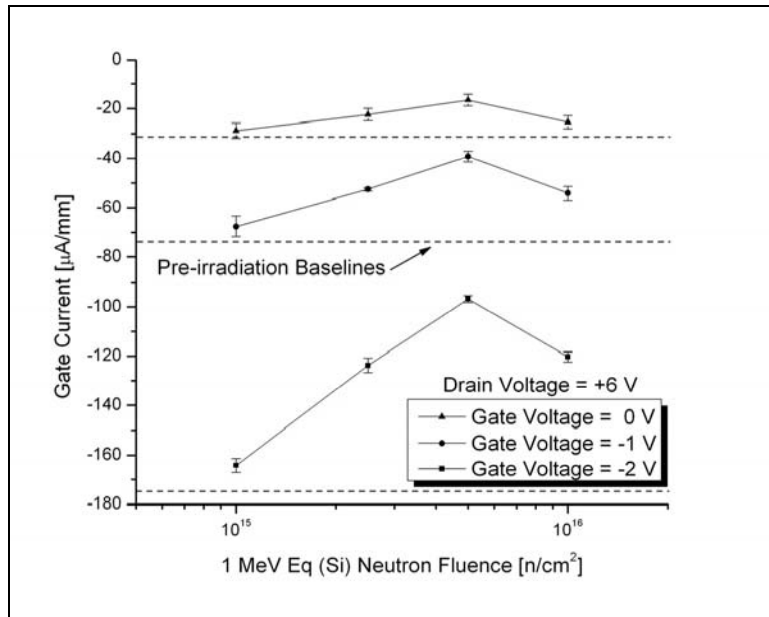


Figure 75. A29: Gate leakage as a function of fluence measured at $V_d = +6.0$ V. The maximum decrease in gate leakage is approximately 45% at 5×10^{15} n·cm⁻² for all gate voltages. The decrease in leakage at maximum fluence is 20, 25, and 30% for $V_g = 0.0$, -1.0, and -2.0 V, respectively.

Upon completion of the maximum fluence, device A29 was stored at RT. The device was again measured 24 and 48 hours later. No change in transconductance was observed. However, V_{th} continued to increase in magnitude (more shift negative) by 17% after 24 hours. At 48 hours no additional shift in either direction is noted. At both 24 and 48 hours the drain current had shifts of less than 2% and are within statistical uncertainty. However, gate current underwent dramatic shifts during both the 24 and 48 hour measurement. Table 12 denotes both the direction and % increase/decrease in magnitude of the gate leakage change. For example, at $V_g = 0.0$ V after 24 hours, the leakage increased in the negative direction by 20%. However, after 48 hours the direction reversed and increased by 20%, resulting in a net 48 hour annealing of 5% in the positive direction (lower leakage).

Table 12. A29: Change of gate leakage magnitude for 24 and 48 hr anneal.

	$V_g = 0.0$ V	$V_g = -1.0$ V	$V_g = -2.0$ V
24 hour	Negative 20%	Negative 7%	Negative 2%
48 hour	Positive 20%	Positive 16%	Positive 18%
Net effect after 48 hours	Positive 5%	Positive 10%	Positive 17%

The Schottky characteristics show a decreased contribution of TE saturation current and a corresponding 10% increase in the SBH with increasing neutron fluence and anneal time (Figure 76). Other trends are difficult to distinguish. However, R_s is bounded between 25-30 Ω , R_1 is bounded between 21-85 $M\Omega$, and the tunneling parameter E_0 is bounded between 35-39 meV.

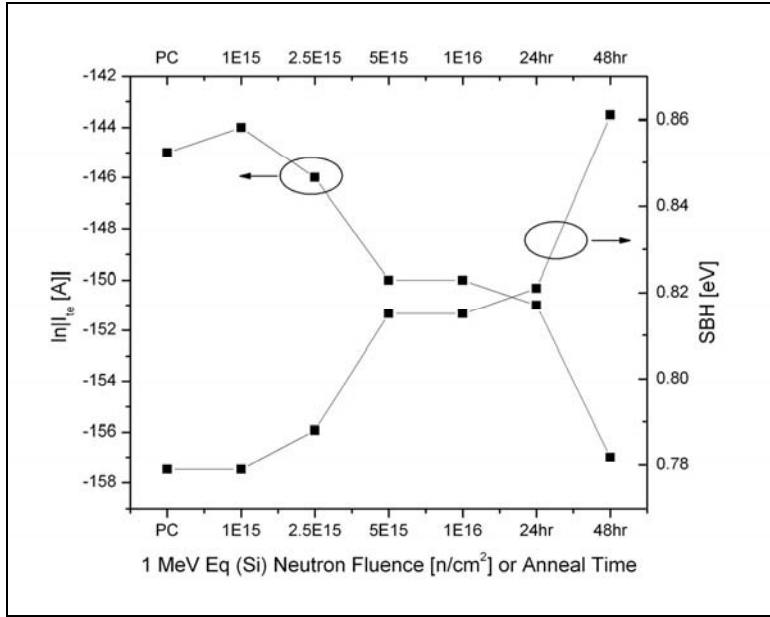


Figure 76. A29: Plot of TE saturation current and SBH as a function of neutron fluence and time of RT anneal. Arbitrary areal Richardson constant of $5 \times 10^{-8} \text{ A-K}^{-2}$ used to determine the SBH.

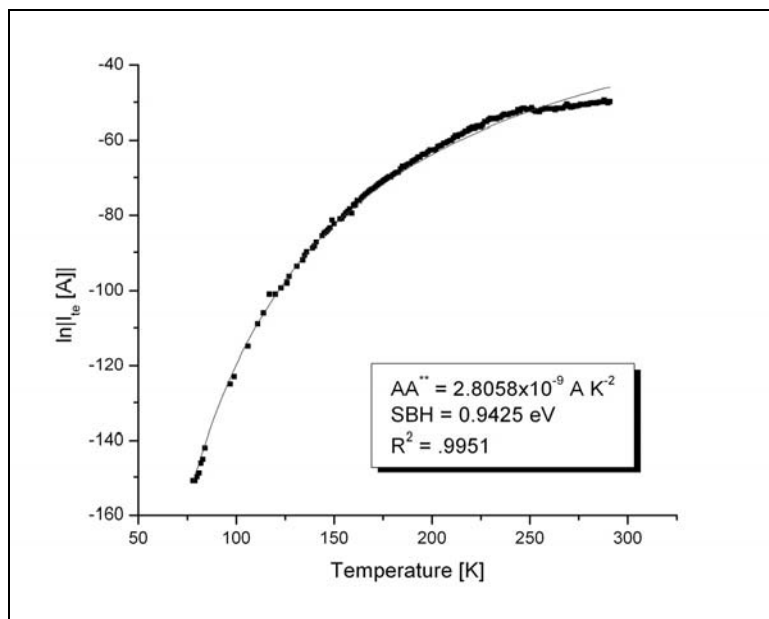
Device A29 exhibited no change in the behavior or mechanism of carrier transport up to a total neutron fluence of $2 \times 10^{14} \text{ n-cm}^{-2}$. The SBH determined by using an arbitrary $AA^{**} = 5 \times 10^{-8} \text{ A-K}^{-2}$ yields a pre-irradiation value of 0.857 eV. At the maximum fluence, the SBH increases to 0.917 eV. Simultaneously, R_s is bounded between 23-28 Ω , R_t is bounded between 21-85 M Ω , and the tunneling parameter E_0 is bounded between 35.9-38.7 meV and FE is dominant. There is no explanation for the wide-ranging values of parasitic resistance. Table 13 is a summary of relevant Schottky diode parameters and trends.

Table 13. A29: Summary Table of Observed Schottky behavior.

	SBH [eV]	I_t [A]	E_0 [meV]	R_s [Ω]
Average	0.922 $\pm 3.19\%$	9.00×10^{-14} $\pm 37.42\%$	37.7 $\pm 2.72\%$	27.0 $\pm 5.23\%$
Trend ^h	9% Increase	Decreasing	Stable	Stable

Rabbit Tube Irradiation Experiment: A30

The final irradiation within the PART consisted of confirming the high fluence behavior. Both pre- and post-irradiation Schottky measurements were conducted, allowing for the first successful comparison of pre- and post-irradiation comparison of the extracted Schottky diode parameters. Figure 78 and Figure 88 illustrate the excellent agreement of the fit to determine the areal Richardson constant, temperature-independent SBH, and E_{00} tunneling parameter.

**Figure 77. A30: Pre-irradiation Schottky diode parameter extraction of the areal Richardson constant and temperature-independent SBH.**

^h I_{te} and I_{gr} are on-the-order of 10^{-65} and 10^{-34} [A] respectively and generally decreasing with increasing fluence.

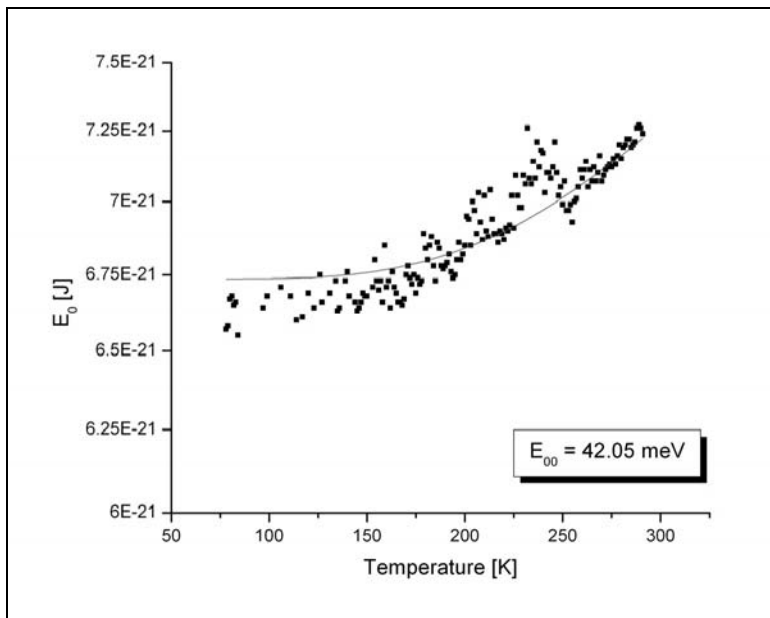


Figure 78. A30: Determination of the tunneling parameter E_{00} from E_0 .

All other extracted parameters follow closely to the plots given for device A25 and the methodology presented in Appendix B.

Following a total fluence of 1.2×10^{16} n-cm⁻², the Schottky contact was recharacterized and yielded a decreased AA^{**} and 16% increased SBH and tunneling parameter E_{00} . Assuming that the Richardson constant is fixed for a device, the decrease in the areal Richardson constant must be due to the increased effective diode area. My hypothesis is that defect-assisted tunneling allows for more current to flow and the effective area appears increased to conserve current density.

Figure 79 through Figure 83 show the comparisons of various Schottky diode parameters before and after neutron irradiation to a total fluence of 1.2×10^{16} n-cm⁻².

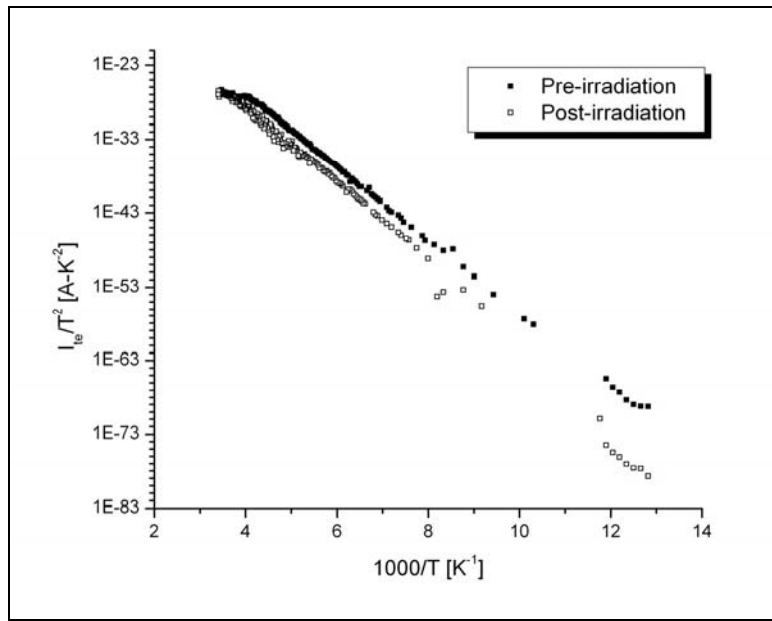


Figure 79. A30: Comparison of TE saturation current following a total fluence of $1.2 \times 10^{16} \text{ n-cm}^{-2}$.

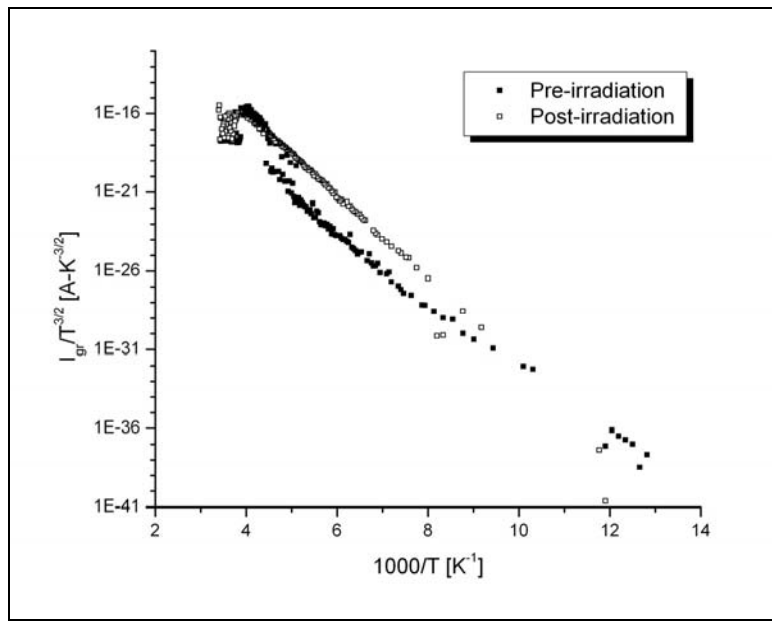


Figure 80. A30: Comparison of GE saturation current following a total fluence of $1.2 \times 10^{16} \text{ n-cm}^{-2}$.

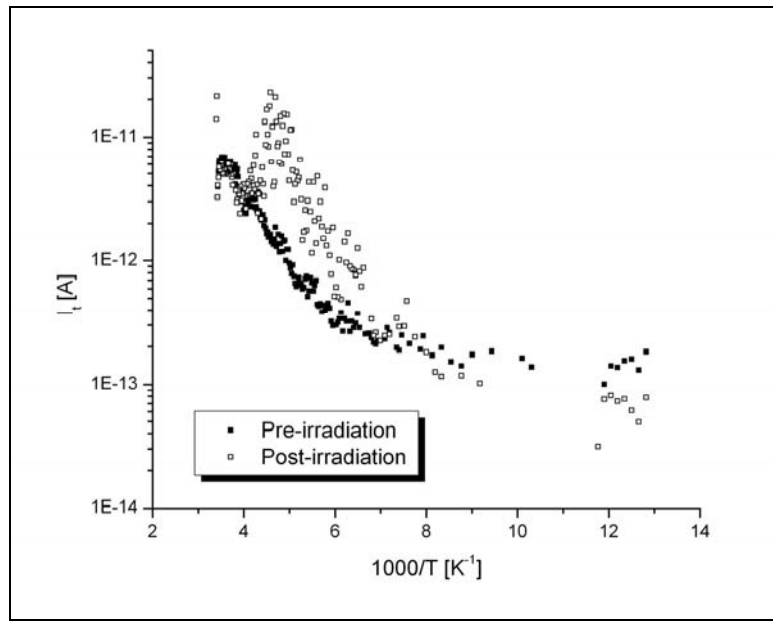


Figure 81. A30: Comparison of tunneling saturation current following a total fluence of $1.2 \times 10^{16} \text{ n-cm}^{-2}$.

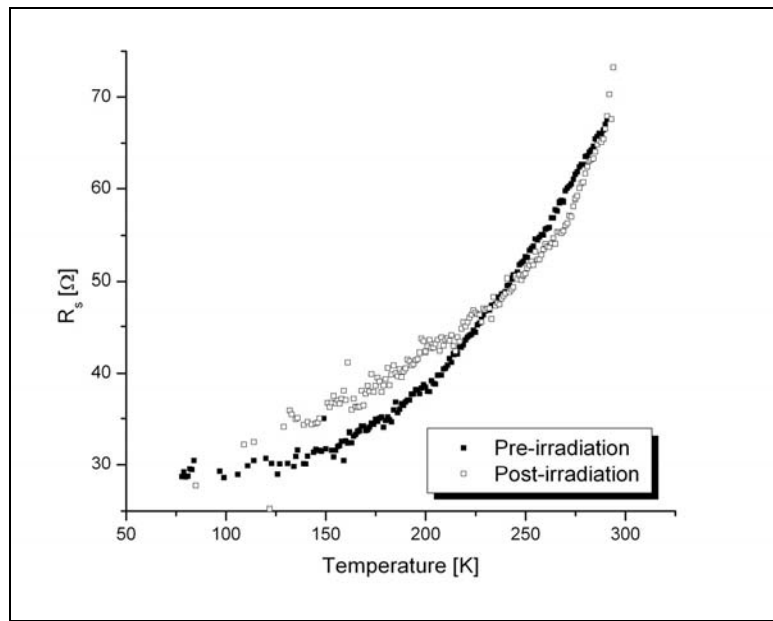


Figure 82. A30: Comparison of tunneling saturation current following a total fluence of $1.2 \times 10^{16} \text{ n-cm}^{-2}$.

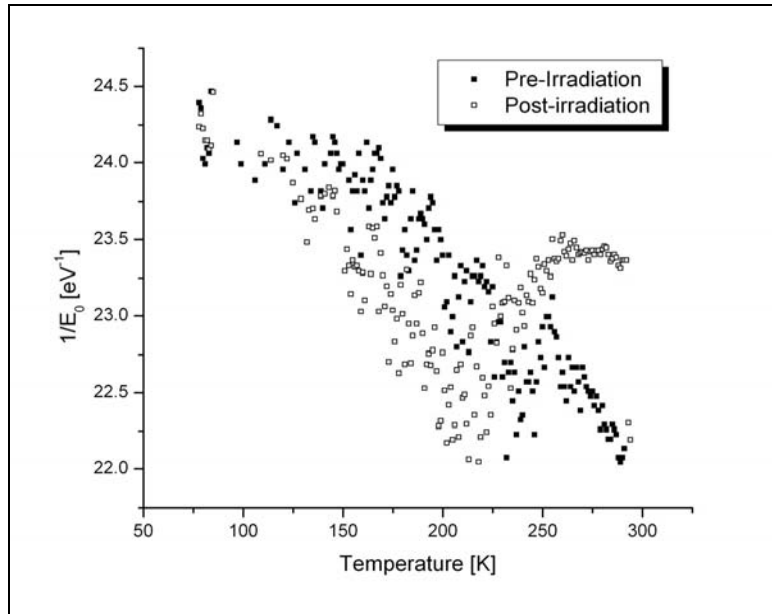


Figure 83. A30: The reciprocal tunneling parameter E_0 , before and following a total fluence of $1.2 \times 10^{16} \text{ n-cm}^{-2}$.

At 80 K, the maximum drain current at $V_g = 0.0$ V is nominally 800 mA/mm. Due to increased lattice scattering, the maximum drain current at RT drops to 200 mA/mm. Simultaneously, the gate leakage increases fivefold for an increase in temperature from 80 K to 295 K. These behaviors are demonstrated in Figure 84, Figure 85, and Figure 86. This portion of the study is to determine the effects of high fluence neutron irradiation to the electrical characteristics at RT. After all, the intended use of GaN-based devices is at ambient or elevated temperatures.

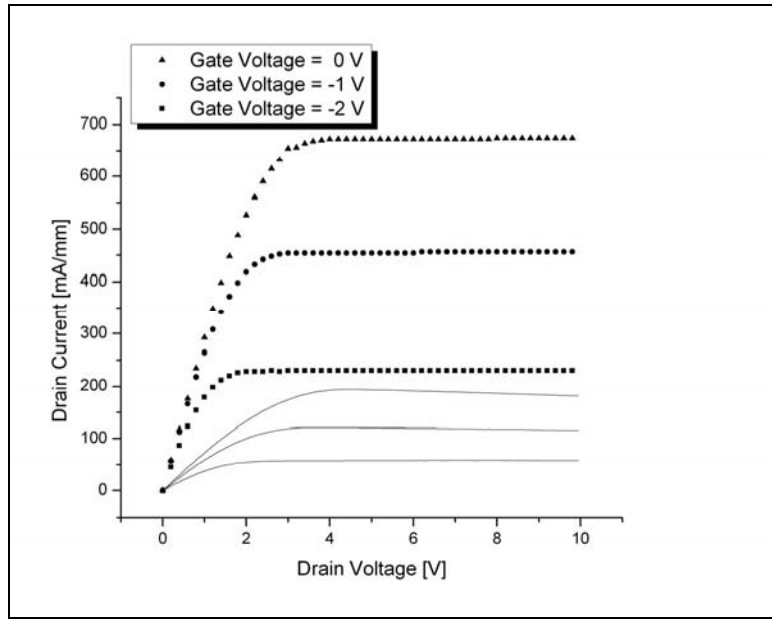


Figure 84. A30: GLADC I-V characteristics at 80 K (symbols) and 295 K (solid line). The maximum RSD <1% at 80 K and <2% at RT.

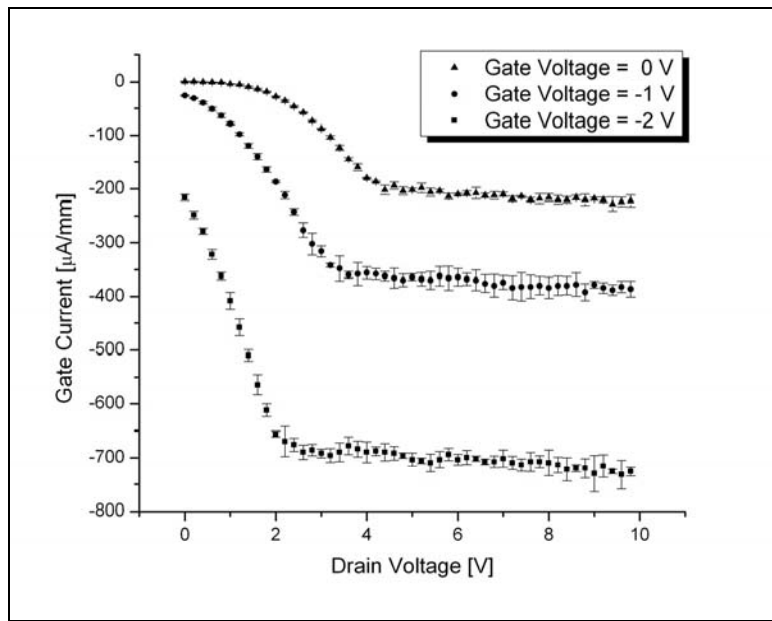


Figure 85. A30: Pre-irradiation characterization at 295 K.

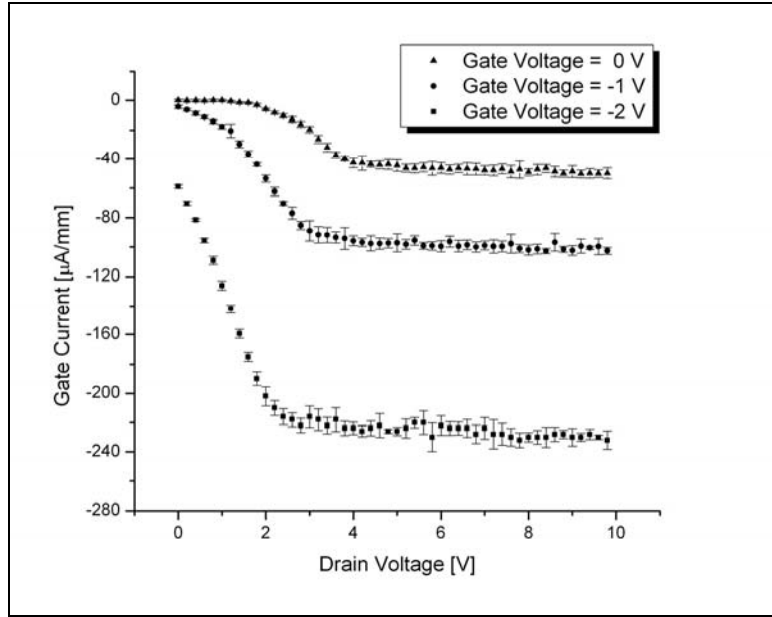


Figure 86. A30: Pre-irradiation characterization at 80 K.

Following irradiation to 1.2×10^{16} n-cm $^{-2}$, the RT electrical characteristics of A30 as a function of fluence behave slightly different than device A29. The primary difference being the negligible radiation response of A29. Figure 87 and Figure 88 show the effect of irradiating to a dose only slightly higher than A29 but A30 exhibits a no vanishing radiation response when measured at RT. This is particularly evident in Figure 88, where after a maximum dose, the drain current remains 14% higher for $V_g = -2.0$ V and $V_d = +6.0$ V. Simultaneously, the gate leakage currents exhibit the same behavior. However, for $V_g = 0.0$, at the maximum fluence the gate leakage is unchanged.

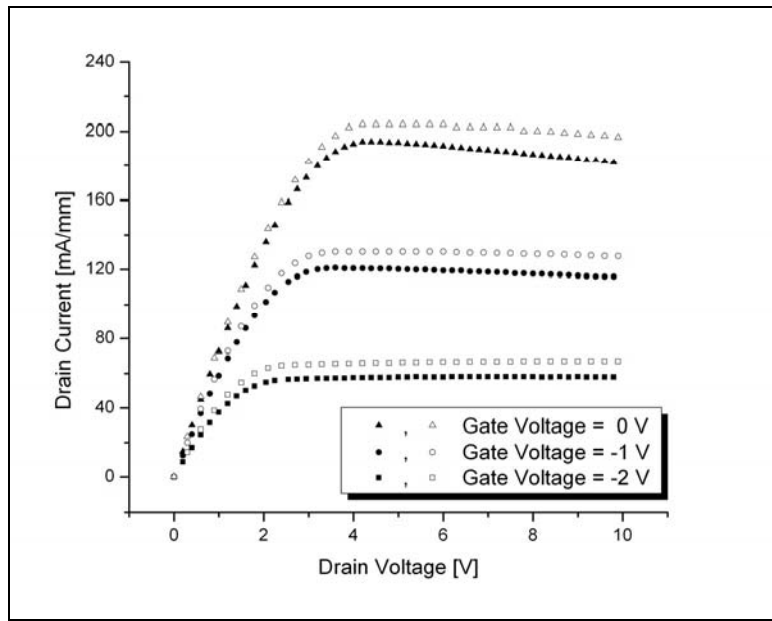


Figure 87. A30: Gate leakage adjusted drain current pre-irradiation (solid symbols) and post-irradiation (open symbols). The maximum RSD for all measurements $<1.4\%$.

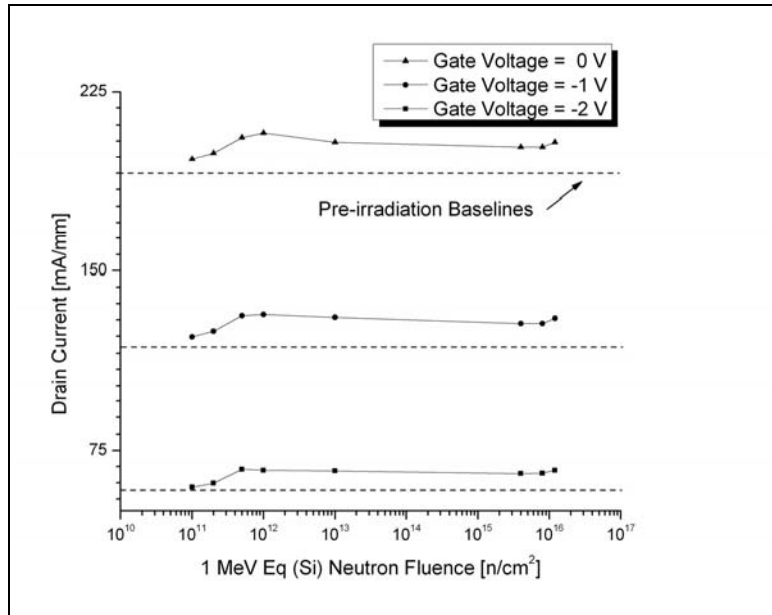


Figure 88. A30: GLADC as a function of fluence measured at $V_d = +6.0$ V. The increase in drain current at the maximum dose is approximately 14, 9, and 6.5% for gate voltages of -2, -1, and 0 V, respectively. The maximum RSD for all measurements is $<0.8\%$.

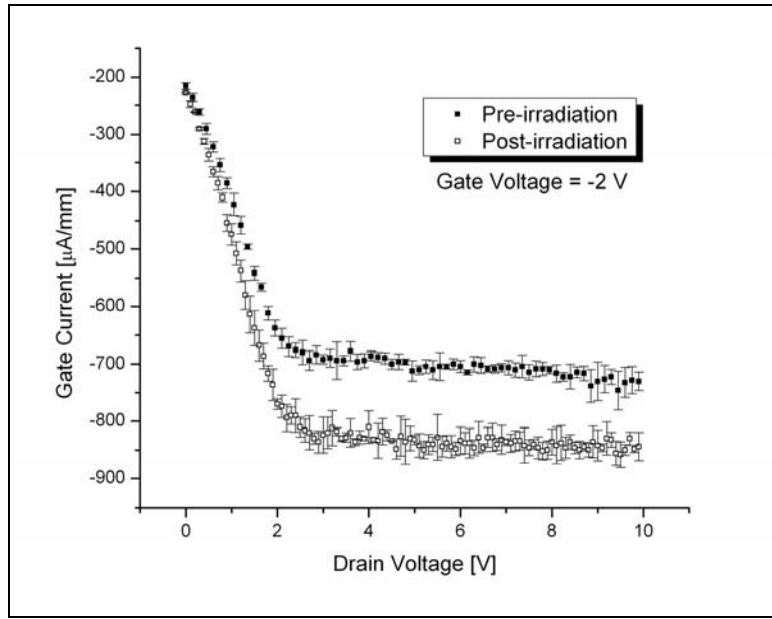


Figure 89. A30: Gate leakage current pre-irradiation (solid symbols) and post-irradiation (open symbols). The maximum increase is nominally 14% for $V_g = -2.0$ V and decreases for increasing gate voltage.

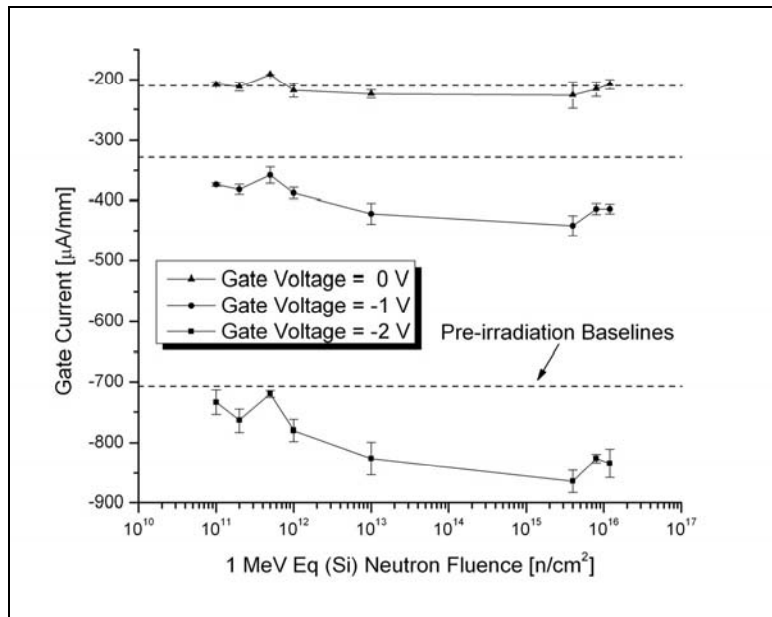


Figure 90. A30: Gate leakage as a function of fluence measured at $V_d = +6.0$ V. The increase in gate leakage at the maximum dose is approximately 18.5, 13.75, and 0% for gate voltages of -2.0, -1.0, and 0.0 V, respectively.

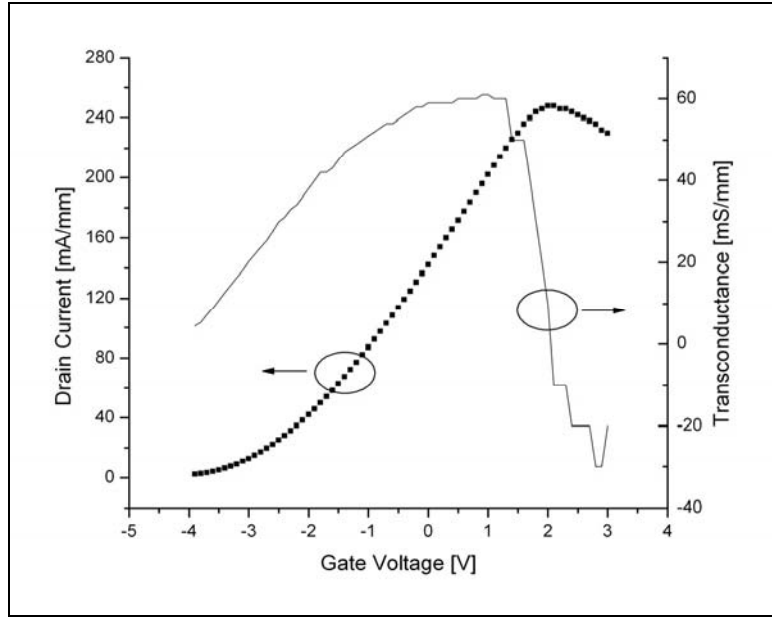


Figure 91. A30: Transfer characteristics and transconductance measured at RT. The maximum RSD <1.5%.

The maximum transconductance at RT exhibited no statistically distinguishable change over five decades of fluence. However, at RT the maximum transconductance location shifts from -1.5 V to +1.0 V. Extrapolation of the transfer curve at the maximum transconductance to $V = 0.0$, yields a threshold voltage that shifted positive nearly 1.0 V to -2.4 V. No radiation-induced changes are observed for V_{th} .

Analysis and Discussion

AlGaN/GaN MODFETs were neutron irradiated and analyzed with a variety of measurement techniques. Most important is the characterization of the Schottky contact utilizing a novel six-parameter fitting routine.

Similar to the results reported by J.M. Sattler, both increased gate and drain currents are observed, thus confirming his effort. The first major radiation effect observed by both endeavors is that of increasing gate current. The origin of increased gate current

(leaky gates) is likely due to a highly doped and/or highly defective surface layer, resulting in carrier transport by tunneling across the Schottky barrier. In addition, the possibility of the Schottky contacts becoming more ohmic-like should not be dismissed. Particularly in light of the fact that RT annealing is virtually non-existent and is expected to be an extremely slow process.

Although multiple processes are likely the source of anomalously large gate leakage currents, for purposes of this research, tunneling currents are investigated. Qualitatively, tunneling through a Schottky contact consists of two parallel transport processes: defect-assisted tunneling and direct tunneling (FE) [30]. Although expected to be dominant at lower temperatures, the tunneling and leakage components of Equation 41 are found to govern carrier transport at all temperatures and thermionic emission is vanishingly small. To account for high leakage currents, various authors theorize a variety of multi-step conduction processes with appropriately assumed special defect distributions to accommodate inconstancies. Specifically, Karmalkar *et al.* assume a uniform distribution of traps throughout the AlGaN layer and spread over an energy band located with the SBH [30].

Yu *et al.* and Miller *et al.* investigated the leakage mechanisms of AlGaN Schottky interfaces based on FE tunneling through a triangular Schottky potential. However, unreasonably high donor densities were required to achieve observed gate leakage values. Therefore, both Yu *et al.* and Miller *et al.* expect other processes such as defect-assisted tunneling to enhance leakage currents. Other published work, including that of Karmalkar *et al.*, all require an unlikely multi-step tunneling process or defect

continuum [55]. Although I confirm that an unreasonably high donor defect density is required to account for pure FE, the donor density does not account for the parallel conduction mechanism of defect-assisted tunneling. Although the six-parameter fitting model is used to analyze the Schottky contact, it is inevitable and unavoidable that charged-carrier transport through the insulating AlGaN layer skews the results. A proposal to independently analyze neutron irradiated AlGaN Schottky diodes is presented in Chapter VI.

Recently, Hashizume *et al.* reported on the strength of the proposed Thin Surface Barrier (TSB) model of anomalously large gate leakage currents. The TSB model indicates that unintentional surface-defect donors reduce the width of the Schottky barrier, which enhances tunneling transport processes. The researchers report that various processing techniques could cause a serious nitrogen deficiency at the m-s interface, resulting in the formation of localized deep donor levels related to the nitrogen vacancy. The TSB model requires that defect donors have an exponentially decaying spacial distribution. The premise of an exponentially decaying special distribution is based upon the observed nature of the nitrogen vacancy, which is assumed to be both a shallow and deep-level donor [55].

The nature of the traps remains ambiguous. J.M. Sattler determined that trap activation energy must be sufficiently low to cause a large increase in the trap concentration when irradiated with 0.45 MeV electrons. Furthermore, other probative studies conducted by Nozaki *et al.* report a specific defect activation energy of 0.28 eV.

Further evidence of tunneling dominance is derived from the tunneling parameters extracted via the six-parameter fitting routine. In particular, the tunneling parameter E_{00} is approximately 40-50 meV for all devices regardless of irradiation level. FE and defect-assisted-tunneling are expected to control when $E_{00} \gg kT$. Clearly, at 80 and 300 K, 40 meV is much greater than the thermal temperature kT . Additionally, from Equation 37, the mechanism of increasing E_{00} is increasing donor density (the only variable reasonably expected to change with irradiation). Although TE is negligible at $T < 500$ K, its effects are further reduced post-irradiation due to an increasing SBH. The increased barrier height further impedes ballistic injection over the barrier. Therefore, the contribution of TE is conclusively eliminated as a source of increased gate leakage.

The second major radiation effect observed and confirmed is that of increasing drain current with fluence. Within the framework of the charge-control model presented by J.M. Sattler, the increased drain current is caused by two distinct possibilities: direct increase in carrier concentration in the 2DEG or 2DEG carrier concentration remains unchanged and the electron mean velocity of the 2DEG increases. However, when using the proposed strain-controlled model by Rashmi *et al.* the possibilities are inestimable. Of particular interest is the effect of strain relaxation or enhancement on the magnitude of drain current. Rashmi *et al.* report increased drain current corresponding to enhanced strain at the AlGaN/GaN interface [45]. Equation 16 is necessary to determine the drain current for strained-heterojunction MODFETs. Use of this full equation is illustrative of the difficulties in attributing observed behavior to simply one distinct possibility.

From Equation 16, only two of the parameters not fixed during manufacturing are known: the applied gate-to-source voltage and threshold voltage. Equation 6 is the simplified model for MODFET threshold voltage that includes the effects of polarization. By appropriately choosing further simplifying assumptions, the remaining unknown terms in the equation, accounting for doping and polarization charge, are likely to dominate changes in the threshold voltage. By choosing a maximum unintentional dopant concentration, the effects of polarization charge can be directly toggled to affect V_{th} . Although polarization changes could be entirely responsible for observed threshold voltage shifts, the other vanishingly small contributions of the SBH and conduction band discontinuity may not be ignored. Further insight is necessary to determine the dominating parameters for V_{th} . The observed threshold voltage shifts followed no distinct pattern and an entire study on this behavior is likely warranted. It becomes increasingly difficult to attribute the changes in the drain current to fluctuations in the threshold voltage because simultaneous increases in both the drain current and decreased V_{th} are observed. Therefore, the saturation drain voltage must be decreasing or the entire product first term of Equation 16 must be increasing as a whole and both large enough to absorb fluctuations in threshold voltage. An agglomeration of these effects cannot be overlooked as a possible source of increased drain current. White *et al.* conclude that although small changes in the polarization can account for shifts in threshold voltage the largest shifts occur at some critical fluence and polarization is unlikely responsible. Instead, mobility continually decreases and once the critical fluence is reached the sheet concentration dramatically decreases to zero [36].

Returning to the framework originally established by J.M. Sattler, another possibility of increased drain current is that of trapped charge in the AlGaN layer. As previously stated, the nitrogen vacancy is an excellent candidate to act as both shallow and deep level donors. The introduction of defect donors is an essential assumption for defect-assisted tunneling and is consistent with increasing drain current.

The introduction of a high density of donor defects within the AlGaN and GaN layers appear as stationary trapped charge. The net effect of a stationary charge beneath the gate is the creation of a virtual image charge needed to balance the trapped charge. The creation of a virtual gate ensues, which acts as an applied bias to the gate since the reference potential is shifted. For n-channel transistors, a net positive trapped charge produces positive vertical shifts in I-V curves (increased drain current). In addition, large concentrations of trapped positive charge act to increase strain at the AlGaN/GaN interface, causing further increase in drain current. Therefore, a mixture of both the virtual gate phenomenon and enhanced strain are proposed as a possible mechanism of increased current.

A study of the annealing effects following a nine month RT anneal confirm that the anneal process is very slow. After nine months essentially no annealing of the drain conduction mechanism occurred. However, the gate leakage recovered to a great extent and fully in some cases. Although annealing is a slow process, it was significant enough to cause a reversal of transistor failure that had occurred nine months previously. The conclusion is that damage is long lived due to the energetically stable Ga and N bonds. However, irradiations at high fluences act to reverse induced damage, perhaps due to

joule heating or additional dislocations that knock atoms into their original energetically favorable and desired lattice position. In addition to joule heating within the device, I believe there may be increased heating of the metallization layer. Heat created throughout the bulk semiconductor material can go either to the package or to the metallization. Since AlGaN and GaN both have high thermal conductivities, heat may be transported out of the bulk and to the substrate and package. This may also explain the epoxy failure when cycling the devices in a liquid nitrogen bath. In that case, the substrate heats up and creates a thermal gradient between the cold package body and warmer substrate that is attempting to dump heat into the epoxy and package.

Overall, the radiation-hardness appears to be dependent on the temperature regime of operation. High-power devices operating within high neutron fluence environments are apparently ideally suited for GaN-based devices. However, it is clear that reduced temperature operation effectively maintains damage and results in significant changes in both the gate and drain current at a dose of only 5.4 rad (Si).

VI. Conclusions and Recommendations

Conclusions

Neutron irradiation of AlGaN/GaN MODFETs confirm results from electron-irradiated devices from the same wafer. Temperature-dependent Schottky measurements confirm the presence of a significant contribution to gate leakage from tunneling current. In addition, the tunneling parameter E_{00} , confirms the presence of field-emission dominated charged carrier transport.

Neutron irradiations at cryogenic temperatures show both increased drain and gate current at the relatively low dose of only 5.4 rad (Si). However, neutron fluences five OOM greater induced comparatively little radiation response when irradiated at RT.

During irradiation, the SBH and tunneling parameter increased, signifying an increase in the density of donor defects and FE tunneling contribution. The effects of irradiation on device behavior are as follows:

- Increased gate leakage current
- Increased drain current
- No change in magnitude or location of maximum transconductance
- Meandering threshold voltage shifts both positive and negative

A study of the annealing effects following a nine month RT anneal confirm that the anneal process is very slow. After nine months essentially no annealing of the drain conduction mechanism occurred. However, the gate leakage recovered to a great extent and fully in some cases. Although annealing is a slow process, it was significant enough to cause a reversal of transistor failure that had occurred nine months previous. The conclusion is that damage is long lived due to the energetically stable Ga and N bonds.

However, irradiations at high fluences act to reverse induced damage, perhaps due to joule heating.

Although I cannot conclusively determine whether FE or defect-assisted tunneling is responsible for the increased gate leakage, the large donor-density (10^{24} cm^{-3}) required by FE alone is coherent with the presence of an alternate and parallel conduction mechanism. However, the high density of donor defects required for FE supports the transition of the Schottky contact from rectifying to more-ohmic like during irradiation. This transition would certainly provide an additional source of electrons and enhanced drain current. The disjointed nature of the drain and gate current has yet to be determined. However, both the drain, gate, and Schottky contact behaviors are well supported by the supposition that a high density of donor defects control the current mechanisms. Additionally, the donors are effective conduction paths for defect-assisted tunneling, and thus lessen the unrealistically high donor density required for pure FE.

Although Rashmi *et al.* have proven that enhanced strain can also result in an increased drain current, the mechanism of enhancing strain by neutron bombardment is unlikely. Simply stated, a fluence of $1.2 \times 10^{16} \text{ n-cm}^{-2}$ is not sufficient to make the argument that enough atoms have been displaced from the lattice into a position that would also enhance strain. Although the irradiations at 80 K prove that the persistence of such dislocations (even though produced in small amounts) can significantly alter device behavior and radiation response.

Finally, the hypothesis is supported with the observation of the increasing Areal Richardson constant. Since the constant is solely dependent on the effective mass

of an electron in the conduction band, and not expected to vary, the only conclusion is that the effective diode area increased. Although unfounded, I propose that this is wholly consistent with defect-assisted tunneling. Since the introduction of defects act as alternate conduction paths, the effective area of charged carrier transport is increased. That is to say, the higher the donor defect concentration, the greater opportunity an electron has to transport to the 2DEG. This supposition is also self-consistent with the proposed FETFET failure mechanism at sufficiently high neutron fluences. When a critical number of conduction paths are created, the AlGaN layer transitions from an effective insulator to a conductor and the conduction area is increased.

Recommended Further Work

The possibilities for further investigation into AlGaN/GaN MODFETs are nearly endless. However, the most immediate and evident recommendation for further work stems from the shortcomings of this particular research endeavor. Although, some important behaviors and relationships have been observed, continuing this specific line of research can yield valuable information. In particular, a complete *in situ* measurement suite at cryogenic temperatures must be completed. The research has shown that irradiating at RT is not the desired method to probe changes in electrical characteristics. In addition, radiation-induced failure has probative value that was not exploited in this undertaking. Without achieving catastrophic failure of transistor action, little changes in transconductance are observed. Without changes in transconductance, the first ever neutron damage constant for transconductance for GaN remains elusive. I also

recommend further investigation of irradiating devices multiple times to observe the hypothesized “irradiation annealing” behavior.

Measurement of the Schottky contact and subsequent diode parameter extraction is difficult and limited in scope. Therefore, it is particularly important to compare the obtained results to another method such as C-V. Additionally, there are a plethora of new emerging models that require experimental verification. Use of defect-assisted tunneling model instead of a TE based model may provide further insight, especially if probed with charged particles.

The examination of Schottky contacts on AlGaN would be of tremendous use in sorting out the charged carrier transport through the contact as opposed to transport through the AlGaN layer. Although device level testing provides great insight into total system behavior, I believe that some more preliminary simple device work would greatly value add to these findings. Also proposed is the use of the test structures to obtain material baselines as well as device behaviors.

Perhaps the most compelling question that needs answering is that of annealing. Although I generally agree with the reported work of J.M. Sattler, I contend that RT annealing is an extremely slow process and negligible on the time scale of this research endeavor. In fact, a nine-month anneal study demonstrated competing annealing process for the gate and drain conduction mechanisms.

Temperature-dependent measurements must be made more experimentally robust. Use of a temperature controller would facilitate obtaining pre- and post-irradiation Schottky characterizations. The addition of a controller would increase the data quality

and quantity during temperature ramps, would enable irradiation studies at various temperatures, and would allow for rapid annealing experimentation.

All of these improvements are designed to compliment the current state-of-the-art in radiation testing of AlGaN/GaN MODFETs. I have concluded that this research is a success if used as the next stepping stone across the river of knowledge.

Appendix A – Nitride Parameters

Property (units)	Units	GaN	AlN
Density [61]	g-cm ⁻³	6.15	3.23
Static Dielectric Constant [61], [62]		8.9	8.5
High Frequency Dielectric Constant [61], [62], [63],		5.35	4.77
Energy Gap (Γ Valley) [64], [65]	eV	3.39	6.2
Effective Mass (Γ Valley) [62], [63], [61]	m_e	.20	.48
Lattice Constant, a [66]	\AA	3.189	3.11
Lattice Constant, c [66]	\AA	5.185	4.98
Electron Mobility [67], [68]	cm ² -V ⁻¹ -s ⁻¹	1000	135
Hole Mobility [66]	cm ² -V ⁻¹ -s ⁻¹	30	14
Saturation Velocity [64], [68]	cm-s ⁻¹	2.5x10 ⁷	1.4x10 ⁷
Peak Velocity [64], [68]	cm-s ⁻¹	3.1x10 ⁷	1.7x10 ⁷
Peak velocity field [61], [68]	kV-cm ⁻¹	150	450
Breakdown field [66]	V-cm ⁻¹	>5x10 ⁶	
Light hole mass [66]	m_e	0.259	0.471
Thermal conductivity [66]	W-cm ⁻¹ -K ⁻¹	1.5	2
Melting temp [66]	°C	>1700	3000
Index of Refraction [4]		2.35 @ 1240nm 2.85 @ 363nm	2.15 @ 413nm 2.85 @ 363nm

Appendix B – Schottky Diode Parameter Extraction Methods

Thermionic Emission Theory

The extraction methods of Schottky diode parameters are imprecise and varied. Although I-V measurements are by far the easiest to perform, the results obtained from I-V characteristics are sensitive to interface defects and are typically the least reliable [47]. Diode parameter extraction via I-V methods is limited in accuracy to prior knowledge of the Richardson constant and the temperature dependence of TE saturation current. Because the Richardson constant varies greatly with processing techniques, an independent I-V technique is necessary for accurate parameter extraction. Fortunately, A^{**} appears in the “ \ln ” term and an error of two in A^{**} gives rise to an error of $0.7kT/q$ in the SBH. More important, is the temperature dependence of the TE saturation current, which dictates the temperature dependence of the SBH (if any). A Richardson plot and subsequent extraction of the constant are obtained by measuring the I-V characteristics of a Schottky contact in a wide temperature range – the so-called I-V-T method.

Analysis of a Schottky contact using only thermionic emission theory results in an extreme overestimate of the thermionic emission saturation current and the contribution of TE to total current flow. Additionally, when other current transport mechanisms are neglected, TE theory alone underestimates the total current flow. The resulting discrepancies lead to ideality factors much greater than unity, Schottky barrier heights are greatly reduced, falsely temperature dependent, and the effective Richardson constants are simply invalid.

A simple extraction of the SBH can be obtained from the linear portion of a semi-log plot of the current. This process is shown in Figure 92 and Figure 93. The barrier height is most commonly calculated from the TE saturation current determined from linear extrapolation to $V=0.0$. This method is illustrated in Figure 93. The one drawback is the previously mentioned need for prior knowledge of A^{**} . Therefore, the SBH cannot be immediately determined by this method. Using the equations given below, the ideality factor and saturation current are calculated. Recall that the non-ideal TE emission equation is:

$$I = I_0 \left(\exp \left[\frac{qV}{nkT} \right] - 1 \right) \quad (B1)$$

Fitting this to the equation of a straight line yields:

$$y = mx + b \Rightarrow \ln|I| = \ln \left| AA^{**} T^2 \exp \left[\frac{-q\phi_B}{kT} \right] \right| + \frac{q}{nkT} V \quad (B2)$$

where

$$y = \ln|I_0|, m = \frac{q}{nkT}, x = V, b = \ln \left| AA^{**} T^2 \right| - \frac{q\phi_B}{kT} \quad (B3)$$

The linear portion of the semi-log plot in Figure 93 is current flow due to TE of carriers over the Schottky barrier.

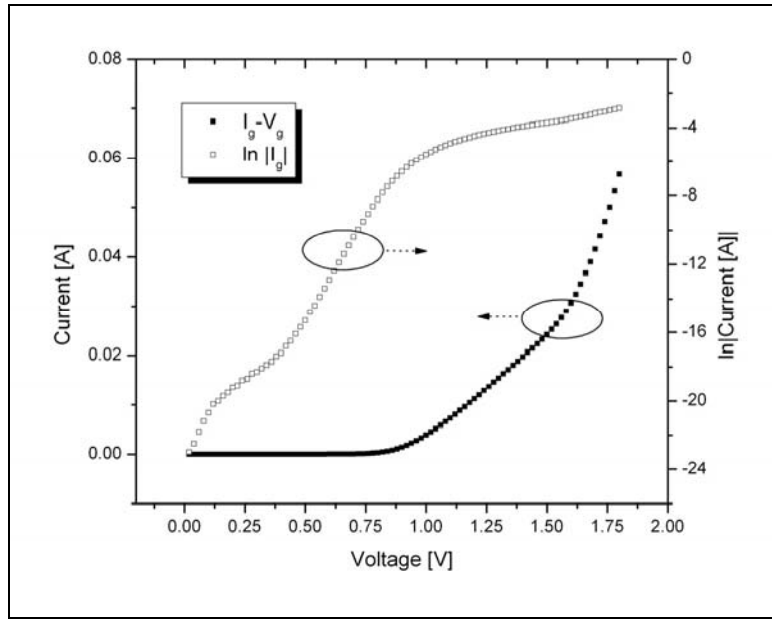


Figure 92. Sample Schottky diode curve at 80K.

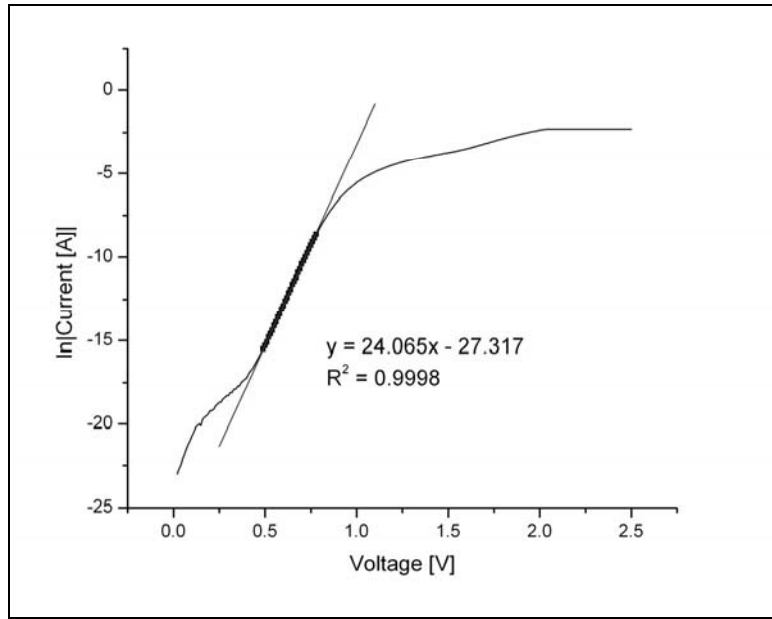


Figure 93. Semi-log current plot for Schottky diode parameter extraction.

The ideality factor and saturation current are 6.03 and 1.37×10^{-12} A respectively for Figure 93 at 80 K. Repeating the extraction technique over a wide temperature range yields Figure 94 and Figure 95.

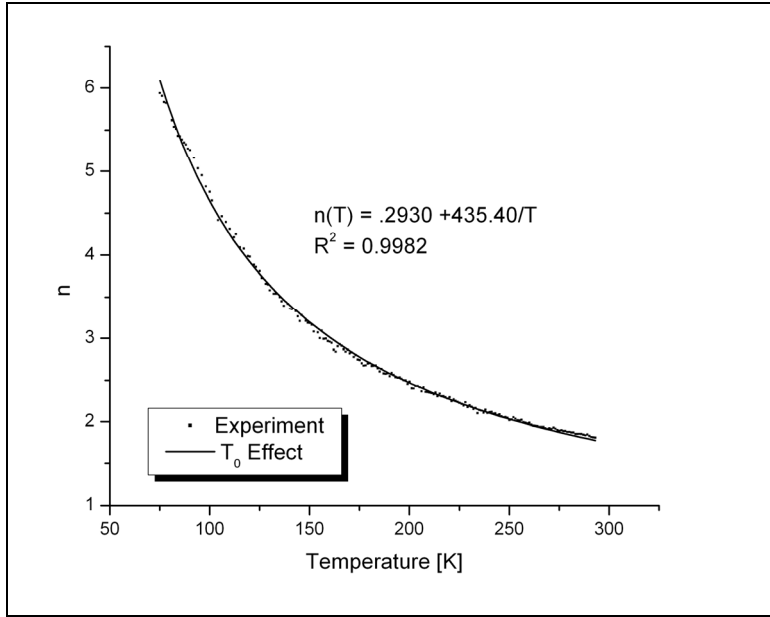


Figure 94. Temperature dependent ideality factor.

The high values of the ideality factor signify significant deviation from TE theory.

The increase in ideality factor with decreasing temperature is known as the “ T_0 effect”.

As shown in Figure 94, n varies inversely proportionally with temperature as:

$$n(T) = \left(n_0 + \frac{T_0}{T} \right) \quad (B4)$$

where n_0 is a constant and T_0 is known as the excess temperature [69]. Although various attempts have been made to explain the temperature dependence of n , perhaps the most relevant hypothesis was proposed by Crowell [70]. Crowell proposed that the T_0 anomaly could be obtained when surface states arise due to tunneling of electrons from the metal into the forbidden gap of the semiconductor. Although further investigation is beyond the scope of this research, it certainly reinforces the use of the proposed all-encompassing diode current model.

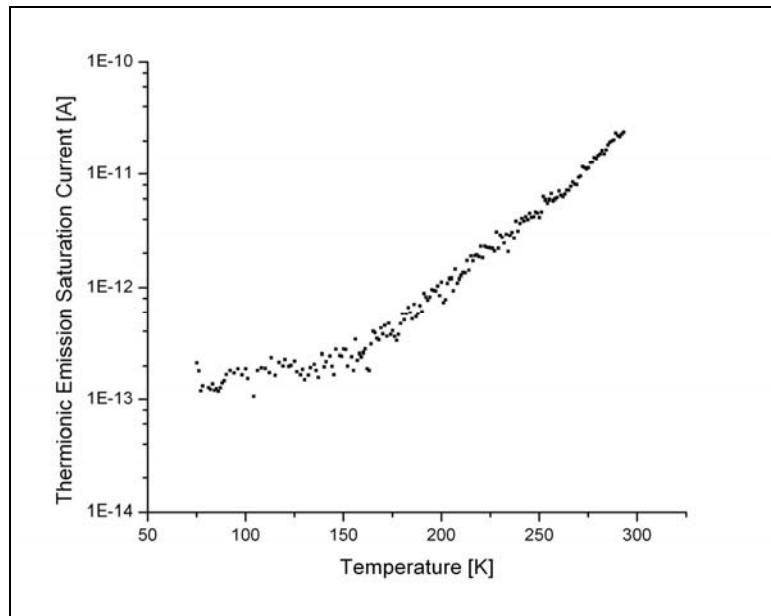


Figure 95. Temperature dependent TE saturation current.

The variation of n with temperature shown as Figure 96 demonstrates the plot of nkT/q vs. kT/q . Temperature independent ideality factors should result in a straight line with gradient n . However, three distinct linear regions conclusively confirm the temperature dependence of n assuming pure TE.

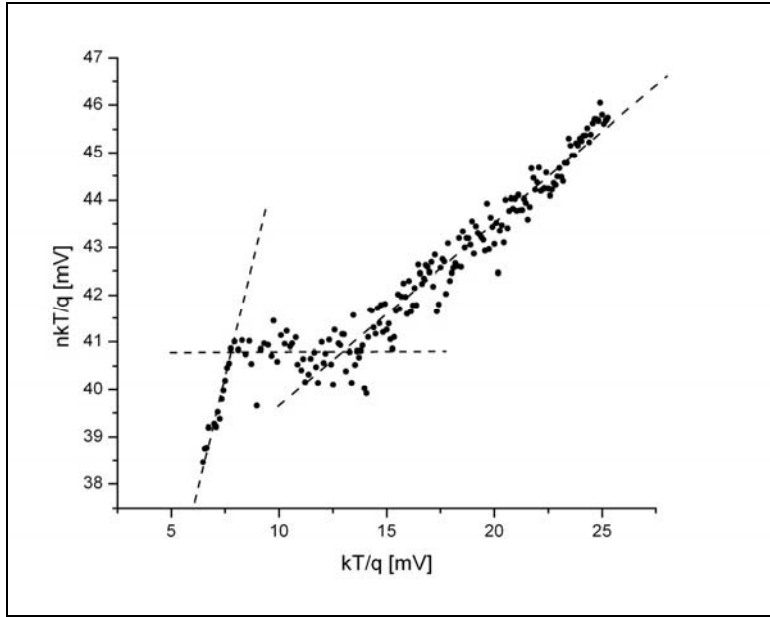


Figure 96. Temperature dependency of ideality factor.

The Richardson constant is typically determined from the y-intercept of $\ln(I_0 / T^2)$ verses $1000/T$ plot. The implicit assumption is that both the SBH and Richardson constant are temperature-independent. If either are temperature dependent, A^{**} can no long be determined. Non-linearities at low temperatures in Richardson plots render accurate parameter extraction impossible. This behavior is observed in Figure 97. Linearity can be restored if $\ln(I_0 / T^2)$ is plotted verses $1000/nT$ [69].

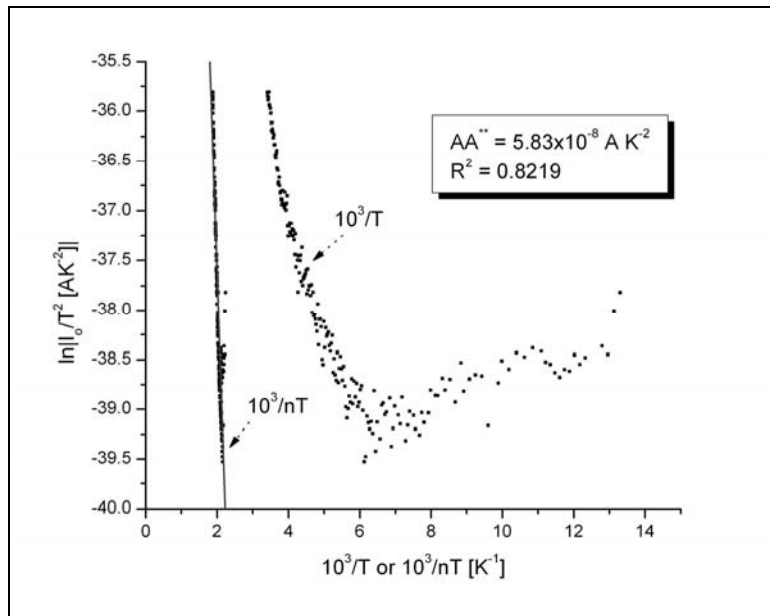


Figure 97. Richardson and modified Richardson Plot.

Current transport across an m-s interface is a thermally activated process. At low temperatures, electrons are able to overcome low barriers and current transport is dominated by current flow through patches of lower barrier heights and higher ideality factors. As the temperature increases, electrons gain sufficient energy to overcome the higher barriers. It has been proposed that the apparent increase in ideality factor and decrease in SBH at low temperatures is due to inhomogeneities of thickness and non-uniformity of the interface charges [71]. Figure 98 illustrates the low barrier height (perhaps dominated by patches) and the large ideality factor at low temperature. Extrapolation of the experimental barrier heights vs. the ideality factor to $n=1$ yields the homogeneous barrier height. Figure 99 shows the extrapolation technique that yields a homogeneous SBH of 0.6218 eV.

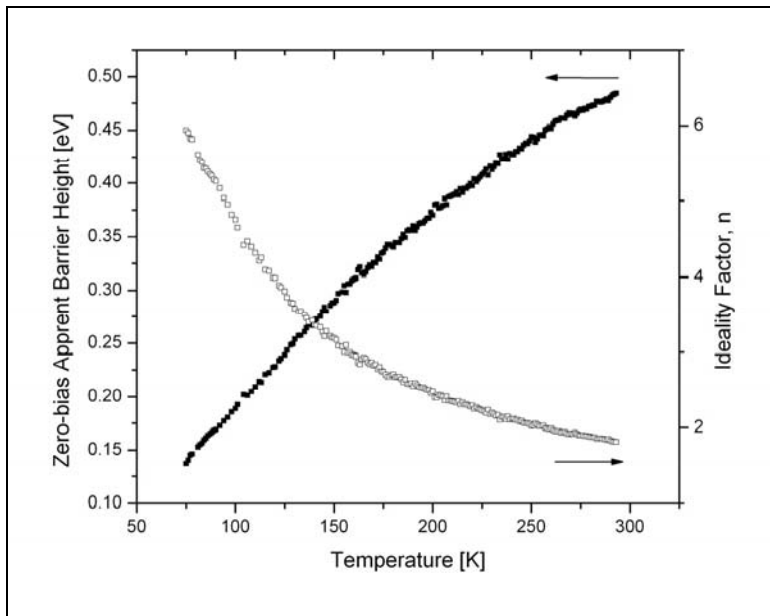


Figure 98. Temperature dependence of the ideality factor and SBH.

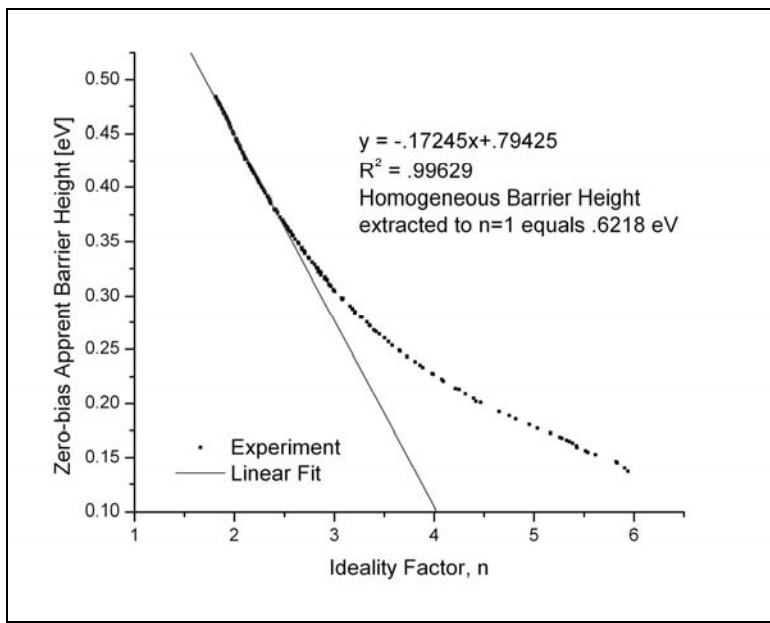


Figure 99. Zero-bias apparent SBH vs. ideality factor.

Application of a pure TE theory to the experimental data leads to several problems. Linearity of the Richardson plot is exceedingly poor at low temperatures, the ideality factor is high, and the Schottky barrier heights are low. These features suggest a

modified current generating mechanism, which in some cases can amount to greater than 90% of the total current [72]. A current-voltage relationship in which other current generating mechanisms dominate is appropriate.

Six-parameter Fitting Model

By measurement of the I-V characteristics of a Schottky diode, the six unknown variables in Equation 41 can be determined. The use of a weighted modified least squares method leads to suitable agreement between experimental data and the proposed model in a wide temperature range. Utilization of this model yields an accurate contribution of various current transport mechanisms and the parameters of the analyzed Schottky structure are evaluated with higher precision in a wide temperature range.

Figure 100 shows the well agreement of the model for a Schottky metal contact at 300 K. A comparison of the extracted parameters from the two methods is listed in Table 14.

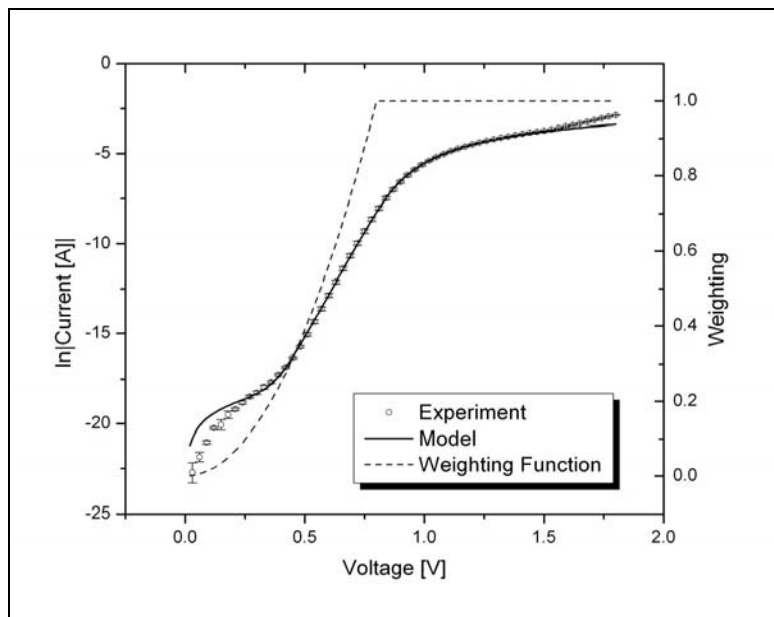


Figure 100. Six-parameter fitting model extracted via numerical fitting routine.

Table 14. TE vs six-parameter fitting model.

	I_{te} [A]	I_{gr} [A]	I_t [A]	E_0 [meV]	R_s [Ω]	R_l [$M\Omega$]
Pure TE Theory	1.37×10^{-12}	N/A	N/A	N/A	N/A	N/A
Proposed six-parameter fitting model	8.66×10^{-64}	3.38×10^{-37}	1.50×10^{-12}	41.8	25.6	32.7

The six-parameter fitting model yields a TE saturation current that is at maximum 52 OOM less than that assumed by pure TE aloneⁱ. Also shown is that G-R is essentially negligible and that the tunneling current is of the same OOM as the pure TE current. Therefore, at 80 K, tunneling and resistive leakage dominate. By repeating the extraction technique over a wide temperature range, the SBH and Richardson constant are determined with increased precision.

The TE saturation current (Figure 101) is highly temperature dependent and changes nearly 50 OOM in the temperature range of approximately 80 – 300 K. From Figure 101 the areal Richardson constant and SBH are determined. The areal Richardson constant is determined to be two OOM greater than that determined by TE theory alone and the temperature independent SBH is determined to be 1.0509 eV. Use of the six-parameter approach yields a SBH that is essentially temperature independent in a full range from 80-300 K (Figure 102). Figure 103 simply demonstrates that a straight line on a modified Arrhenius plot linearizes the temperature dependence of the TE

ⁱ When I_{te} and I_{gr} are increasingly small (limited to 10^{-100} [A]), the fitting routine attempts to increase both parameters to their maximum values without significantly increasing the fitting error. Without this function, the error is minimized with both values reaching their numerically limited minimum value. This behavior is a side effect of the minimizing function utilized within Mathematica.

saturation current. Similarly, the modified Arrhenius plot of I_{gr} can be used to determine the energy gap of the Schottky contact (Figure 104). The tunneling saturation current shown in Figure 105 is clearly the dominant transport mechanism at all temperatures. However, when plotted against $1000/T$, there are three distinct linear regions observable (Figure 106). Expected to dominate at low temperatures, tunneling saturation current is greatest at low temperatures.

The tunneling parameter E_{00} is determined from Equation 36 and Figure 107. The parameter was determined to be 49.801 ± 0.202 meV for this sample device. This is in general agreement to other tunneling parameters for Schottky contacts dominated by tunneling [52]. Other determined parameters include both series and parasitic resistance (Figure 108, Figure 109). Parasitic resistance is dominant at low applied biases and is subject to the largest uncertainties in the proposed fitting routine. Large uncertainty in R_1 arises due to both current detection limitations and large relative error in the data at low biases. The poor fit at low applied biases cannot be reconciled at this time and an appropriate weighting function is used to ensure a sufficiently suitable fit in the linear region.

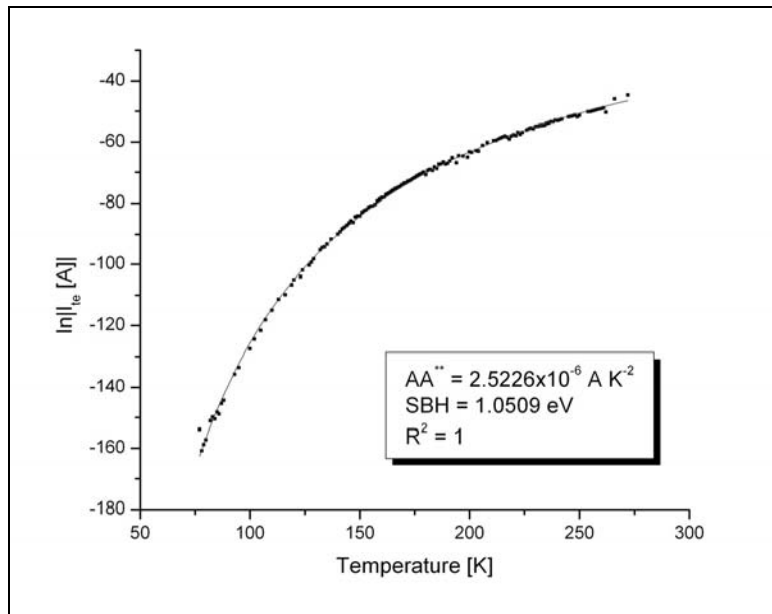


Figure 101. TE saturation current in a wide temperature range.

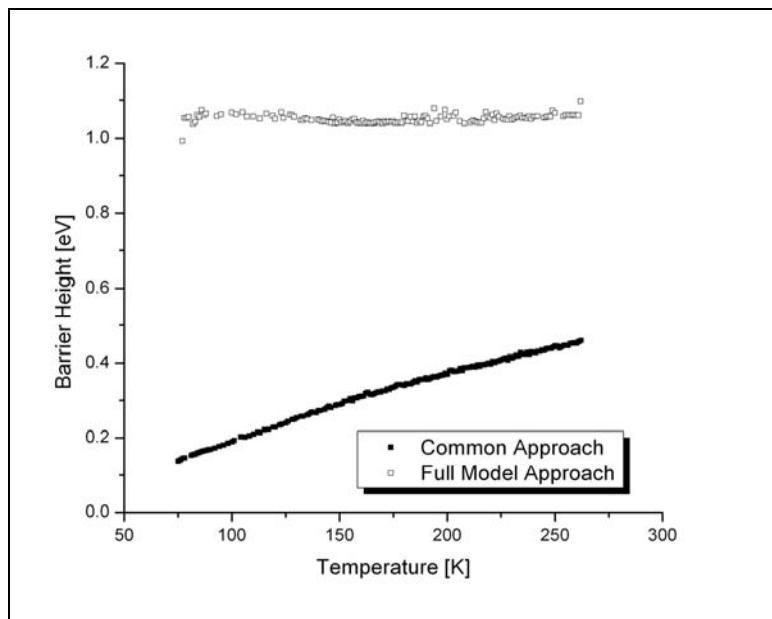


Figure 102. Temperature dependence of barrier height determined by the six-parameter method and TE only approach.

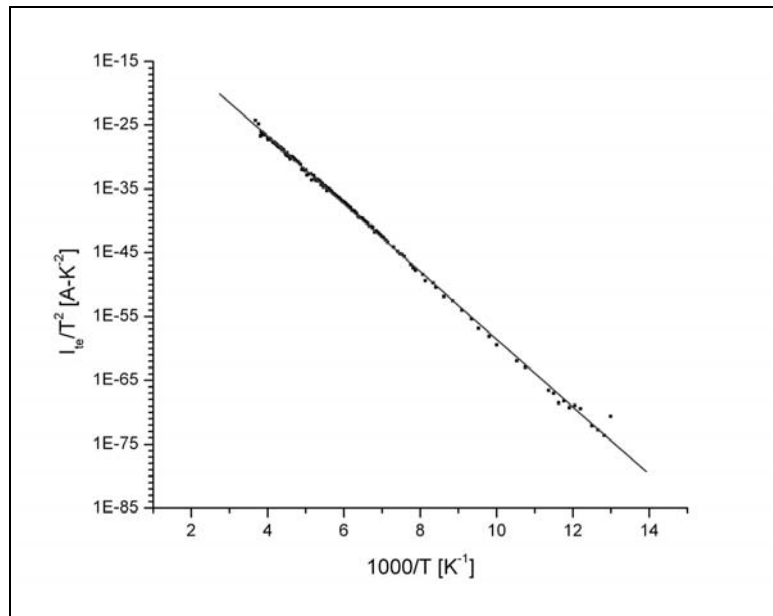


Figure 103. Arrhenius plot of TE saturation current.

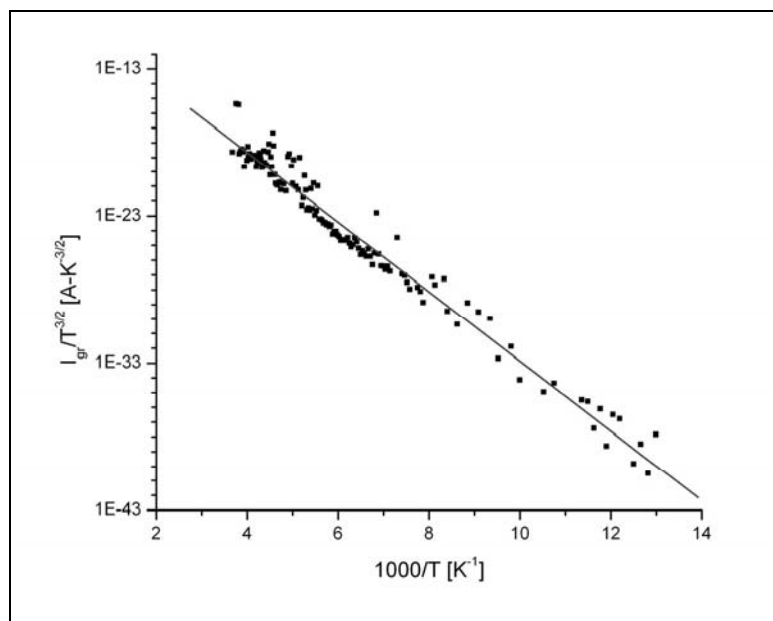


Figure 104. Arrhenius plot of GR saturation current.

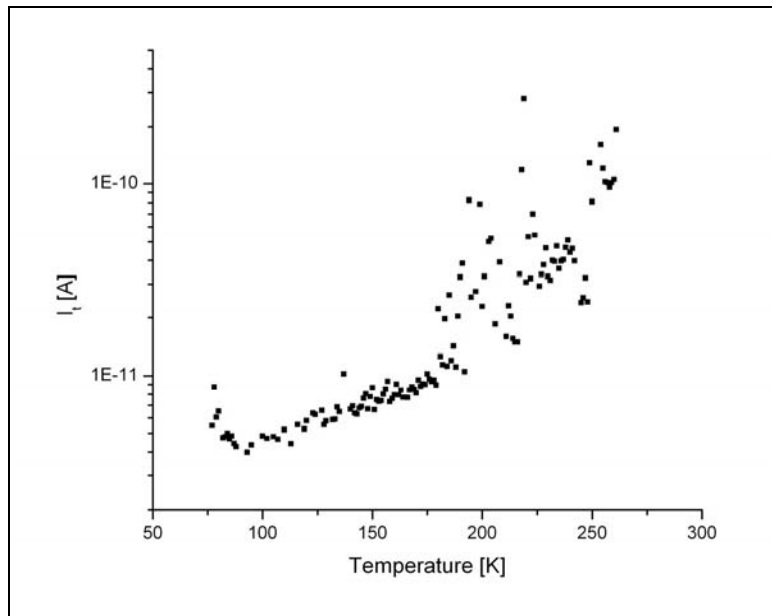


Figure 105. Temperature dependence of tunneling saturation current in a wide temperature range.

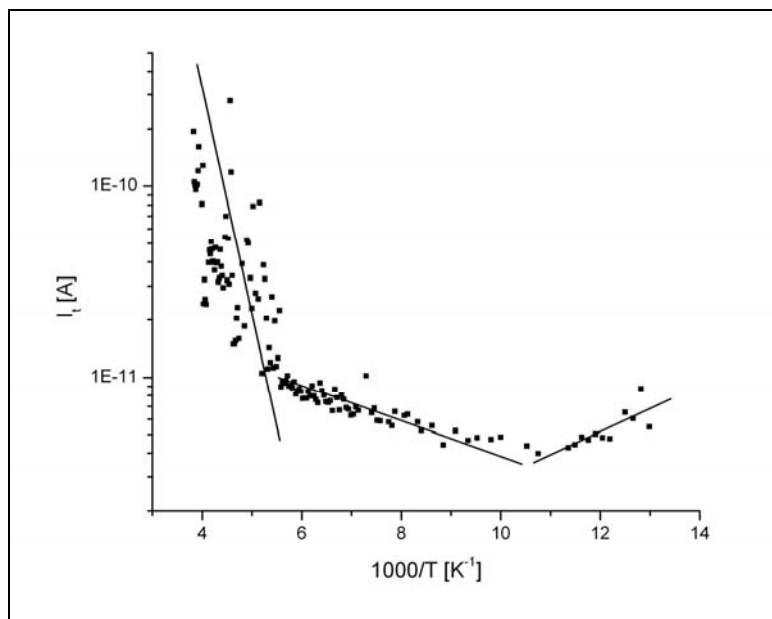


Figure 106. Arrhenius plot of tunneling saturation current with three distinct linear regions shown.

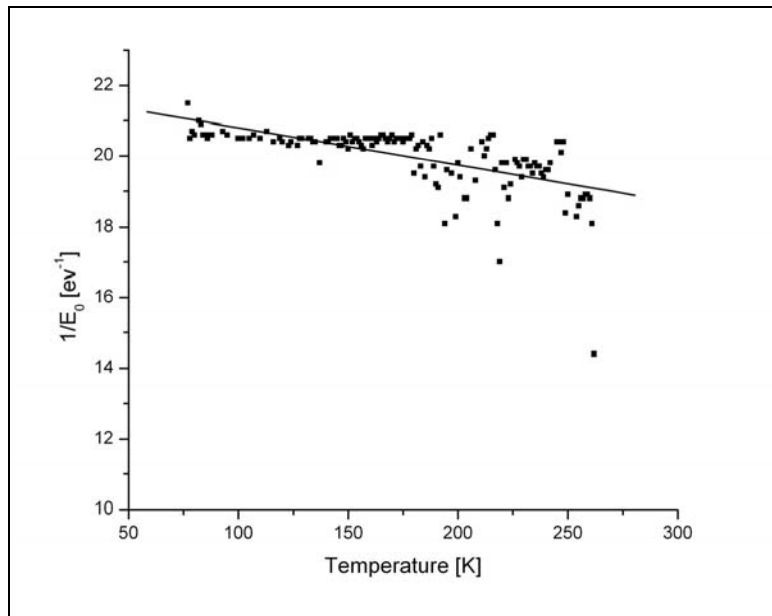


Figure 107. Reciprocal tunneling parameter, E_0 .

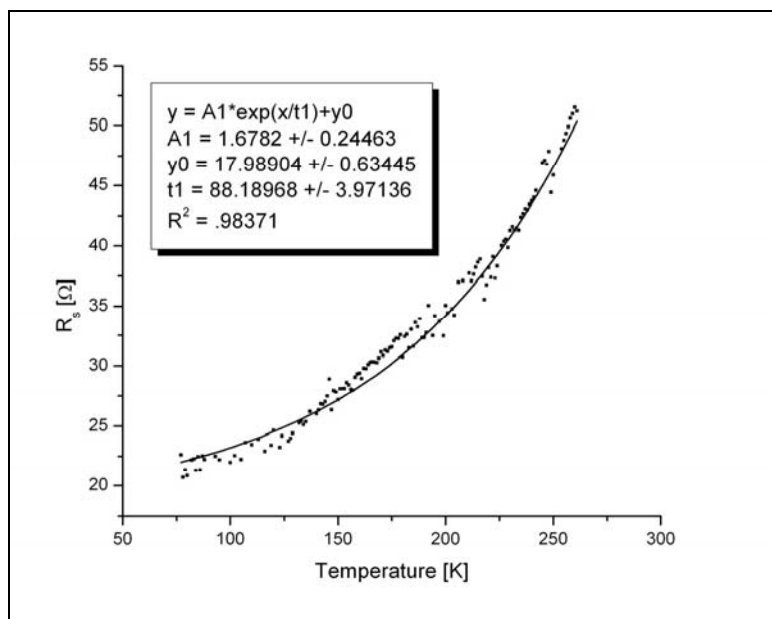


Figure 108. Temperature dependence of series resistance.

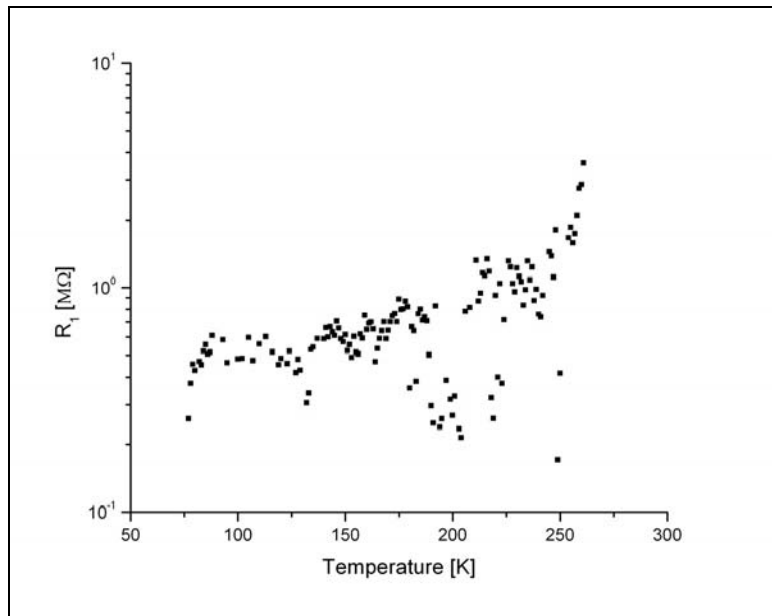


Figure 109. Temperature dependence of parasitic resistance, R_1 .

Table 15. Areal Richardson constant and Temperature-Independent SBH.

Device ID	AA^{**} [A-K ⁻²]	Temperature Independent SBH [eV]	E_{00} [meV]	R^2
A10	$2.5 \times 10^{-6} \pm 1.03 \times 10^{-20}$	$1.05 \pm 5.02 \times 10^{-17}$	49.8 ± 0.202	1
A12	$6.23 \times 10^{-11} \pm 1.7 \times 10^{-11}$	$0.95 \pm 3.86 \times 10^{-3}$	43.4 ± 0.987	0.997
A13	$1.05 \times 10^{-9} \pm 2.97 \times 10^{-10}$	$0.916 \pm 3.95 \times 10^{-3}$	41.6 ± 0.120	0.997
A24	$3.86 \times 10^{-8} \pm 1.03 \times 10^{-8}$	$0.96 \pm 3.78 \times 10^{-3}$	44.6 ± 0.136	0.997
A25 ^j	$1.02 \times 10^{-7} \pm 6.1 \times 10^{-8}$	$0.98 \pm 8.58 \times 10^{-3}$	50.9 ± 0.396	0.988
A30 Pre-irradiation	$2.8 \times 10^{-9} \pm 9.9 \times 10^{-10}$	$0.94 \pm 5.24 \times 10^{-3}$	42.1 ± 0.044	0.995
A30 Post-irradiation	$2.4 \times 10^{-7} \pm 1.1 \times 10^{-7}$	$1.09 \pm 7.15 \times 10^{-3}$	49.0 ± 0.309	0.993

^j Device irradiated at 80 K. Data taken during annealing process.

The experimentally determined values for AA^{**} fluctuate wildly when using the six-parameter fitting model. Since it is unlikely m^* is responsible for the wide-ranging value of A^{**} , the only remaining variable parameter is that of the effective diode area (A). The effective area can vary widely between devices and is particularly difficult to determine in multi-component semiconductor materials [52]. In the case of a very good Schottky contact with low leakage, the device area is so small that the detection limit is reached for low biases. Although the large structure of the FATFET should eliminate this problem, some devices exhibit the characteristic current limit at low bias. Figure 93 illustrates a device that is not particularly limited by current detection. Devices limited in this manner have somewhat disjointed and random current measurement readings at low biases and then seem to “turn on” at about 0.5 volts and immediately enter the linear region.

Appendix C – Nine Month Anneal Study

Devices A0408 and A0409 were irradiated by J.M. Sattler at 80 K under conditions listed as Table 16. At a total dose of $9 \times 10^{14} \text{ e}^- \cdot \text{cm}^{-2}$, device A0408 exhibited no transistor action and all measurements were at current compliance of the SMUs (100 mA). However, A0409 survived to a total dose of $3.67 \times 10^{15} \text{ e}^- \cdot \text{cm}^{-2}$. Following irradiation, the devices were placed in RT storage. No information on the light intensity is available.

Table 16. Second Irradiation Experiment Summary (28 January 2004) [29].

Sample	Energy [MeV]	Beam Current [μA]	Relative Dose [$\text{e}^- \cdot \text{cm}^{-2}$]	Relative Irradiation Time [min]	Total Dose [$\text{e}^- \cdot \text{cm}^{-2}$]	Total Irradiation Time [min]
A0408	0.45	0.13	10^{14}	7	1×10^{14}	7
A0408	0.45	0.13	2×10^{14}	13	3×10^{14}	20
A0408	0.45	0.13	6×10^{14}	39	9×10^{14}	59
A0409	0.45	0.3	3×10^{14}	8	3×10^{14}	8
A0409	0.45	0.3	6.7×10^{14}	13	9.7×10^{14}	21
A0409	0.45	0.3	9×10^{14}	18	1.87×10^{15}	39
A0409	0.45	0.3	1.8×10^{15}	50	3.67×10^{15}	89

Following a nine-month RT anneal, devices A0408 and A0409 were measured at RT and 80 K in darkness. To our amazement, A0408 again exhibited transistor action at both RT and 80K, apparently having annealed. All presented data measured at 80 K agrees well with RT measurements. Figure 110 illustrates the I-V characteristics of device A0408 at pre- and post-irradiation, and subsequent annealing at 9-mos. The figure shown is the GLADC. When the drain current is not adjusted for gate leakage, the 9-mos anneal drain current exhibits a similar pattern as the GLADC characteristics (Figure 111).

Table 17 summarizes the observed increase in drain current. Note, that the most off state, -3 V, exhibits the greatest percentage increase in drain current.

Table 17. Percent increase drain current from pre-irradiation baseline measurement following irradiation and annealing, A0408.

	$V_g = -1$ V	$V_g = -2$ V	$V_g = -3$ V
Pre-irradiation	-	-	-
$3 \times 10^{14} \text{ e}^- \cdot \text{cm}^{-2}$	14	45	117
$9 \times 10^{14} \text{ e}^- \cdot \text{cm}^{-2}$	Current Compliance	Current Compliance	Current Compliance
9-mos anneal	31	64.5	211

* Measured at +6 V drain voltage

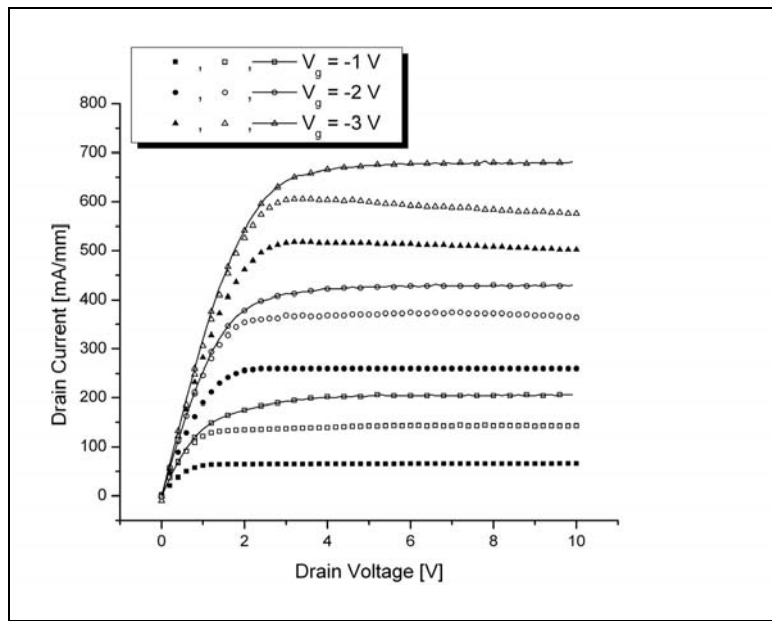


Figure 110. A0408: Solid symbols are pre-irradiation, open symbols are $3 \times 10^{14} \text{ e}^- \cdot \text{cm}^{-2}$, open-lined symbols are 9-mos measurements. Data is gate leakage adjusted drain current. The maximum RSD <1%.

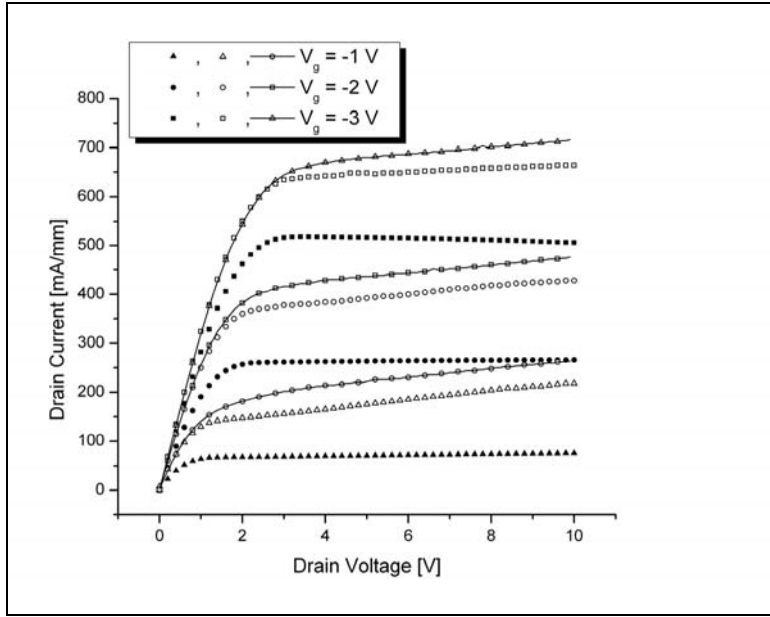


Figure 111. A0408: Non-Gate leakage adjusted drain current characteristics. The maximum RSD <1% and symbols have the same meaning as above.

The gate leakage of device A0408 also exhibited peculiar behavior. As the drain current annealed from current compliance, the final 9-mos value was greater than that measured post-irradiation at $3 \times 10^{14} \text{ e}^- \cdot \text{cm}^{-2}$. However, the gate leakage showed significantly more annealing. Figure 112, Figure 113, and Figure 114 illustrate the increase in gate leakage at the last post-irradiation measurement and subsequent annealing to a current less than post-irradiation. Device A0408 has gate leakage that is approximately two OOM greater than that of the specific devices used for this research. Hence, the GLADC is largely affected by changes in the gate current because they are of the same magnitude.

Table 18 lists the percentage increase from baseline measurements for the gate current. The observed gate leakage behavior is in opposition to the observed GLADC

differences. The largest deviation from baseline measurements for gate leakage occurred during the “most on” voltage of -1 V.

Table 18. Percent increase gate current from pre-irradiation baseline measurement following irradiation and annealing, A0408.

	$V_g = -1$ V	$V_g = -2$ V	$V_g = -3$ V
Pre-irradiation	-	-	-
3×10^{14} e ⁻ ·cm ⁻²	1300	1088	831
9×10^{14} e ⁻ ·cm ⁻²	Current Compliance	Current Compliance	Current Compliance
9-mos anneal	395	347	339

* Measured at +6 V drain voltage

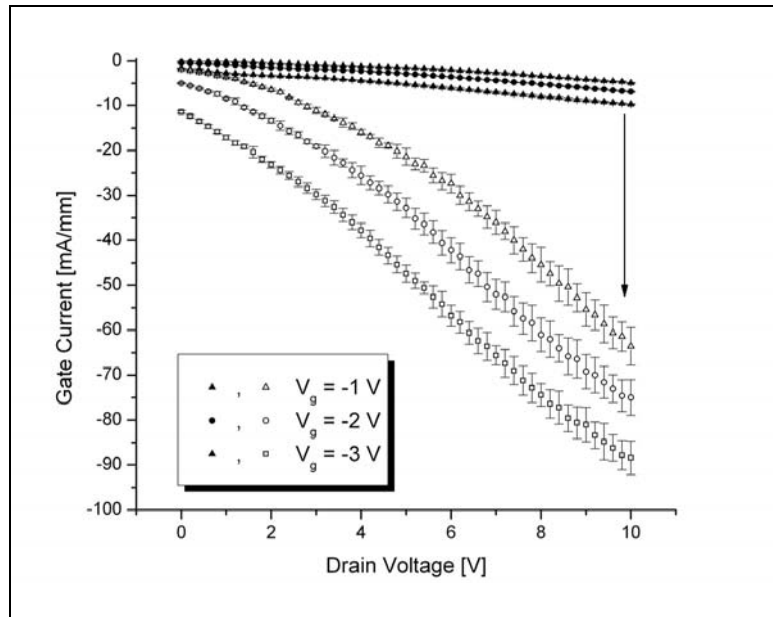


Figure 112. A0408: Pre- and post-irradiation gate leakage. Symbols have same meaning as above.

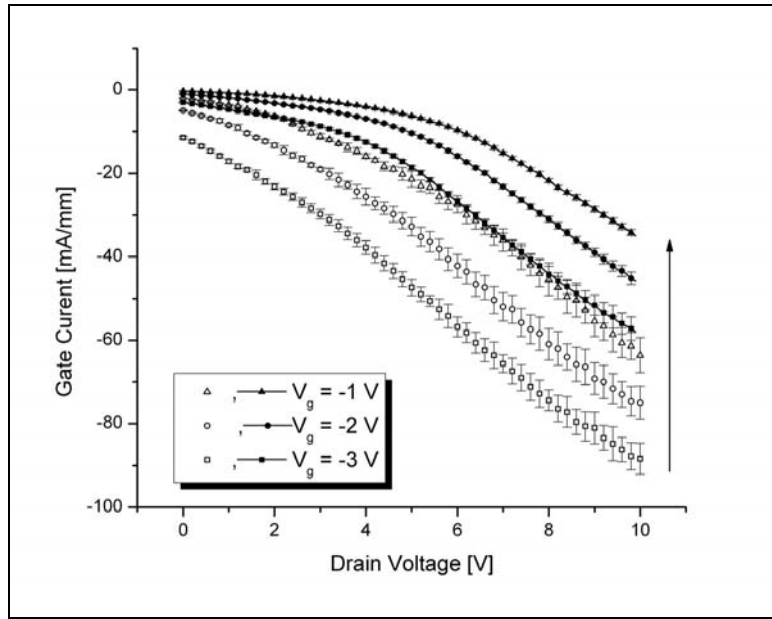


Figure 113. A0408: Gate leakage recovery after 9-mos anneal. Symbols have same meaning as in previous figures.

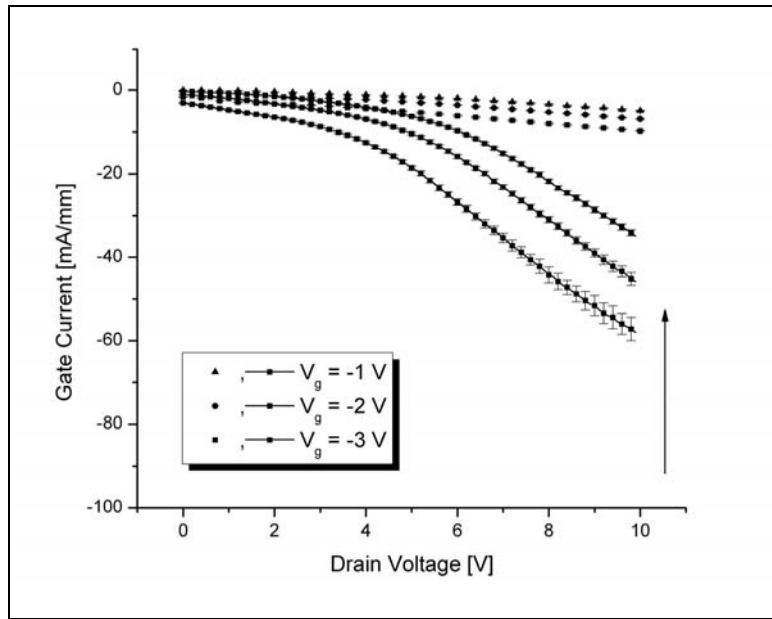


Figure 114. A0408: Recovery of gate leakage following a 9-mos RT anneal. Symbols have same meaning as in previous figures.

Of particular concern regarding the increased gate leakage is the tremendous jump at the initial irradiation and then relatively no additional radiation response. This behavior

is similar to the observed behavior when the device is damaged due to static discharge. Although discharges can greatly affect the Schottky contact, apparently little deviation from normal drain currents are observed. The conclusive evidence that the Schottky contact has been damaged comes from the Schottky contact data. A device that has been damaged due to static discharge exhibits Schottky diode characteristics with no linear region. Meaning, parasitic resistance and series resistance apparently dominate all other transport mechanisms. Although the devices are “useable” in the traditional sense, no long-term information is available. The mechanism of annealing static discharge damaged Schottky contacts is unknown.

Device A0409 also shows peculiar behavior that can be correlated to device A0408 but not confirmed. A particular difficulty in analyzing both devices is that their radiation hardness was quite different. Nonetheless, they provide interesting insight to the annealing phenomenon. Figure 115 shows the GLADC I-V characteristics for pre- and post-irradiation, and subsequent 9-mos RT anneal. Similar to that of A0408, the post-irradiation response is that of increasing drain current. However, the 9-mos anneal behavior for A0409 is unexpected. Figure 115 clearly shows that the drain current following annealing has increased when adjusted for gate leakage. This behavior is comparable to A0408 (Figure 110). However, in analyzing A0408, the assumption was made that the GLADC following annealing had increased from the post-irradiation values due to the device failure at $9 \times 10^{14} \text{ e}^- \cdot \text{cm}^{-2}$. Quantification of this increased is listed as Table 19.

Table 19. Percent increase drain current from pre-irradiation baseline measurement following irradiation and annealing, A0409 GLADC.

	$V_g = -1$ V	$V_g = -2$ V	$V_g = -3$ V
Pre-irradiation	-	-	-
$3.67 \times 10^{15} e^- \text{-cm}^{-2}$	16	43.6	136
9-mos anneal	26	63.6	209

* Measured at +6 V drain voltage

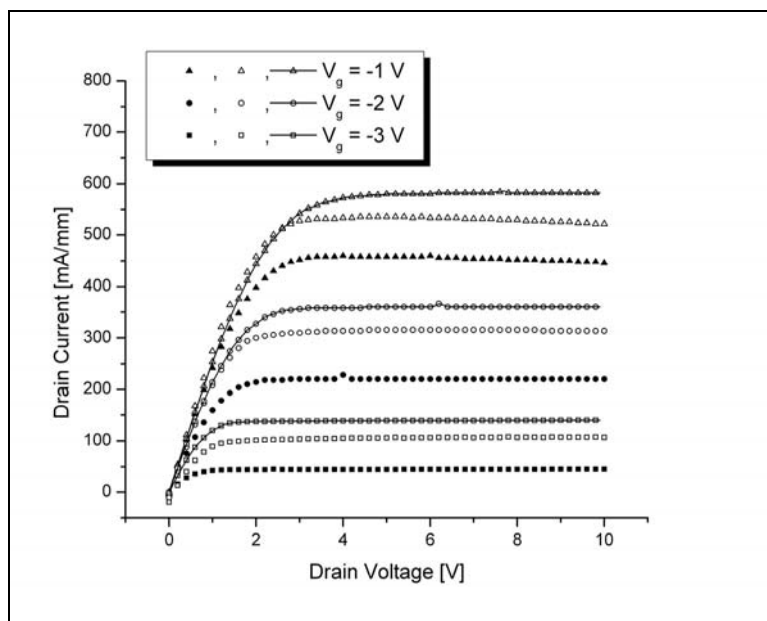


Figure 115. A0409: GLADC I-V characteristics. The maximum RSD <2.5%. Symbols have same meaning as above.

The non-GLADC I-V characteristics are shown as Figure 116 and demonstrate that there is annealing for low gate biases. From Figure 116 it appears that the nine month anneal value is below that of the final irradiation measurement. In fact, the data confirms a “recovery” of sorts (Table 20).

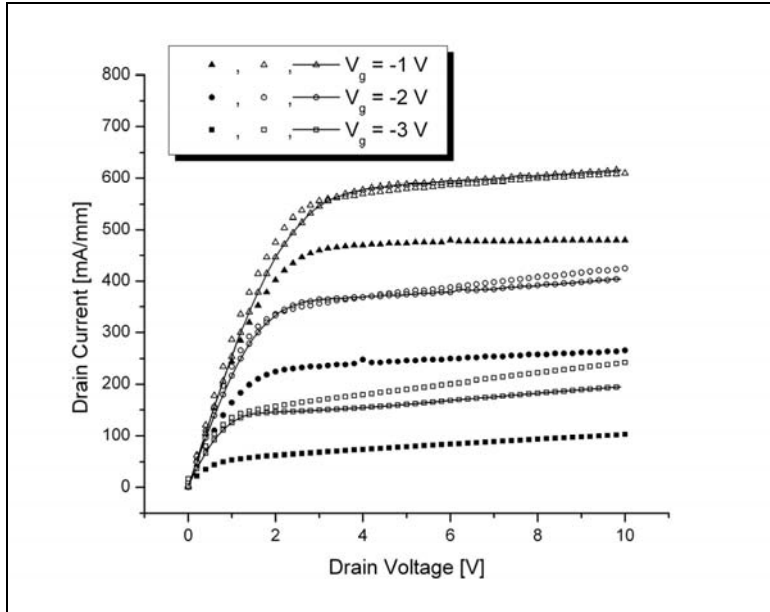


Figure 116. A0409: Non-GLADC I-V characteristics. Maximum RSD <2.5%. Symbols have same meaning as above.

Table 20. A0409: Percent increase drain current from pre-irradiation baseline measurement following irradiation and annealing, Non-GLADC.

	$V_g = -1$ V	$V_g = -2$ V	$V_g = -3$ V
Pre-irradiation	-	-	-
$3.67 \times 10^{15} e^- \text{cm}^{-2}$	23	56	139
9-mos anneal	23	51	100

* Measured at +6 V drain voltage

From the differences in the GLADA and non-GLADC plots, I contend that gate leakage anneals by a different process than that of the mechanism responsible for drain current. This is observed in device A0408 and the I-V characteristics of device A0409 seem comparable. Figure 117 and Figure 118 illustrate “super” recovery of the gate currents. At the maximum electron irradiation dose the gate leakage increased by greater than 100% for all gate voltages at +6 V Drain Voltage. This is an OOM less increase than

A0408. Table 21 lists the percentage increase from pre-irradiation baseline measurements.

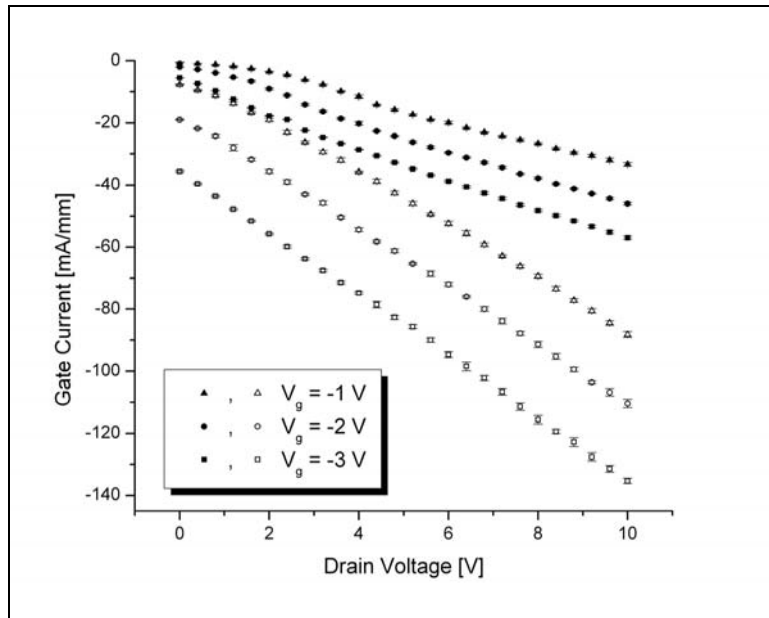


Figure 117. A0409: Increased gate leakage following a maximum dose of $3.67 \times 10^{15} e^- \text{cm}^{-2}$. Symbols have same meaning as above.

Table 21. A0409: Percent increase gate current from pre-irradiation baseline measurement following irradiation and annealing.

	$V_g = -1 \text{ V}$	$V_g = -2 \text{ V}$	$V_g = -3 \text{ V}$
Pre-irradiation	-	-	-
$3.67 \times 10^{15} e^- \text{cm}^{-2}$	163	143	144
9-mos anneal	-55	-55	-25

* Measured at +6 V drain voltage

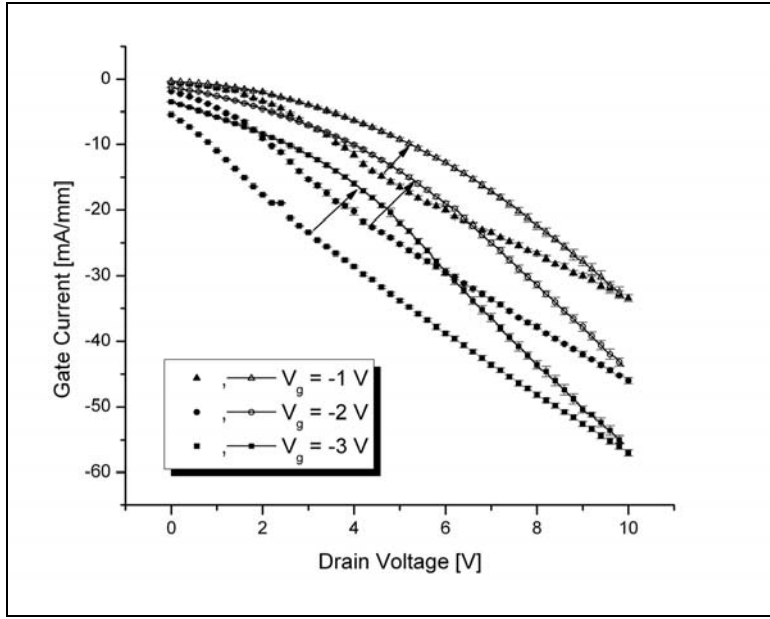


Figure 118. A0409: Annealing “super” recovery of gate leakage. Symbols have same meaning as above.

Although total I-V recovery was not achieved, gate leakage currents showed increased recovery effectiveness. When adjusted for gate leakage, it seems as if no annealing of the drain current occurred. However, due to gate leakage recovering, much more than the drain current and they are both of the same magnitude, the leakage dominates the adjusted curves. It appears that annealing is a balance of completing processes, namely, annealing of the bulk semiconductor material and properties responsible for 2DEG formation and processes pertaining to the Schottky contact. Previous work by Mishra *et al.* demonstrated that increased SBHs following gamma-irradiation were persistent at temperatures up 350 °C [22]. Although Schottky measurements are unavailable, I hypothesize the following: FATFATs have tunneling dominant charged carrier transport through the Schottky contact. An introduction of a large number of donor defects near the m-s interface increases defect-defect assisted

carrier transport. In addition, the introduction of donor defects act to “pump-up” the 2DEG. However, the increase in density of surface states is not persistent and the gate leakage recovers. At the same time, an unknown mechanism acts to recover the 2DEG at a slower rate.

While it is clear that gate leakage currents have significantly recovered, drain current recovery remains unclear. Although GaN may be rad-hard, the annealing rate is expected to be extremely slow due to energetically stable Ga and N bonds. From the standpoint of having to use a device in an integrated system, annealing is essentially nonexistent. That is to say, gate leakage is undesired and the device is drain current controlled.

Bibliography

- [1] Ma, T. P. and P. V. Dressendorfer (1989). Ionizing radiation effects in MOS devices and circuits. New York, Wiley.
- [2] Shur, M. S., R. Gaska, et al. (2002). Wide band gap electronic devices. Fourth IEEE International Caracas Conference on Devices, Circuits and Systems, Aruba.
- [3] Neuberger, R., G. Müller, et al. (2003). "Observation of ion-induced changes in the channel current of high electron mobility AlGaN/GaN transistors (HEMT)." Mater. Sci. Eng., B, **B93**: 143-146.
- [4] Morkoç, H. (1999). Nitride semiconductors and devices. Berlin ; New York, Springer.
- [5] McFall, Judy. "Optical Investigation of Molecular Beam Epitaxy $\text{Al}_x\text{Ga}_{1-x}\text{N}$ to determine material quality." Wright-Patterson AFB, OH: Air Force Institute of Technology (2000)
- [6] B. Luo *et al.* "High-energy proton irradiation effects on AlGaN/GaN high-electron mobility transistors," J. Electron. Mater. 31: 437-441 (2002).
- [7] Hu, X., A. P. Karmarkar, et al. (2003). "Proton-irradiation effects on AlGaN/AlN/GaN high electron mobility transistors." Nuclear Science, IEEE Transactions on **50**(6): 1791-1796.
- [8] Ionascut-Nedelcescu, A., C. Carbone, et al. (2002). "Radiation hardness of gallium nitride." Nuclear Science, IEEE Transactions on **49**(6): 2733-2738.
- [9] Kim, H., S.-J. Park, et al. (2001). "Effects of current spreading on the performance of GaN-based light-emitting diodes." IEEE Transactions on Electron Devices **48**(6): 1065-1069.
- [10] Zolper, J.C., "A Review of Junction Field Effect Transistors for High-Temperature and High-Power Electronics," Solid-State Electron. 42: 2153-2156 (1998).
- [11] Ionascut-Nedelcescu, A., C. Carbone, et al. (2002). "Radiation hardness of gallium nitride." Nuclear Science, IEEE Transactions on **49**(6): 2733-2738.

- [12] Morkoç, H., A. D. Carlo, et al. (2002). "GaN-based modulation doped FETs and UV detectors." *Solid-State Electron.* **46**: 157-202.
- [13] M. Stutzmann *et al.* "GaN-based heterostructures for sensor applications," *Diamond Relat. Mater.* 11: 886-891 (2002).
- [14] Henini, M. (1999). "III-V nitrides for electronic and UV applications." *III-V's Review* **12**(5): 28-32.
- [15] Morkoç, H., "Potential applications on III-V nitride semiconductors," *Mater. Sci. Eng., B*, B43: 137-146 (1997).
- [16] Gil, B. (2002). Low-dimensional nitride semiconductors. Oxford, Oxford University Press.
- [17] Umesh K. Mishra, *et. al.* "AlGaN/GaN HEMTs – An Overview of Device Operation and Applications," *Proceedings of the IEEE*, Vol. 90, No. 6: 1022-1031 (2002).
- [18] <http://nitronex.com/education/chartApplications.html>. Nitronex Corporation. Accessed: 19 February 2005.
- [19] Atkas, O., A. Kuliev, et al. (2004). "60Co gamma radiation effects on DC, RF, and pulsed I-V characteristics of AlGaN/GaN HEMTs." *Solid-State Electron.* **48**: 471-475.
- [20] Luo, B., J. W. Johnson, et al. (2002). "Influence of 60-Co Gamma Rays on dc performance of AlGaN/GaN high electron mobility transistors." *Appl. Phys. Lett.* **80**(4): 604-606.
- [21] Look, D. C., D. C. Reynolds, et al. (1997). "Defect Donor and Acceptor in GaN." *Phys Rev. Lett* **79**(12): 2273-2276.
- [22] Mishra, U.K., et al. (2004). "Effects of 60Co Gamma-Irradiation on Two-Dimensional Electron Gas Transport and Device Characteristics of AlGaN/GaN HEMTs. Air Force Office of Scientific Research: Multidisciplinary University Research Initiative, Nashville, Tennessee
- [23] Hu, X., B. K. Choi, et al. (2004). "The Energy Dependence of Proton-Induced Degradation in AlGaN/GaN High Electron Mobility Transistors." *Nuclear Science, IEEE Transactions on* **51**(2): 293-297.

[24] Umana-Membreno, G. A., J. M. Dell, et al. (2003). "⁶⁰Co gamma irradiation effects on n-GaN Schottky diodes." *Electron Devices, IEEE Transactions on* **50**(12): 2326-2334.

[25] Mishra, U.K., et al. (2004). " γ -irradiation induced defects in MOCVD n-GaN Schottky diodes." Air Force Office of Scientific Research: Multidisciplinary University Research Initiative, Nashville, Tennessee

[26] Fang, Z.-Q., L. Polenta, et al. (2000). Deep centers in as-grown and electron-irradiated n-GaN. Semiconducting and Insulating Materials Conference, 2000. SIMC-XI. International.

[27] D. C. Look, *et. al.* "On the Nitrogen Vacancy in GaN," *Appl. Phys. Lett.*, Vol. 83, No. 17: 3525-3527 (2003).

[28] Goodman, S. A., F. D. Auret, et al. (2000). Electron irradiation induced defects in n-GaN. Semiconducting and Insulating Materials Conference, 2000. SIMC-XI. International.

[29] Sattler, James M. *An Analysis of the Effects of Low Energy Electron Radiation on Al_xGa_{1-x}N/GaN Modulation-doped Field-effect Transistors*. Air Force Institute of Technology (AU), Wright-Patterson AFB OH, March 2004.

[30] Shreepad Karmalkar, *et. al.* "Mechanism of the reverse gate leakage in AlGaN/GaN high electron mobility transistors," *Appl. Phys. Lett.*, Vol. 82, No. 22: 3976-3978 (2003).

[31] D. Qiao, *et. al.* "Transport properties of the advancing interface ohmic contact to AlGaN/GaN heterostructures," *Appl. Phys. Lett.*, Vol. 80, No. 6: 992-994 (2002).

[32] M. Asif Khan, *et. al.* "AlGaN/GaN metal-oxide-semiconductor heterostructure field-effect transistors on SiC substrates," *Appl. Phys. Lett.*, Vol. 77, No. 9: 1339-1341 (2000).

[33] S. Nozaki, *et. al.* "Compression of the dc drain current by electron trapping in AlGaN/GaN modulation doped field-effect transistors," *Appl. Phys. Lett.*, Vol. 78, No. 19: 2896-2898 (2001).

[34] B. Luo *et. al.* "High-energy proton irradiation effects on AlGaN/GaN high-electron mobility transistors," *J. Electron. Mater.*, 31: 437-441 (2002).

[35] White B. D., *et al.* "Characterization of 1.8 MeV proton-irradiated AlGaN/GaN field-effect transistor structures by nanoscale depth-resolved luminescence spectroscopy," *IEEE Transactions on Nuclear Science* **49**: 2695-2701 (December 2002).

[36] White, B. D., M. Bataiev, *et al.* (2003). "Electrical, Spectral, and Chemical Properties of 1.8 MeV Proton Irradiated AlGaN/GaN HEMT Structures as a Function of Proton Fluence." *IEEE Transactions on Nuclear Science* **50**(6): 1934-1941.

[37] Gaudreau, F., P. Fournier, *et al.* (2002). "Transport properties of proton-irradiated gallium nitride-based two-dimensional electron-gas system." *Nuclear Science, IEEE Transactions on* **49**(6): 2702-2707.

[38] http://www.onr.navy.mil/sci_tech/information/312_electronics/ncsr/devices/hemt.asp. Office of Naval Research, National Compound Semiconductor Roadmap. Updated: 15 November 2004, Accessed: 19 February 2005.

[39] Ambacher, O., J. Smart, *et al.* (1999). "Two-dimensional electron gases induced by spontaneous and piezoelectric polarization charges in N- and Ga-face AlGaN/GaN heterostructures." *J. Appl. Phys.* **85**(6): 3222.

[40] Li, T., R. P. Joshi, *et al.* (2000). "Monte Carlo evaluations of degeneracy and interface roughness effects on electron transport in AlGaN–GaN heterostructures." *J. Appl. Phys.* **88**(2): 829-837.

[41] Rashmi, A. Agrawal, *et al.* (2000). "Analytical model for DC characteristics and small signal parameters of AlGaN/GaN modulation doped field effect transistors for microwave circuit applications." *Microwave and Optical Technology Letters* **27**: 413-418.

[42] Rashmi, S. Haldar, *et al.* (2001). "2-D analytical model for current voltage characteristics and output conductance of AlGaN/GaN MODFET." *Microwave and Optical Technology Letters* **29**: 117-123.

[43] Rashmi, A. Kranti, *et al.* (2003). "Comprehensive analysis of small signal parameters of fully strained and partially relaxed high Al-content lattice mismatched $\text{Al}_m\text{Ga}_{1-m}\text{N}/\text{GaN}$ HEMTs." *IEEE Trans. Microwave Theory and Techniques* **51**(2): 621-630.

[44] Rashmi, A. Kranti, et al. (2002). "An accurate charge control model for spontaneous and piezoelectric polarization dependent two-dimensional electron gas (2-DEG) sheet charge density of lattice mismatched AlGaN/GaN HEMTs." Solid-State Electronics **46**(5): 621-630.

[45] Rashmi, A. Kranti, et al. (2002). "Impact of strain relaxation of $\text{Al}_m\text{Ga}_{1-m}\text{N}$ layer on 2-DEG sheet charge density and current voltage characteristics of lattice mismatched $\text{Al}_m\text{Ga}_{1-m}\text{N}$ /GaN HEMTs." Microwave and Optical Technology Letters **33**(3): 205-212.

[46] Albrecht, J. D., P. P. Ruden, et al. (2000). "AlGaN/GaN Heterostructure Field-Effect Transistor Model Including Thermal Effects." IEEE Transactions on Electron Devices **47**(11): 2031-2036.

[47] Schroder, D. K. (1998). Semiconductor material and device characterization. New York, Wiley.

[48] Yu, L. S., Q. Z. Liu, et al. (1998). "The role of the tunneling component in the current-voltage characteristics of metal-GaN Schottky diodes." J. Appl. Phys. **84**(4): 2099-2104.

[49] Sze, S. M. (1981). Physics of semiconductor devices. New York, Wiley.

[50] Padovani, F. A. and R. Stratton (1966). "Field and Thermionic-Field Emission in Schottky Barriers." Solid-State Electron. **9**: 695-707.

[51] Abay, B., G. Çankaya, et al. (2003). "Barrier characteristics of Cd/p-GaTe Schottky diodes based on I-V-T measurements." Semicdon. Sc. Technol. **18**: 75-81.

[52] Donoval, D., M. Barus, et al. (1991). "Analysis of I-V measurements on PtSi-Si Schottky structures in a wide temperature range." Solid-State Electron. **34**(12): 1356-1373.

[53] Brad D. White. Department of Electrical and Computer Engineering, Ohio State University, Columbus, OH. Personal Correspondence 11 November 2004.

[54] Hasegawa, H. and S. Oyama (2002). "Mechanism of anomalous current transport in n-type GaN Schottky contacts." J. Vac. Sci. Technol. B **20**(4): 1647-1655.

[55] Hashizume, T., J. Kotani, et al. (2004). "Leakage mechanism in GaN and AlGaN Schottky interfaces." Appl. Phys. Lett. **84**(24): 4884-4886.

[56] Joseph Talnagi. Sr. Research Associate, Ohio State University Nuclear Reactor Laboratory, Columbus, OH. Personal Conversation 5 January 2005.

[57] Turner, J. E. (1992). Atoms, radiation, and radiation protection. New York, McGraw-Hill.

[58] MIL-STD-750D 1000 Series

[59] ASTM E772(1992), "Standard Practice for Characterizing Neutron Energy Fluence Spectra in Terms of an Equivalent Monoenergetic Fluence for Radiation-Hardness Testing of Electronics", Approved 15 SEP 1994

[60] David Christian. Quantifying Flux for (Bulk) Radiation Damage Studies. Fermi National Accelerator Laboratory. Document number: BTeV-doc-133-v1

[61] V. W. L. Chin, T. L. Tansley, and T. Osotchan, *J. Appl. Phys.* **75**, 7365 (1994).

[62] S. N. Mohammad and H. Morkoc, *Prog. Quant. Electron.* **20**, 361 (1996).

[63] A. S. Barker, Jr. and M. Ilegems, *Phys. Rev. B* **7**, 743 (1973).

[64] H. P. Maruska and J. J. Tietjen, *Appl. Phys. Lett.* **15**, 327 (1969).

[65] W. M. Yim, E. J. Stofko, P. J. Zanzucchi, J. I. Pankove, M. Ettenburg, and S. L. Gilbert, *J. Appl. Phys.* **44**, 292 (1973).

[66] Michael S. Shur and M. Asif Khan, *Mat. Res. Bull.* **22** (2), 44 (1997).

[67] U. V. Bhapkar and M. S. Shur, *J. Appl. Phys.*, **82** (4), 1649 (1997).

[68] S. K. O'Leary, B. E. Foutz, M. S. Shur, U.V. Bhapkar, and L. F. Eastman, *Solid State Comm.* **105**, 621 (1998).

[69] Sahin M., Safak H., et al. (2004). "Temperature dependence of current-voltage characteristics of Ag/p-SnS Schottky barrier diodes." *Appl. Surf. Sci.* In Press, Corrected Proof.

[70] Crowell, C. R. (1977). "The physical significance of the T0 anomalies and interface states." *Solid-State Electron.* **20**: 171-175.

- [71] Chand, S. and J. Kuma (1995). "Current-voltage characteristics and barrier parameters of Pd₂Si/p-Si(111) Schottky diodes in a wide temperature range." Semicond. Sci. Technol. **10**: 1680-1688.
- [72] Sellai, A., M. S. Raven, et al. (2000). "I-V-T measurements on GaAs/AlGaAs heterojunctions interpreted on the basis of thermally assisted tunneling." Eur. Phys. J. AP **9**: 131-136.

REPORT DOCUMENTATION PAGE
*Form Approved
OMB No. 0704-0188*

The public reporting burden for this collection of information is estimated to average 1 hour per response, including the time for reviewing instructions, searching existing data sources, gathering and maintaining the data needed, and completing and reviewing the collection of information. Send comments regarding this burden estimate or any other aspect of this collection of information, including suggestions for reducing the burden, to the Department of Defense, Executive Services and Communications Directorate (0704-0188). Respondents should be aware that notwithstanding any other provision of law, no person shall be subject to any penalty for failing to comply with a collection of information if it does not display a currently valid OMB control number.

PLEASE DO NOT RETURN YOUR FORM TO THE ABOVE ORGANIZATION.

1. REPORT DATE (DD-MM-YYYY)	2. REPORT TYPE	3. DATES COVERED (From - To)		
4. TITLE AND SUBTITLE		5a. CONTRACT NUMBER		
		5b. GRANT NUMBER		
		5c. PROGRAM ELEMENT NUMBER		
6. AUTHOR(S)		5d. PROJECT NUMBER		
		5e. TASK NUMBER		
		5f. WORK UNIT NUMBER		
7. PERFORMING ORGANIZATION NAME(S) AND ADDRESS(ES)			8. PERFORMING ORGANIZATION REPORT NUMBER	
9. SPONSORING/MONITORING AGENCY NAME(S) AND ADDRESS(ES)			10. SPONSOR/MONITOR'S ACRONYM(S)	
			11. SPONSOR/MONITOR'S REPORT NUMBER(S)	
12. DISTRIBUTION/AVAILABILITY STATEMENT				
13. SUPPLEMENTARY NOTES				
14. ABSTRACT				
15. SUBJECT TERMS				
16. SECURITY CLASSIFICATION OF:		17. LIMITATION OF ABSTRACT	18. NUMBER OF PAGES	19a. NAME OF RESPONSIBLE PERSON
a. REPORT	b. ABSTRACT	c. THIS PAGE		19b. TELEPHONE NUMBER (Include area code)